Warsaw University of Technology

Faculty of Physics

Ph.D. Thesis

Marcin Zawisza M.Sc.

Study of meson-baryon correlations in relativistic nuclear collisions registered by the STAR detector

Supervisor

Professor Jan Pluta Ph.D. D.Sc.

Warsaw 2010

Contents

List of Tables

List of Figures

Streszczenie

Korelacje cząstek nieidentycznych przy niskich prędkościach względnych mierzą asymetrie czasowo-przestrzenne pomiędzy punktami emisji cząstek w czasie wymrożenia. Źródłem obserwowanych asymetrii czasowo-przestrzennych mogą być rezonanse, kolektywne zachowanie się wytworzonej materii czy różnice w procesie wymrażania różnych rodzajów cząstek.

Przedstawiona praca zawiera analizę korelacji mezon-barion (pion-proton) w zderzeniach jąder złota przy energii w układzie środka masy równej 200GeV/nukleon. Dane doświadczalne pochodzą z eksperymentu STAR, znajdującego się w Brookhaven National Laboratory w USA. Program naukowy eksperymentu STAR jest dedykowany do badania właściwości plazmy kwarkowo-gluonowej, a analiza zawarta w tej pracy jest elementem tego przedsięwzięcia.

W rozdziale pierwszym zawarto wprowadzenie do fizyki ciężkich jonów oraz podstawowe sygnatury plazmy kwarkowo-gluonowej. Formalizm matematyczny funkcji korelacyjnych oraz oddziaływań w stanie końcowym wprowadzony został w rozdziale drugim. Rozdział trzeci został poświęcony dotychczasowym analizom korelacyjnym wykonanym głównie w eksperymencie STAR oraz nielicznym wcześniejszym próbom wyznaczenia asymetrii czasowo-przestrzennej układu pion-proton. Kompleks eksperymentalny zderzacza ciężkich jonów RHIC oraz eksperyment STAR zostały opisane w rozdziale czwartym. Technika analizy eksperymentalnej, zastosowane metody analizy i uzyskane wyniki przeprowadzonych badań zawarte są w rozdziale piątym. Rozdział szósty poświęcony został symulacjom, których wyniki odniesione do danych eksperymentalnych ułatwiły interpretację zaobserwowanych efektów i wyciągnięcie wniosków. Rozprawę kończy rozdział siódmy, w którym przedstawione zostały najistotniejsze wnioski z przeprowadzonych badań.

Analiza korelacji pion-proton wymagała zbadania wpływu produktów rozpadów rezonansów delta oraz słabo rozpadającego się barionu lambda na obserwowane funkcje korelacyjne oraz czasowo-przestrzenne rozkłady źródła. W tym celu wykonane zostały stosowne obliczenia z użyciem modeli.

Analiza eksperymentalna wymagała przezwyciężenia trudności związanych z ograniczoną akceptancją detektora. Duża różnica mas między pionem a protonem sprawia, że wybór pionu i protonu o bliskich prędkościach wymaga wyboru cząstek o dużej różnicy pędów. W rezultacie piony użyte w analizie wybrane zostały z dolnej granicy akceptancji pędowej komory projekcji czasowej, protony natomiast wybrane zostały z obszaru górnej granicy akceptancji pędowej detektora (a nawet nieznacznie ją przekraczając). Dodatkowym czynnikiem utrudniającym analizę jest fakt, że krzywa dE/dx pionów w wybranym do analizy zakresie pędu przecina się z krzywą dE/dx elektronów. Również krzywa dE/dx protonów w wybranym do analizy zakresie pędu przecina się z krzywą elektronów. Powoduje to iż skorelowane pary elektron-pozyton pochodzące z konwersji w materiale detektora kwantów gamma mogą zostać błędnie zidentyfikowane jako pary pion-proton. W celu eliminacji takich par zastosowano dodatkowe topologiczne kryteria selekcji cząstek.

Kryteria selekcji pionów i protonów wymuszone znaczną różnicą mas powodują, że pewne orientacje z przestrzeni wektora k^* (pęd pierwszej cząstki w układzie spoczynkowym pary) nie są rejestrowane. Dotychczas stosowane metody obliczania funkcji korelacyjnych, ze względu na wysoką czułość na ten brak akceptancji nie pozwalały na określenie parametrów badanego źródła. Problemy te przezwyciężono po zastosowaniu nowatorskiej metody, opracowanej w 2008 roku, wyznaczania funkcji korelacyjnych bezpośrednio rozłożonych na sferyczne funkcje harmoniczne.

Na podstawie otrzymanych funkcji korelacyjnych wyznaczono parametry gaussowskiego źródła. Wyniki wskazują, że średnie punkty emisji pionów i protonów są różne. Asymetria pomiędzy punktami emisji dwóch rodzajów cząstek jest skorelowana z rozmiarem źródła i zależy od centralności zderzenia.

Badania z użyciem modeli potwierdzają obserwacje dokonane w danych eksperymentalnych. Obserwowana asymetria ma charakter czasowo-przestrzenny. Piony emitowane są później niż protony, a średni punkt emisji protonów jest przesunięty na zewnątrz źródła względem średniego punktu emisji pionów. Asymetria czasowa i przestrzenna są ze sobą skorelowane - większe przesunięcie przestrzenne pociąga za sobą większą różnicę w czasach emisji. Obszar źródła, z którego emitowane są protony jest mniejszy niż obszar źródła, z którego emitowane są piony.

Obserwowane właściwości źródła utworzonego w zderzeniach jąder złota przy energii 200GeV na nukleon w układzie środka masy wskazują na kolektywne właściwości wytworzonej materii.

Abstract

Correlations between non-identical particles at small relative velocity probe asymmetries in the average space-time emission points at freeze-out. The origin of such asymmetries may arise from long-lived resonances, bulk collective effects, or differences in the freeze-out scenario for the different particle species.

This thesis presents study of meson-baryon (pion-proton) femtoscopy in Au+Au collisions at $\sqrt{s_{NN}} = 200$GeV. Data used in this work was registered by the STAR (Solenoidal Tracker at RHIC) experiment in Brookhaven National Laboratory in 2004. Scientific program of the STAR experiment was dedicated to search for Quark Gluon Plasma and investigation of its properties. Analysis presented here is an element of this exciting and pioneering scientific adventure.

This work was done at the most advanced experimental facility, dedicated to heavy ion collisions, in the World . Obtained experimental results proved that average emission points of pions and protons are not the same. Source of protons is smaller than the source of pions and is shifted to the edge of the system created in heavy ion collision.

This dissertation is organized as follows. Short introduction to the heavy ion physics, basic concepts of the signatures of the quark gluon plasma can be found in the chapter 1. Formalism related to the correlation functions or final state interactions FSI is presented in the chapter 2. Chapter 3 shows overview of the HBT analyzes done by the STAR collaboration for the Au+Au collisions. It contains also overview of the attempts to the pion-proton femtoscopy made so far by a few other collaborations. Description of the experimental setup RHIC complex and STAR experiment can be found in the chapter 4. Experimental analysis, technique and obtained results step by step are described in the chapter 5. Discussion and interpretation of the results is done via comparison to the similar studies performed with `Therminator` and `UrQMD` models and is presented in chapter 6. At the end the whole work is summarized in the chapter 7.

Chapter 1

Introduction

1.1 Relativistic Heavy-Ion Collisions

Heavy-Ion collisions at relativistic energies gives possibility to study properties of nuclear matter at extreme conditions of temperature and density. Nuclei under such conditions passes to a new state of matter called Quark Gluon Plasma (QGP). According to the Big-Bang theory this state of matter existed in the first microseconds after the Big-Bang. In QGP quarks and gluons are not bounded into hadrons. They can freely move over the whole volume of the plasma.

Process of a space-time evolution of the system created in two relativistic nuclei collision is presented on figure 1.1. Just after the collision (center of the $z-t$ coordinate system) during the pre-equilibrium phase, partons bounded into nucleons interact with each other. Fragments of the nuclei which did not interact move away along the light cone. According to the current state of research, energy cumulated in the mid-rapidity region is sufficient to create a quark gluon plasma QGP which achieves a local equilibrium at the proper time τ_0=1fm/c. QGP phase evolves according laws of hydrodynamics. During this phase system expands what results in drop of its temperature. Plasma begins to hadronize what is depicted as a mixed phase. After crossing chemical freeze-out line all quarks and gluons are bounded into hadrons which finally streams out of the collision region after thermalization (temperature of the system drops below the thermal freeze-out temperature).

Properties of matter created in heavy ion collisions are extensively investigated in experiments performed in two World's leading laboratories, Brookhaven National Laboratory in USA at Relativistic Heavy Ion Collider (RHIC) and CERN in Europe at Super Proton Synchrotron (SPS) as well as recently started Large Hadron Collider (LHC).

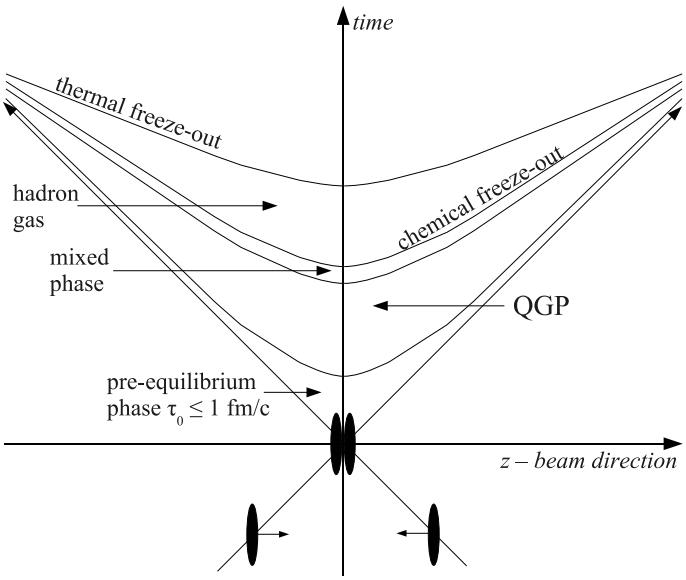

Figure 1.1: Schematic light-cone diagram of a heavy ion collision.

1.2 QCD calculations - energy density and phase diagram

Due to characteristics of the strong force quarks and gluons can exist only in states bounded into hadrons. However under condition of high temperature or baryon density it is possible to achieve an asymptotic freedom in which partons do not interact with each other and can freely move over the created system. Figure 1.2 represents lattice QCD (quantum chromodynamics) calculations [2] of a phase diagram of a nuclear matter, T versus μ_B, the baryonic chemical potential. At $\mu_B = 0$ the transition from hadron resonance gas to quark gluon plasma takes place at the critical temperature $T_c = 164 \pm 2MeV$. Curvature of the crosover transition is given by

$$\frac{T}{T_c} = 1 - \frac{C\mu_B^2}{T_c^2}, C = 0.0032 \tag{1.1}$$

The solid line which starts from the endpoint at $T_E = 162 \pm 2MeV$, $\mu_B = 360 \pm 40MeV$ is a first order phase transition.

The only one experimental way to create quark gluon plasma is through increasing temperature of the system in ultra-relativistic ion collisions. Limits of existence of hadronic phase is not only reached by exceeding critical temperature T_c but also by increasing density of matter, the so called "cold compression". Deconfined quarks and gluon at low temperature and high baryonic density create state called Color Superconductor which possibly exists in the interior of the neutron stars. Mechanism of deconfinement at low temperature and high baryon density

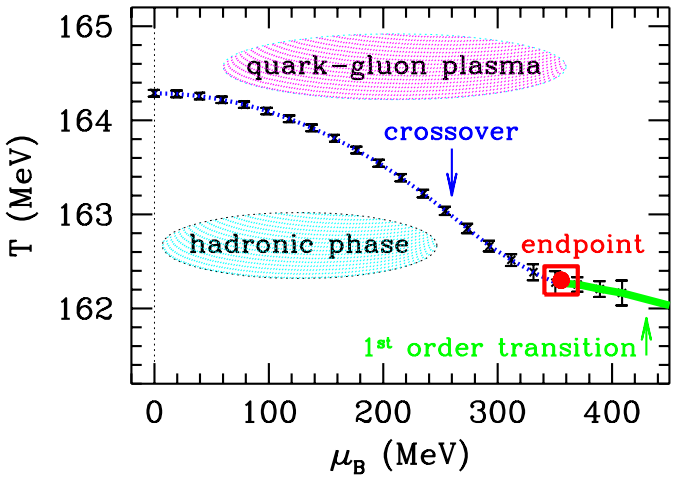

Figure 1.2: Phase diagram of a nuclear matter (lattice QCD calculations) [2].

is called Debye screening. Due to compression of matter quarks and gluons cannot be localized in nucleons. This phenomena is achieved when long range interactions are screened, Debye screening radius r_D is shorter than the nucleon radius.

Figure 1.3 shows QCD calculations by Frithjof Karsch [1] for 2-flavour (u,d) and 3-flavor (u,d,s) quarks as well as two light (u,d) and one heavier (s) quark mass of energy density ε/T^4 as a function of temperature normalized to the critical temperature T/T_c. Transition to quark gluon plasma is seen as a sudden increase of energy density at T/T_c about 1. All three calculations gives consistent results of estimated energy density at T_c, $\varepsilon_c = (6 \pm 2)T_c^4$.
For high temperature regime $T \gtrsim 1.5T_c$ the equation of state, the temperature dependence on energy density ε/T^4 and pressure p/T^4, asymptotically approach the free gas limit for gas of gluons and n_f quark flavors.

$$\frac{\varepsilon_{SB}}{T^4} = \frac{p_{SB}}{T^4} = \left(16 + \frac{21}{2} n_f\right) \frac{\pi^2}{30} \tag{1.2}$$

Equation 1.2 can be used for descriptions of systems with low net baryon density (close numbers of quarks and anti-quarks) and non interacting quarks and gluons.

Figure 1.4 presents recent calculations of energy density and three times pressure as a function of temperature calculated by A. Bazavov et. al in [3]. Although sudden increase of energy density is observed, it is not the first order phase transition but a smooth cross over. The band of the transition region is for temperatures from 185MeV to 195MeV.

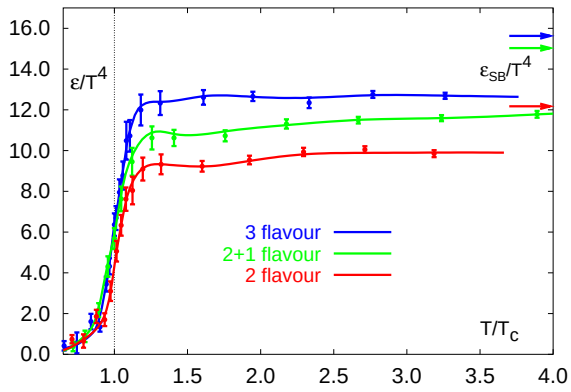

Figure 1.3: Energy density as a function of temperature in QCD calculations for 2- and 3-flavor quarks [1].

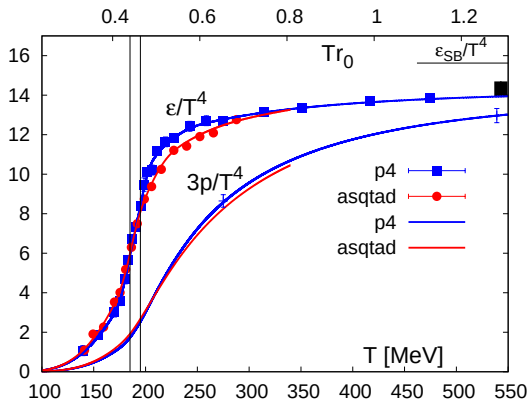

Figure 1.4: Energy density and three times the pressure calculated on lattices. The band indicates the transition region 185 MeV < T < 195 MeV. [3].

1.3 Signatures of Quark Qluon Plasma

1.3.1 Elliptic flow and scaling with the number of constituent quarks

In non-central collisions anisotropy of particle distribution in transverse plain occurs. This phenomena is called anisotropic flow. The transverse single particle distribution in the azimuthal angle ϕ is often expressed in Fourier expansion:

$$E\frac{d^3N}{d^3p} = \frac{1}{2\pi}\frac{d^2N}{p_T dp_T dy}\left(1+2\sum_{n=1}^{\infty} v_n \cos\left[n(\phi-\Phi_{RP})\right]\right) \tag{1.3}$$

where Φ_{RP} is the angle of the reaction plane defined by impact parameter and longitudinal direction. The most exciting observations are for the second order harmonic coefficient v_2 which characterizes the ellipticity of the azimuthal distribution of the produced particles thus it is called "elliptic flow".

Figure 1.5 depicts how spacial anisotropy and different gradients of pressure for different orientations of azimuth of the particle with respect to the reaction plane results in momentum-space anisotropy of produced particles.

Figure 1.6 shows v_2 measurements done at RHIC by Phenix and STAR experiments [4]. Left group of panels shows v_2 as a function of transverse momentum case (a) and v_2 as a function of KE_T - transverse kinetic energy. $v_2(p_T)$ shows mass ordering for $p_T < 2GeV/c$, for higher values of transverse momentum mass ordering is broken and quark composition of the particles dominates over their masses. Plot (b) on the left panel of figure 1.6 shows v_2 as a function of

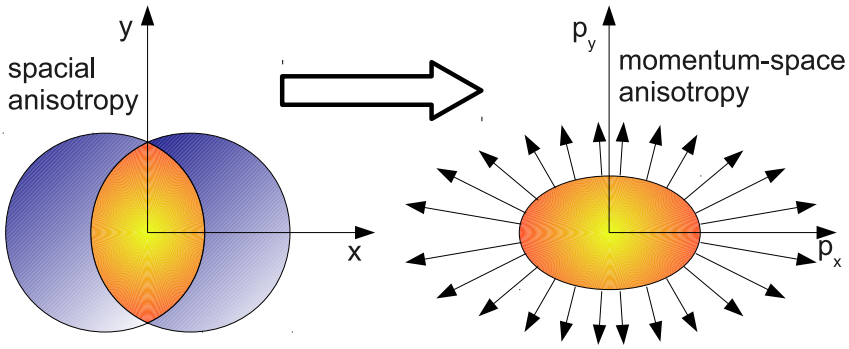

Figure 1.5: Elliptic flow phenomena. Pressure gradients in spacial anisotropy in non-central collision results in momentum-space anisotropy.

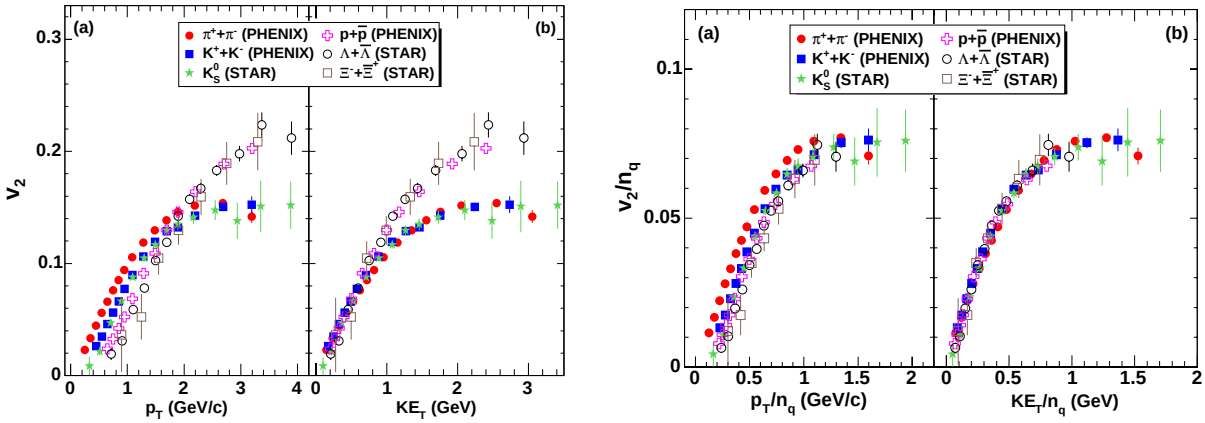

Figure 1.6: Left: (a) v_2 vs p_T and (b) v_2 vs KE_T. Right: (a) v_2/n_q vs p_T/n_q and (b) v_2/n_q vs KE_T/n_q. Both left and right for identified particle species in minimum bias Au+Au collisions [4].

KE_T. v_2 of presented particle species do not show mass ordering but scales up to $KE_T \approx 1$. In two discussed cases for $p_T \gtrsim 2$ and $KE_T \gtrsim 1$ v_2 split into two separate branches of mesons and baryons. Elliptic flow of baryons reaches higher values than elliptic flow of mesons.

Quite different observations are for v_2 scaled by the number of constituent quarks n_q what is presented on right panel of figure 1.6. v_2 for both mesons $n_f = 2$ and baryons $n_f = 3$ follow the same curve over the full range of KE_T/n_q. This result suggests that thermalization is connected with quark level rather than hadronic level. Plot (a) of the right panel does not show as good scaling of v_2/n_q with p_T/n_q as with KE_T/n_q due to effect of hydrodynamical mass ordering. This suggests that mass ordering is preserved over the range of linear increase of KE_T.

1.3.2 Suppression of high transverse momenta hadrons

Nuclear modification factor R_{AA} is defined as a ratio of the particle yield in nuclei-nuclei collisions to the particle yield in proton-proton collisions normalized by the number of binary collisions in nuclei-nuclei collisions N_{coll}^{AA}.

$$R_{AA}(p_T) = \frac{1}{N_{coll}^{AA}} \frac{d^2N^{AA}/dydp_T}{d^2N^{pp}/dydp_T} \tag{1.4}$$

If the medium created in A+A collisions has similar properties like in p+p collisions nuclear modification factor is constant and equal one. Any deviations from unity suggest that created media created in proton-proton and nuclei-nuclei collisions have different features. By analogy to R_{AA} R_{CP} - central to peripheral ratio is defined to compare central and peripheral A+A collisions.

$$R_{CP}(p_T) = \frac{N_{coll}^{peripheral}}{N_{coll}^{central}} \frac{d^2N^{central}dydp_T}{d^2N^{peripheral}dydp_T} \tag{1.5}$$

If matter created in central heavy ion collisions has similar properties to matter created in peripheral collisions no deviation from one should be observed.

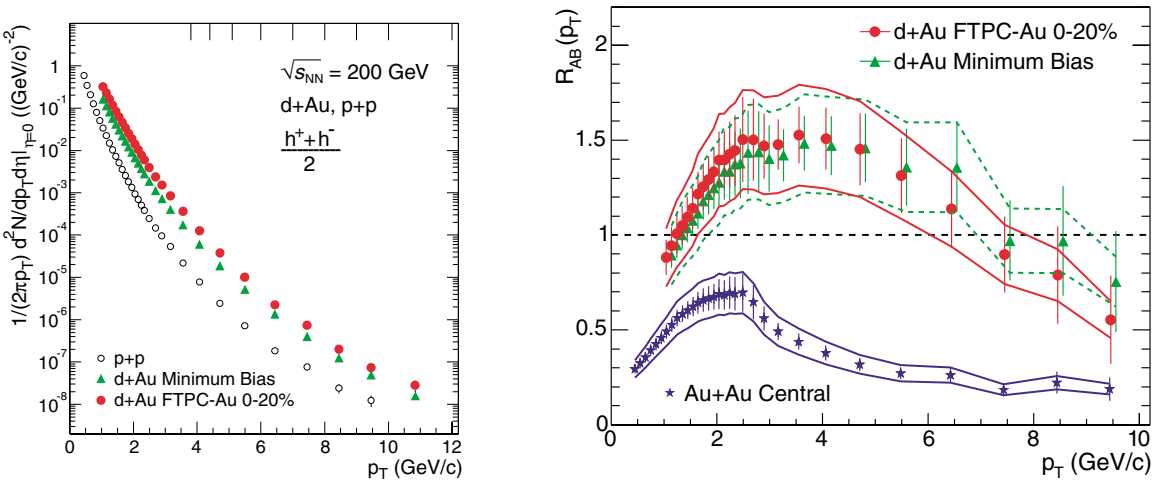

Figure 1.7: Left: inclusive p_T distribution for central and minimum bias d+Au collisions and non-diffractive p+p collisions. Right: Nuclear modification factor for d+Au collisions as well as central Au+Au collisions (minimum bias d+Au shifted 0.1GeV to the right for better visualization) [7].

Figure 1.7 shows results obtained by STAR Collaboration [7]. Left panel presents inclusive p_T distribution of charged hadrons for central and minimum bias d+Au collisions and non-diffractive p+p collisions. Right panel shows nuclear modification factor for the same d+Au data and central Au+Au data scaled by the p+p spectrum. Au+Au collisions reveals strong

suppression of hadron production for large transverse momenta and are significantly different than d+Au collisions which shows Cronin effect, inclusive yield is enhanced in $2GeV/c < p_T < 7GeV/c$. Suppression seen in Au+Au collisions is due to final state interactions with the dense matter created in high energy collision.

1.3.3 Jet quenching

Jet is defined by group of high p_T particles having similar momenta orientation. Jets are created at level of quarks and gluons when high energetic parton travels through matter. Its energy loss is sensitive to properties of created matter. If the matter is dense enough energetic partons may loose enough energy due to hard scattering to prevent emission of the jet what has been observed by STAR experiment in Au+Au collisions [7]. This phenomena is called jet quenching.

Figure 1.8 shows obtained results for central Au+Au, minimum bias p+p as well as minimum bias and central d+Au collisions. Plotted two particle azimuthal distribution of back-to-back jets is defined as

$$D(\Delta\phi) = \frac{1}{N_{trigger}} \frac{1}{\varepsilon} \frac{dN}{d\Delta\phi} \tag{1.6}$$

where $N_{trigger}$ is the number of trigger particles with $4GeV/c < p_T < 6GeV/c$ and ε is the tracking efficiency of the associated particles. As each trigger particle are correlated with all associated particles distributions shows peak at $\Delta\phi = 0$. Second "away-side" peak, opposite to the trigger jet at $\Delta\phi = \pi$ is observed only for $p+p$ and $d+Au$ collisions. Medium created in central Au+Au collisions is dense enough to quench the "away-side" jet. The "near-side" jet observed in central Au+Au collisions is believed to come from partons produced close to the surface of the surface of the medium and outward directed.

1.3.4 J/psi suppression

In 1986 it was suggested by T. Matsui, H. Satz [6] that production of J/ψ particle ($c\bar{c}$) could be suppressed in the quark-gluon plasma because of the screening of the confining potential.

First spectacular measurements of J/ψ suppression was done at SPS. Figure 1.9 shows the J/ψ over Drell-Yan cross-section ratio as a function of the average length L of the nuclear matter (traversed by the $c\bar{c}$ state compared to the normal nuclear absorption pattern (left panel) [5]. Right panel of this figure shows the same data but divided by the normal nuclear absorption pattern [5]. Both panels of figure 1.9 show clear suppression of J/ψ above the $L \approx 8\,fm$ what

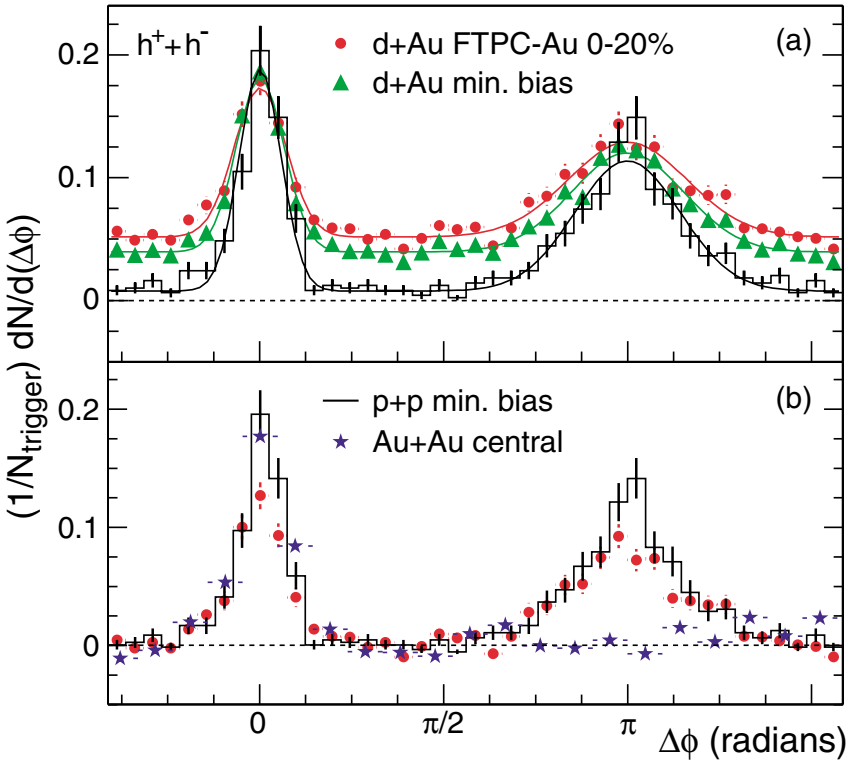

Figure 1.8: Two particle azimuthal distribution [7].

corresponds to energy density of the medium $\varepsilon \approx 2.5 GeV/fm^3$.

1.3.5 Strangeness enhancement

Strangeness is absent in the colliding nuclei so any strange hadron must be produced in the created source. Strange quarks can be produced in hadronic or partonic reactions, gluon fusion or quark-anti-quark annihilation. As s quark is relatively heavy (104^{+26}_{-34}MeV[1]) high energy is required for its production. Energy threshold for production of strange quark in hadronic channel is much higher than energy threshold in partonic reactions thus possible enhancement of the production of strange hadrons has been proposed to be a signature of existence of QGP.

Figure 1.10 presents enhancement of production in mid-rapidity region of strange baryons $\Lambda(uds)$, $\Xi^-(dss)$, $\Omega(sss)$ and their antiparticles as a function of number of participants N_{part} measured at the SPS and RHIC energies. Clear enhancement can be observed for all presented particles. Measured enhancement grows linearly for strange baryons with number of participants and its strength depends on strangeness of the particle ($S = 1,2,3$) and is higher for

[1] Particle Physics Booklet, July 2008

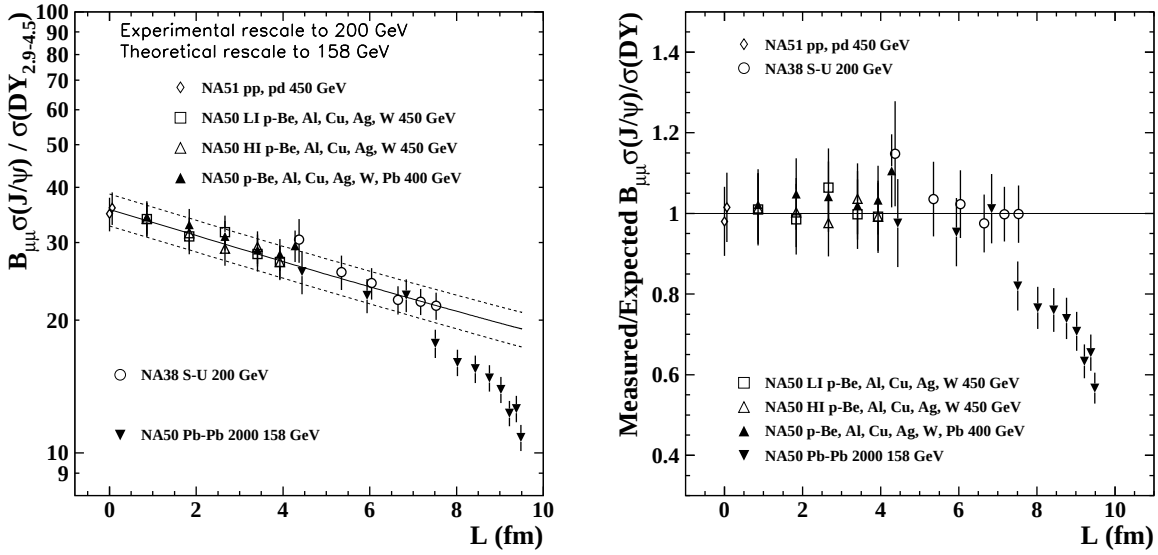

Figure 1.9: The J/ψ over Drell-Yan cross-section ratio as a function of L compared to the normal nuclear absorption pattern (left) and divided by the normal nuclear absorption pattern (right) [5].

particles with higher number of strange quarks. Data from RHIC is within the error bars at the same level as data from SPS. Enhancement of production of inclusive protons which are shown for a reference is constant over the investigated region of number of participants.

1.3.6 Dynamical fluctuations of strange particles multiplicities - "horn" structure

Methods of localizing the region of transition from hadron gas to quark gluon plasma have been proposed in [9]. The most spectacular is energy dependence of the ratio of strange particle multiplicities to pion multiplicities and an increase of the event-by-event fluctuations what can have characteristic behavior in the deconfinement transition region.

At energies lower than energy needed for a QGP formation the strangeness to entropy ratio increases with energy of the system due to the fact that mass of the strange degrees of freedom is higher than temperature of the created system. At the critical temperature this ratio is higher in the state which exists in the lower lower temperatures than in the state which exists above T_C. Thus in the mixed phase strangeness to entropy ratio decreases to value specific to QGP. This behavior has been called "horn" structure and is considered to be signature of the phase transition and a very good tool for a critical-point search.

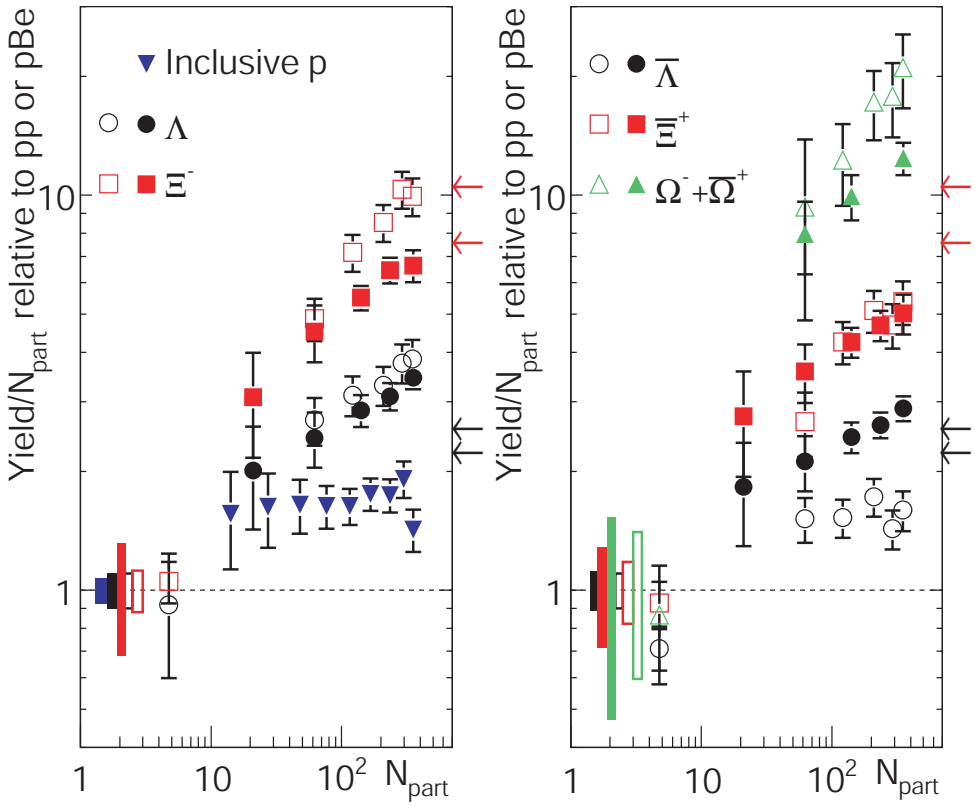

Figure 1.10: Yield enhancement of strange baryons Λ,$\bar{\Lambda}$, Ξ^-,$\bar{\Xi}^+$ and Ω,$\bar{\Omega}$ as a function of number of participants. Solid markers are for Au+Au at $\sqrt{s_{NN}} = 200GeV$, open markers are for Pb+Pb at $\sqrt{s_{NN}} = 17.3GeV$. Black and red arrows indicate predictions for Λ and Ξ. Blue triangles show inclusive protons to illustrate effects of non-strange baryons [8].

Figure 1.11 shows energy dependence of the relative strangeness production measured by the NA49 Collaboration[11] in Pb+Pb collisions at the SPS, data are also supplied with recalculated results from AGS. Ratio $E_S = (\langle\Lambda\rangle + \langle K + \bar{K}\rangle) / \langle\pi\rangle$ plotted as a function of collision energy reveals the "horn" structure predicted in the SMES (Statistical Model of the Early Stage) model [10]. Fast increase of the E_S ratio is followed by the turn out and decrease at about $\sqrt{s_{NN}}30GeV$. Reference data from proton reactions shows only monotonic increase over the measured collision energy.

Recently two World's leading heavy ion facilities SPS and RHIC began their projects of search for critical-point with energy and system scanning. The idea is to move in two dimensions with energy and baryon density on the phase diagram and localize the critical point (see figure 1.2).

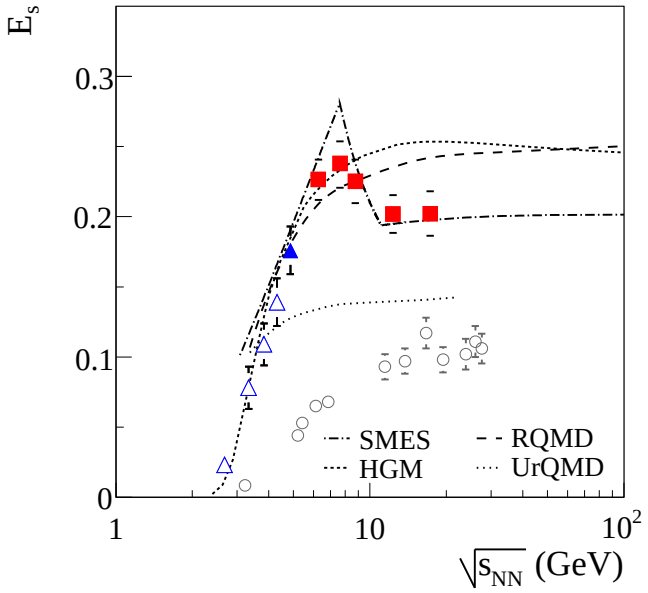

Figure 1.11: Energy dependence of the relative strangeness production as measured by the $E_S = (\langle\Lambda\rangle + \langle K + \bar{K}\rangle) / \langle\pi\rangle$ ratio in central Pb+Pb at SPS (red markers) and Au+Au at AGS (blue markers) collisions. Data from proton-(anti-)proton reactions (open circles) is plotted for comparison [11].

1.4 Models

Since the beginning of heavy ion collision physics scientists develop various models which are intended to describe particles production mechanism and interactions between produced particles. In this thesis two models UrQMD and Therminator are used for discussion and comparison with experimental results.

1.4.1 UrQMD - Ultrarelativistic Quantum Molecular Dynamics

The Ultrarelativistic Quantum Molecular Dynamics [12][13] - UrQMD - model is a microscopic transport model used for simulating heavy ion collisons in a wide range of collision energies from about $\sqrt{s_{NN}} = 1$GeV (SIS) up to top RHIC energy $\sqrt{s_{NN}} = 200$GeV. UrQMD is a multipurpose model for studying physical phenomena such as: creation of dense hadronic matter at high temperatures, multi-fragmentation processes, elliptic flow, electromagnetic probes, production of resonances or particle correlations. UrQMD model supports hydrodynamical evolu-

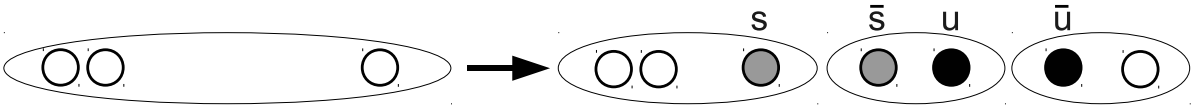

Figure 1.12: Particle production via baryon string fragmentation. Two quark-antiquark pairs ($u\bar{u}$ and $s\bar{s}$) are created in the color flux-tube between constituent diquark and the constituent quark.

tion of hot and dense stage of the collision. It also includes the Pythia for hard pQCD scatterings.

In UrQMD projectile and target are modeled by Fermi-gas ansatz. Nucleons are represented by Gaussian shaped density functions. A nucleon nucleon interaction is based on a non-relativistic Skyrme-type equation of state with additional Yukawa and Coulomb potentials. Hadron hadron collisions are performed stochastically. Cross section has geometrical interpretation as an area and collision between particles occurs when the relative distance between them d_{trans} is lower or equal $\sqrt{\sigma_{tot}/\pi}$, where σ_{tot} is a total cross section and depends on particle type and collision energy.

Production of particles takes place via decays of resonances or via strings excitations and fragmentations. At lower collision energies in c.m up to about 8-10GeV/nucleon production of particles is dominated by decays of resonances. For energies considered in this work strings excitations and fragmentations dominates process of particles production. An example of baryon string fragmentation excitation is presented on figure 1.12 where two quark-antiquark pairs are created. The leading diquark combines forms a hyperon with newly produced s quark, newly produced $\bar{s}$ and u quarks form a kaon and newly produced $\bar{u}$ quark with leading quark forms a pion.

UrQMD has implemented decay channels of all nucleon-, delta- and hyperon-resonances up to $2.25 GeV/c^2$ as well as meson decays. It is possible to prevent UrQMD from decaying selected particles.

UrQMD model is very flexible what helps in understanding of interactions and the dynamics of heavy ion collisions. It allows user to specify various parameters of the collision like energy of the collision, type of the collision head-on or fixed target, type of target and projectile or impact parameter. Among many parameters it is also possible to define equation of state or time of the evolution of the system.

1.4.2 THERMINATOR: THERMal heavy-IoN generATOR

Therminator[14] is an event generator based on Monte-Carlo generator which implements single freeze-out thermal models. Its primary goal is to study particle production in relativistic heavy ion collisions at the energies of SPS, RHIC or LHC.

Therminator implements a few expansion models based on Buda-Lund parametrization or Blast-Wave parametrization. All particles from Particle Data Tables are take into account during generation process. Positions and momenta of the particles are generated using Bose-Einstein or Fermi-Dirac distribution on the hypersurface. Produced particles do not interact with each other. Stable particles stream away along classical trajectories. Unstable particles are additionally decayed. Therminator supports two-body and tree-body decays. Decays of cascade particles proceed until only stable particles are present.

In this work emission function with quasi-linear velocity profile (equation 1.7)[15] was used:

$$\begin{aligned}\frac{dN}{dyd\varphi p_T dp_T d\alpha_{||} d\phi d\rho} &= \frac{\tau m_T \cosh\left(\alpha_{||}-y\right)}{(2\pi)^3}\times \\ &\left\{\exp\left[\beta\frac{m_T\cosh\left(\alpha_{||}-y\right)-p_T\nu_r\cos\left(\varphi-\phi\right)}{\sqrt{1-\nu_r^2}}-\beta\mu\right]\right\}^{-1} \quad (1.7)\end{aligned}$$

where the freeze-out hypersurface is defined as:

$$\begin{aligned}\tilde{\tau} &= \tau = const, \\ \nu_r &= \mathrm{tgh}\,\alpha_\perp(\xi) = \frac{\rho/\rho_{max}}{\nu_T+\rho/\rho_{max}} \quad (1.8)\end{aligned}$$

and τ, ρ_{max}, ν_T are parameters of the model.

A new version of `Therminator`+Lhyquid (`Therminator 2.0 beta`) with implemented hydrodynamics was also used for calculations done in this work. Although this version is still not officially released it can be considered as reliable as a number of publications based on its calculations were already published [16][17][18][19].

In this version hydrodynamical equations implement ideal-fluid, baryon free, boost invariant hydrodynamics. Initial energy density has a Gaussian form:

$$n(x,y) = \exp\left(-\frac{x^2}{2a^2}-\frac{y^2}{2b^2}\right) \quad (1.9)$$

where x and y are transverse coordinates and a and b are parameters (estimated from the GLISSANDO Glauber Monte Carlo calculations [21]) that depend on centrality of the collision.

Evolution of the system begins with formation of the massless partons and collisionless partonic free-streaming followed by a sudden equilibration. In the next step fully thermalized fluid begins its hydrodynamical evolution which starts at the emission proper time $\tau_0 = 0.25$fm. System freezes at the freezeout temperature T_f=145MeV, then statistical hadronization at the freeze-out hypersurface (hadrons are generated according to the Cooper-Frye formalism [22]) takes place and then all hadrons steams freely. Rescattering between hadrons is neglected. Unstable hadrons decay.

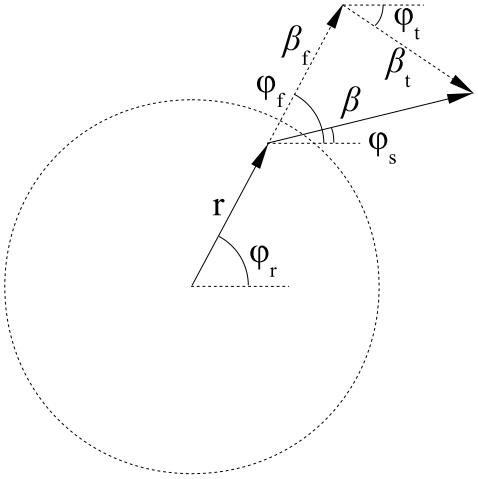

Figure 1.13: Diagram of the particle's velocity β decomposition into flow β_f and thermal β_t components. [19]

Investigating emission asymmetries is the main aim of this work. In hydrodynamical evolution of the system source can be divided into fluid cells. Each cell has its flow velocity $\boldsymbol{\beta_f}$. Particles emitted from such cell have the same flow velocity. In addition to $\boldsymbol{\beta_f}$ each particle gets its own thermal velocity $\boldsymbol{\beta_t}$ which have random direction ϕ_t (see figure 1.13. Component of the emission point, of a single particle, parallel to its the velocity has the form [19][20]:

$$x_{out} = \frac{\boldsymbol{x\beta}}{\beta} = \frac{r\left(\beta_f + \beta_t \cos\left(\phi_t - \phi_f\right)\right)}{\beta} \tag{1.10}$$

where $\boldsymbol{\beta}$ is a single particle velocity.

Mean emission point, averaged over particles at fixed β, for Gaussian density profile $\exp\left(-r_t^2/2r_0^2\right)$ can be expressed as:

$$\langle x_{out}\rangle = \frac{\langle r\beta_f\rangle}{\left\langle\sqrt{\beta_t^2+\beta_f^2}\right\rangle} = \frac{r_0\beta_0\beta}{\beta_0^2 + T/m_t} \tag{1.11}$$

where r_0 is a radius and $\beta_f = \beta_0 r/r_0$. The local thermal momentum distribution is characterized by temperature T.

Equation 1.11 has explicitly given element of a thermal velocity. We can see that maximal possible shift between emission points in *out* is for zero thermal velocity.

As explained in [19], in general when two particles, lighter and heavier emitted from the same fluid cell have the same flow velocity but different momenta. Total velocity of them is additionally increased by thermal, momentum dependent component. Thus for the same p_T thermal velocity obtained by lighter particle is higher than a thermal velocity obtained by heavier particle. Total velocity of a lighter particle is less correlated with its emission point than in case of heavier one. In the system with no flow mean emission point of any particle is zero. When thermal (random) component dominates over flow (correlated) component of the particle velocity than mean emission points are also zero. When β_f dominates over β_t then shift of the mean emission point is observed but as the β_f of both particles is the same, centers of the source of the lighter particle is very close to the center of the source of the heavier particle. Asymmetry in the *out* direction between average emission points of lighter and heavier particles can be observed when flow and thermal components of the particle velocity are comparable.

Chapter 2

Two particle correlations with small relative velocities

In the 1950s R. Hanbury Brown and R.Q. Twiss proposed the new technique of measuring angular dimensions of bright visual stars [23][24]. It was based on the idea that the time of arrival of photons in coherent beams of light is correlated and this phenomenon can be used an interferometer to measure the apparent angular diameter of stars. Information about the size of the emitting source can be calculated from opening angle of momentum vectors which can be extracted from the two photon correlation function as a function of a space-time distance of the detected photons.

A few years later correlation effect in angular distributions of pions, related to the Bose-Einstein statistics was observed in the antiproton-proton anihilation process [25]. Later on Kopylov and Podgoretsky formulated a method of extracting space-time characteristics of the source [26].

Both techniques use measurable momentum-space structure for description of non measurable space-time structure of the investigated object but in case of the astronomy the effect that causes correlation between photons takes place in the detector and in case of nuclear collisions the correlation between particles has its origin in the source.

2.1 Identical particles correlations

The momentum correlations of non-interacting particles emitted in nuclear collisions are influenced by the quantum statistics effect. If the particles are bosons they obey Bose-Einstein

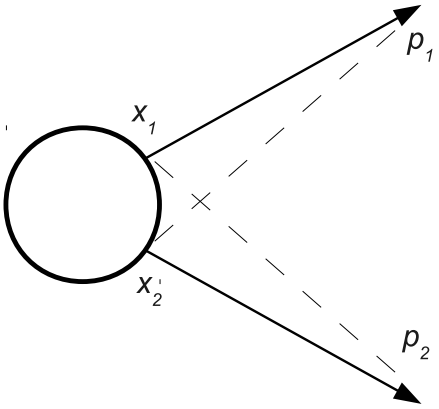

Figure 2.1: Identical particles are indistinguishable thus two scenarios of registering them are equally probable.

statistics and if the particles are fermions they satisfy Fermi-Dirac statistics. Interacting particles are also influenced by final state interaction which may come from Coulomb or strong forces.

Identical particles are indistinguishable therefore the plane wave function (Eq. 2.1) of the pair needs to cover two scenarios - depicted on the figure 2.1. The first one when particles with momenta p_1 and p_2 are emitted from points x_1 and x_2 respectively and the second one when they are emitted from x_2 and x_1 respectively. Quantum mechanics requires the wave function to be symmetrized for bosons and anti-symmetrized for fermions.

$$\Psi_{12}(\boldsymbol{x_1},\boldsymbol{p_1},\boldsymbol{x_2},\boldsymbol{p_2}) = \frac{1}{\sqrt{2}}\left[\exp\left(i\boldsymbol{p_1}\cdot\boldsymbol{x_1}+i\boldsymbol{p_2}\cdot\boldsymbol{x_2}\right)\pm\exp\left(i\boldsymbol{p_1}\cdot\boldsymbol{x_2}+i\boldsymbol{p_2}\cdot\boldsymbol{x_1}\right)\right] \tag{2.1}$$

The probability of registering two particles in such state can be expressed by

$$\mathcal{P}_2(\boldsymbol{p_1},\boldsymbol{p_2}) = E_1E_2\frac{dN}{d^3p_1d^3p_2} = \int d^4x_1d^4x_2S(x_1,\boldsymbol{p_1})S(x_2,\boldsymbol{p_2})\left|\Psi_{12}\right|^2 \tag{2.2}$$

where $S(x,p)$ is the single particle Wigner space-phase density. One-particle spectra are defined by

$$\mathcal{P}_1(\boldsymbol{p_1}) = E_p\frac{dN}{d^3p} = \int d^4xS(x,\boldsymbol{p}) \tag{2.3}$$

Two particle correlation function is defined as a ratio of two-particle and one-particle spectra (Eq. 2.4)

$$C(\boldsymbol{p_1},\boldsymbol{p_2}) = \mathcal{N}\frac{\mathcal{P}_2(\boldsymbol{p_1},\boldsymbol{p_2})}{\mathcal{P}_1(\boldsymbol{p_1})\mathcal{P}_1(\boldsymbol{p_2})} \tag{2.4}$$

where $\mathcal{N}$ is the proportionality factor which is specified by relating particle spectra to inclusive differential cross sections.

$$\mathcal{P}_1(\boldsymbol{p_1}) = E_p \frac{1}{\sigma}\frac{d\sigma_p}{d^3p} \tag{2.5}$$

$$\mathcal{P}_2(\boldsymbol{p_1}) = E_1 E_2 \frac{1}{\sigma}\frac{d\sigma_{12}}{d^3p_1 d^3p_2} \tag{2.6}$$

Particle spectra can be also expressed in terms of creation and annihilation operators:

$$\mathcal{P}_1(\boldsymbol{p_1}) = E\langle \hat{a}_p^+ \hat{a}_p \rangle \tag{2.7}$$

$$\mathcal{P}_2(\boldsymbol{p_1}) = E_1 E_2 \langle \hat{a}_{p_1}^+ \hat{a}_{p_2}^+ \hat{a}_{p_1} \hat{a}_{p_2} \rangle \tag{2.8}$$

and they can be normalized by

$$\int \frac{d^3p}{E} \mathcal{P}_1(\boldsymbol{p}) = \langle \hat{N} \rangle \tag{2.9}$$

$$\int \frac{d^3p_1}{E_1}\frac{d^3p_2}{E_2} \mathcal{P}_{12}(\boldsymbol{p_1}, \boldsymbol{p_2}) = \langle \hat{N}(\hat{N}-1) \rangle \tag{2.10}$$

where $\hat{N}$ is the number operator. Equations 2.9 and 2.10 define proportionality factor used in equation 2.4

$$\mathcal{N} = \frac{\langle \hat{N} \rangle}{\langle \hat{N}(\hat{N}-1) \rangle} \tag{2.11}$$

If we introduce two vectors of average momentum $K = (p_1 + p_2)/2$ and relative momentum $q = p_1 - p_2$ than we can replace $S(x_1, p_1)S(x_2, p_2)$ by $S(x_1, K - \frac{1}{2}q)S(x_2, K - \frac{1}{2}q)$ and following [27] for small relative momenta we can apply the following smoothness approximation

$$S(x_1, K - \frac{1}{2}q)S(x_2, K - \frac{1}{2}q) \approx S(x_1, K)S(x_2, K) \tag{2.12}$$

Finally the equation 2.4 can be expressed as follows.

$$C(\boldsymbol{q}, \boldsymbol{K}) = 1 \pm \frac{\left| \int d^4x S(x, \boldsymbol{K}) e^{iqx} \right|^2}{\left| \int d^4x S(x, \boldsymbol{K}) \right|^2} \tag{2.13}$$

2.1.1 Gaussian parametrization of the source

In order to extract quantitative information from the measured correlation function the parametrization of the emission function $S(x, K)$ needs to be assumed. The simplest is a Gaussian parametrization of a source:

$$S(x,t) \approx \exp\left(-\frac{x^2}{2r_0^2} - \frac{t^2}{\tau_0^2} \right) \tag{2.14}$$

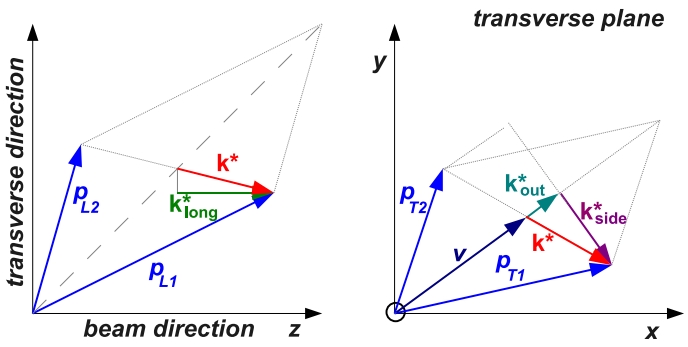

Figure 2.2: Decomposition of k^* into $out, side, long$ components.

Equation 2.14 does not depend on the average momentum K of the pair and the correlation function can be written as

$$C(\boldsymbol{q}, q_0) = 1 + \lambda \exp\left(-\frac{\boldsymbol{q}^2 R^2}{2} - \frac{q_0^2 \tau^2}{2}\right) \tag{2.15}$$

where $q_0 = E_1 - E_2$ is the energy component conjugated to the emission duration. Parameter λ is the phenomenological parameter which takes values between 0 and 1 and describes strength of the correlation.

One-dimensional correlation functions are often calculated with respect to Lorentz invariant variable $q_{inv} = \sqrt{q_0^2 - \boldsymbol{q}^2}$. Correlation function then takes the form:

$$C(q_{inv}) = \lambda \exp\left(-q_{int}^2 R^2\right) \tag{2.16}$$

2.1.2 *Out-side-long* coordinate system

Often choice of the coordinate system in femtoscopic analyzes is the Bertsch-Pratt[28][29] *out-side-long* parametrization where *long* is directed along the beam axis, *out* and *side* lay in transverse plane. *Out* is along the total momentum of the pair and *side* is perpendicular to it. Schematic view of *out*, *side* and *long* components is presented on figure 2.2. Vector k^* decomposed on this figure is half of the vector q and is used in construction of the non-identical particle correlation functions which are discussed in this thesis.

Correlation function can be now rewritten as

$$C(\boldsymbol{q}) = 1 + \lambda \exp(-q_O^2 R_O^2 - q_S^2 R_S^2 - q_L^2 R_L^2) \tag{2.17}$$

2.1.3 Final State Interaction - Coulomb and strong

Coulomb part of the pair wave function of charged particles which depends on relative distance between emission points can be written in the following form [30]:

$$\psi^{c}_{-k^*}(r^*) = e^{i\delta_c}\sqrt{A_c(\eta)}e^{-ik^*r^*}F(-i\eta,1,i\xi) \tag{2.18}$$

where $\xi = k^*r^* + \boldsymbol{k^*}\cdot\boldsymbol{r^*} \equiv \rho(1+\cos\theta^*)$, $\rho = k^*r^*$, $\eta = 1/(k^*a)$ and $a = 1/(\mu z_1 z_2 e^2)$ is the Bohr radius, $\mu = m_1m_2/(m_1+m_2)$ is the reduced mass, $\delta_c = \arg\Gamma(1+i/(k^*a))$ [34] is the Coulomb s-wave phase shift, k^* is half of the relative momentum in pair rest frame PRF, r^* is the relative separation between emission points and θ^* is the angle between k^* and r^*.

A_c is the Gammov factor which describes the Coulomb interaction at 0 relative distance between emitted particles:

$$A_c(\eta) = \left|\psi^{c}_{-k^*}(0)\right|^2 = 2\pi\eta\left(\exp(2\pi\eta)-1\right)^{-1} \tag{2.19}$$

and $F(\alpha,1,z)$ is the confluent hypergeometric function:

$$F(\alpha,1,z) = 1 + \frac{\alpha z}{1!^2} + \frac{\alpha(\alpha+1)z^2}{2!^2} + ... \tag{2.20}$$

If the particles interact also by strong interaction a pair wave function needs to be supplied additional term responsible for description of it [31].

$$\psi^{c}_{-k^*}(r^*) = e^{i\delta_c}\sqrt{A_c(\eta)}\left[e^{-ik^*r^*}F(-i\eta,1,i\xi) + f_c(k^*)\frac{\tilde{G}(\rho,\eta)}{r^*}\right] \tag{2.21}$$

where $\tilde{G} = \sqrt{A_c}(G_0 + iF_0)$ is a combination of the regular (F_0) and singular (G_0) s-wave Coulomb functions.

$$f_c(k^*) = \frac{f(k^*)}{A_c(\eta)} = \left[f_0^{-1} + \frac{1}{2}d_0k^{*2} - \frac{2h(\eta) + iA_c(\eta)/\eta}{a_c}\right]^{-1} \tag{2.22}$$

$f(k^*)$ is the amplitude of the low-energy s-wave elastic scattering due to the short-range interaction renormalized by the long-range Coulomb forces. Function $h(\eta)$ is expressed through the digamma function, but for $|\eta| < 0.3$ can be approximated by

$$h(x) = \frac{1}{x^2}\sum_{n=0}^{\infty}\frac{1}{n(n^2+x^{-2})} - C + \ln|x| \tag{2.23}$$

and finally C is the Euler constant.

Interaction between pions and protons is dominated by Coulomb interaction. Strong component of FSI is negligible thus correlation function at small relative momenta $k^*r^* < 1$ and for $r^* \ll |a|$ can be approximated by [33]:

$$C(k^*) = A_c(\eta)\left[1 + 2\left\langle r^*(1+\cos\theta^*)\right\rangle/a + ...\right] \tag{2.24}$$

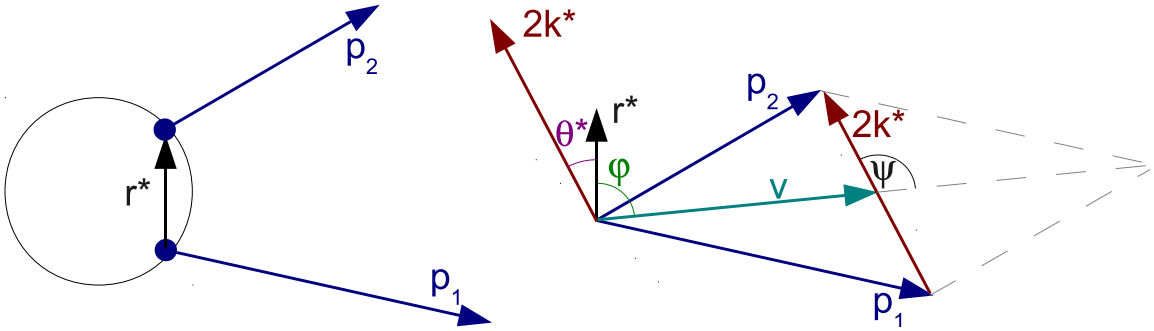

Figure 2.3: Kinematical relations between separation of the emission points and momenta of the particles.

2.2 Correlation function of non-identical particles

Correlations between non-identical particles are sensitive to differences between space-time emission points of different particle species. Correlation function can be approximated by equation 2.24. Element $r^*(1+\cos\theta^*)$ averaged over space defines space-time structure of the source but both quantities r^* and θ^* are not accessible in the experiment. Taking into account that the final state interaction which determines correlation function depends on the orientation of the relative 4-coordinates of the emission point through the scalar product of $\boldsymbol{k^*}\cdot\boldsymbol{r^*}$ we can measure space-time asymmetry of the source [33][34][35]. Figure 2.3 describes relations between quantities not measurable in the experiment and experimentally accessible quantities.

Two particles are emitted with momenta $\boldsymbol{p_1}$ and $\boldsymbol{p_2}$. Separation between them is defined by vector $\boldsymbol{r^*}$. Vector $\boldsymbol{k^*}$ is defined as half of the relative momentum of the pair what is momentum of the first particle in pair rest frame PRF. Velocity of the pair keeps the direction of total momentum of the pair and creates an angle Ψ with vector $\boldsymbol{k^*}$. θ^* is an angle between $\boldsymbol{r^*}$ and $\boldsymbol{k^*}$ and φ is an angle between $\boldsymbol{r^*}$ and $\boldsymbol{v}$.

To access information about such asymmetry in the outward direction (*out*) one can construct two correlation functions C^+ for $\cos(\Psi)>0$ and C^- for $\cos(\Psi)<0$ what corresponds to $k^*_{out}=\boldsymbol{k^*}\cdot\boldsymbol{v}_\perp/v_\perp>0$ and $k^*_{out}=\boldsymbol{k^*}\cdot\boldsymbol{v}_\perp/v_\perp<0$. If particles are in the average emitted from the same positions, ratio of C^+/C^- measures mean relative emission time. If in the average there is no delay between emission of two particles the ratio C^+/C^- measures spacial shift between average emission points. In general combination of these two cases:

$$< r^* >= \gamma_T(\Delta r-\beta_T\Delta t) \tag{2.25}$$

which cannot be separated is measured. Δr and Δt are quantities in centrum mass system CMS. Relation between PRF and CMS is defined by the Lorentz factor $\gamma_T = 1/\sqrt{(1-v_T)}$. Once the relations from figure 2.3 are defined the equation 2.24 can be rewritten as [33]

$$\begin{aligned} C(k^*) &= A_c(\eta)[1+2\langle r^*\rangle/a + \\ &\quad 2\cos\Psi\langle r^*_{out}\rangle/a + \\ &\quad 2\sin\Psi\left(\sin\phi\langle r^*_{side}\rangle + \cos\phi\left\langle r^*_{long}\right\rangle\right)/a + \cdots] \end{aligned} \tag{2.26}$$

Then for $r^*_{side} = r^*_{long} = 0$ and $k^* \to 0$ "double-ratio" C^+/C^- takes the form [33]

$$\frac{C^+}{C^-} \approx 1 + 2\left(\langle\cos\Psi\rangle_- - \langle\cos\Psi\rangle_+\right)\langle r^*_{out}\rangle/a \tag{2.27}$$

where $+$ and $-$ subscripts indicates averaging over positive and negative orientations of k^*_{out}. Deviation from unity (peak or dip) for small k^* is conjugated with space-time asymmetry of the source.

2.3 Constructing experimental correlation function

Experimental correlation function is constructed as a ratio of two particle distribution of particles coming from the same event $N(q)$ (correlated particles) to the two particle distribution of particles coming from different events $D(q)$ (uncorrelated particles). Correlation function is required to satisfy the condition that it is constant and equal 1 for large q so denominator $D(q)$ should be properly rescaled. Constant c is the correlation function normalization factor.

$$C(q) = \frac{N(q)}{cD(q)} \tag{2.28}$$

Two particle distributions are constructed as a functions of pair relative momentum q in case of identical particles or half of the relative momentum k^* for non-identical particles.

2.4 Correlation function constructed in spherical harmonics

Structure of the source can be much more efficiently explored by constructing correlation function using spherical harmonic decomposition [36]. Acceptance of the detector does not cover full phase space of vector k^* what results in difficulties in calculating harmonic moments from 3-dimensional correlation function. To resolve such problems method of constructing raw pair

distributions directly in spherical harmonics has been used in this work [37] and will be briefly described below.

Correlation function $C(\boldsymbol{k^*})$ is defined as a ratio of two particle distribution of correlated particles $T(\boldsymbol{k^*})$ do the ratio of two particle distribution of uncorrelated particles $M(\boldsymbol{k^*})$

$$C(\boldsymbol{k^*}) = \frac{T(\boldsymbol{k^*})}{M(\boldsymbol{k^*})} \tag{2.29}$$

each of the elements of this equation can be decomposed into SH

$$T(\boldsymbol{k^*}) = 2\sqrt{\pi}\sum_{lm} T_{lm}(k^*)Y_{lm}(\theta,\phi) \tag{2.30}$$

where

$$T_{lm}(k^*) = \frac{1}{2\sqrt{\pi}}\int d\theta d\phi T(\boldsymbol{k^*})Y^*_{lm}(\theta,\phi) \tag{2.31}$$

experimental conditions require following approximation

$$T_{lm}(k^*_n) \approx \frac{2\sqrt{\pi}}{N}\sum_{i=1}^{N}\begin{cases} Y^*_{lm}(\theta_{k^*_i},\phi_{k^*_i}) & \text{if } k^*_i \text{ in bin } n, \\ 0 & \text{otherwise} \end{cases} \tag{2.32}$$

where N is the number of pairs in calculated distribution. Then T_{lm} takes the form

$$T_{lm}(k^*) = \sum_{l''m''} \tilde{M}_{lml'm'}(k^*)C_{l''m''}(k^*) \tag{2.33}$$

where matrix $\tilde{\boldsymbol{M}}_{k^*}$ is written as

$$\begin{aligned} \tilde{M}_{lml''m''}(k^*) \quad = \quad & \sum_{l'm'} M_{l'm'}(k^*) \\ & (-1)^m\sqrt{(2l+1)(2l'+1)(2l''+1)} \\ & \begin{pmatrix} l & l' & l'' \\ 0 & 0 & 0 \end{pmatrix}\begin{pmatrix} l & l' & l'' \\ -m & m' & m'' \end{pmatrix} \end{aligned} \tag{2.34}$$

Such defined equation 2.33 can be used for direct computing of $C_{lm}(k^*)$ components.

Due to symmetry reasons number of relevant components are reduced. Detailed discussion can be found in [36]. In analysis presented in this thesis collisions of identical ions (Au+Au) are considered and measurement covers symmetric mid-rapidity region thus odd $(l+m)$ components vanish (polar angle symmetry). Due to the fact that measurement is integrated over the reaction plane all imaginary components also vanish. Vanishing components of the calculated function can be treated as an analysis and data quality test.

C_{00} component directly probes size of the system, is sensitive to FSI interaction and reveals attractive or repulsive behavior of Coulomb interaction. ReC_{11} keeps information about asymmetry of the source. C_{20} and ReC_{22} elements indicate that size of the system in three directions *out*, *side* and *long* are not the same. Higher order elements are not significant to this analysis.

Chapter 3

Overview of femtoscopic analyzes

3.1 STAR results - meson-meson systems

System of identical pions is the most extensively investigated system in femtoscopic measurements. The first STAR measurements of pion-pion correlations were done in *year*1 dataset of Au+Au collisions at $\sqrt{s_{NN}} = 130GeV$ then in $\sqrt{s_{NN}} = 200GeV$. Recently such studies have been supplemented with measurements done in Cu+Cu at $\sqrt{s_{NN}} = 62.4GeV$ and $\sqrt{s_{NN}} = 200GeV$ as well as Au+Au at $\sqrt{s_{NN}} = 62.4GeV$. Figures 3.1 and 3.2 show the latest results on pion interferometry published in 2009.

As shown on figure 3.1 femtoscopic radii grow as expected with increasing centrality for both colliding systems. No centrality dependence is observed for λ parameter and R_{out}/R_{side} ratio. HBT radii and R_{out}/R_{side} decreases with transverse mass. Decrease of *out* and *side* components is described by transverse flow. Decrease of *long* component is correlated with longitudinal flow. Parameter λ grows with increasing transverse mass of the investigated system m_T. This is due to decreasing contribution of pions produced from long lived resonance decays at higher transverse momenta [38]. What is not presented on the cited figures but mentioned by the authors of [38] is that parameter λ and ratio R_{out}/R_{side} are higher for collisions at $\sqrt{s_{NN}} = 62.4GeV$ than for $\sqrt{s_{NN}} = 200GeV$.

Left panel of figure 3.2 show ratios of extracted radii for central Au+Au and Cu+Cu collisions at $\sqrt{s_{NN}}$=200GeV and 62.4 GeV. Ratios of Au+Au to Au+Au as well as Cu+Cu to Cu+Cu are close to unity. Ratios of radii extracted from Au+Au collisions to radii from Cu+Cu collisions are at the level about 1.5. All ratios do not show any dependence on transverse mass what can be understood in terms of models which assume the radii proportional to $A^{1/3}$, where A is

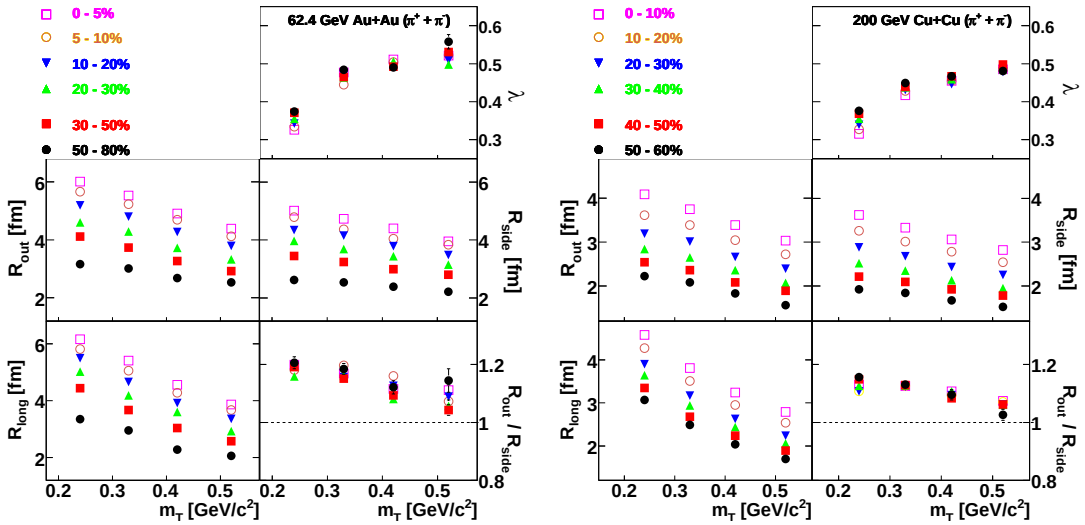

Figure 3.1: Femtoscopic parameters R_{out}, R_{side}, R_{long}, R_{out}/R_{side} and λ as a function of transverse mass m_T and their centrality dependence for Au+Au collisions at $\sqrt{s_{NN}} = 62.4GeV$ (left panel) and Cu+Cu collisions at $\sqrt{s_{NN}} = 200GeV$ (right panel) [38].

the atomic mass number of the colliding nuclei [38].

Estimated pion freeze-out volume ($V_f \propto R^2_{side}R_{long}$, $V_f \propto R_{out}R_{side}R_{long}$) as a function of charged particle multiplicity density for Au+Au and Cu+Cu collisions is presented on right panel of figure 3.2 [38]. As the system size decreases with transverse mass authors of this analysis used for the volume freeze-out estimation the lowest m_T bin which corresponds to k_T region from 150 to 250 MeV/c. Common linear dependence is observed for all four combinations of colliding nuclei and energy of the collision.

The energy dependence of the pion freeze-out volume in heavy ion collisions calculated for wide range of energies from energies of AGS up to energies of RHIC is presented on figure 3.3. AGS measurements show monotonic decrease of the volume while for SPS and RHIC energies monotonic increase is observed. Authors of the [38] explain this effect in therms of mean free path length of pions at freeze-out (eqn. 3.1)

$$\lambda_f = \frac{1}{\rho_f \sigma} = \frac{V_f}{N\sigma} \tag{3.1}$$

where ρ_f is the freeze-out density described as the number of pions N in the freeze-out volume V_f and the σ is the total cross section for pions to interact with the medium. $N\sigma$ can be expressed as a sum of pion-pion and pion-nucleon contributions. At the energies available at the AGS pion-nucleon cross section is larger than the pion-pion cross seciton, also number of nucleons in mid-rapidity region is larger than the number of pions. Thus the decrease of the number of

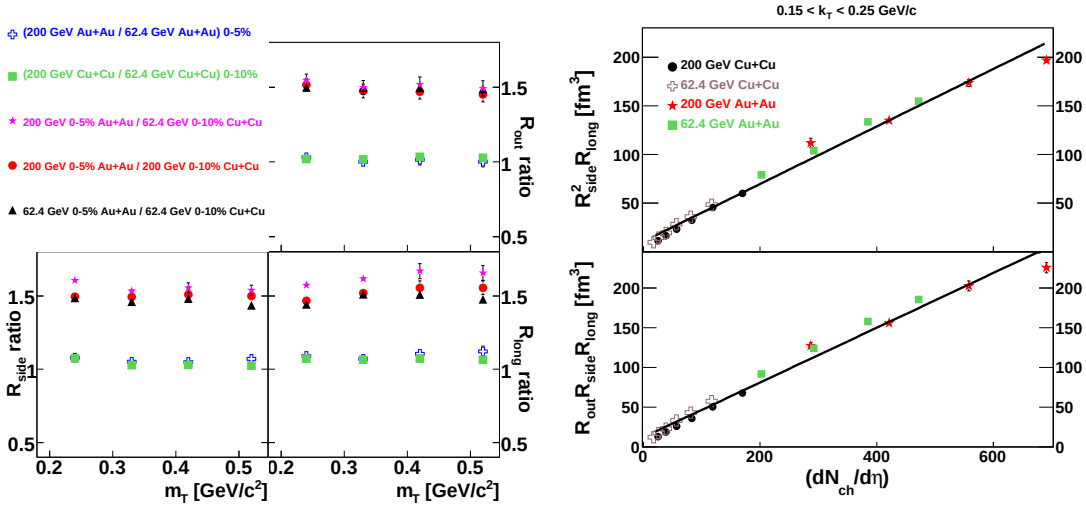

Figure 3.2: Left: Ratios of femtoscopic radii at central collisions for Au+Au and Cu+Cu collisions at $\sqrt{s_{NN}} = 200$ and $62.4GeV$ as a function of m_T [38]. Right: Pion freeze-out volume estimates as a function of charged particle multiplicity density for Au+Au and Cu+Cu collisions for $\sqrt{s_{NN}} = 62.4GeV$ and $\sqrt{s_{NN}} = 200GeV$ [38].

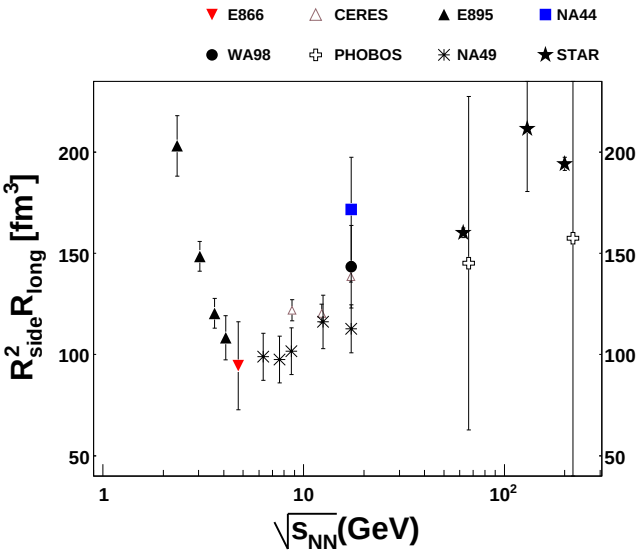

Figure 3.3: The energy dependence of the pion freeze-out volume in mid-rapidity region in heavy ion collisions for wide range of energies from AGS up to RHIC [38]. Data are for Au+Au, Pb+Pb and Au+Pb collisions.

	σ (fm)	$\langle \Delta r^*_{out} \rangle$ (fm)
STAR Data	$12 \pm 0.4^{+2.2}_{-3}$	$-5.6 \pm 0.6^{+1.9}_{-1.3}$
RQMD	11.8 ± 0.4	-8.0 ± 0.6
Blast-Wave	9.9 ± 0.1	-6.9 ± 0.3

Table 3.1: Gaussian 3-dimensional fit results in pair rest frame for pion-kaon correlation functions for central Au+Au collisions at $\sqrt{s_{NN}} = 200$GeV [39].

nucleons with energy results in decrease of observed freeze-out volume. At the SPS and RHIC energies contribution to the $N\sigma$ therm from pion-pion dominates thus monotonic increase of the V_f with energy is observed.

Figure 3.4 shows pion-kaon correlation functions measured in Au+Au collisions at $\sqrt{s_{NN}} = 130 GeV$ - the first results of non-identical particle correlations measured by STAR Collaboration. Presented results suggest that pions and kaons are not emitted, in the average from the same space-time emission point. Top panels of figure 3.4 show the average of the $C_+(k^*)$ (pions catch up witch kaons) and $C_-(k^*)$ (pions move away from kaons). For like sign pairs coulomb interaction is repulsive thus correlation between particles in low k^* values is suppressed. For unlike sign pairs coulomb interaction is attractive thus correlation is increased. Middle and bottom panels show the ratios of C_+/C_- for *out*, *side*, and *long* directions of vector k^*. Ratios calculated with respect to k^*_{side} and k^*_{long} are equal to unity within the statistical errors what suggest that the average separation $\langle r^*_{side} \rangle = \langle r^*_{long} \rangle = 0$. Clear evidence for space-time asymmetry is visible in C_+/C_- calculated with respect to sign of k^*_{out}. Ratio is below one for like-sign pairs and above one for unlike sign pairs. Table 3.1 presents fit results to the experimental data as well as Blast-Wave and RQMD functions.

The first statistically meaningful femtoscopic analysis of $K^0 - K^0$ was done in Au+Au collisions at $\sqrt{s_{NN}} = 200 GeV$ by the STAR Collaboration [40]. Correlation of neutral kaons is dominated by quantum statistics and final state interaction which do not contain Coulomb part. Kaon interferometry suffers less than pions from resonance decays and thus provide cleaner signal for femtoscopic studies. Figure 3.5 shows measured raw correlation function as well as corrected on purity and momentum resolution. Fit results give size of the source $R = 4.09 \pm 0.46 \pm (stat) 0.39 (sys) fm$ and chaoticity parameter $\lambda = 0.92 \pm 0.23 (stat) \pm 0.13 (sys)$ at mean transverse mass $\langle m_T \rangle = 1.07 GeV/c^2$.

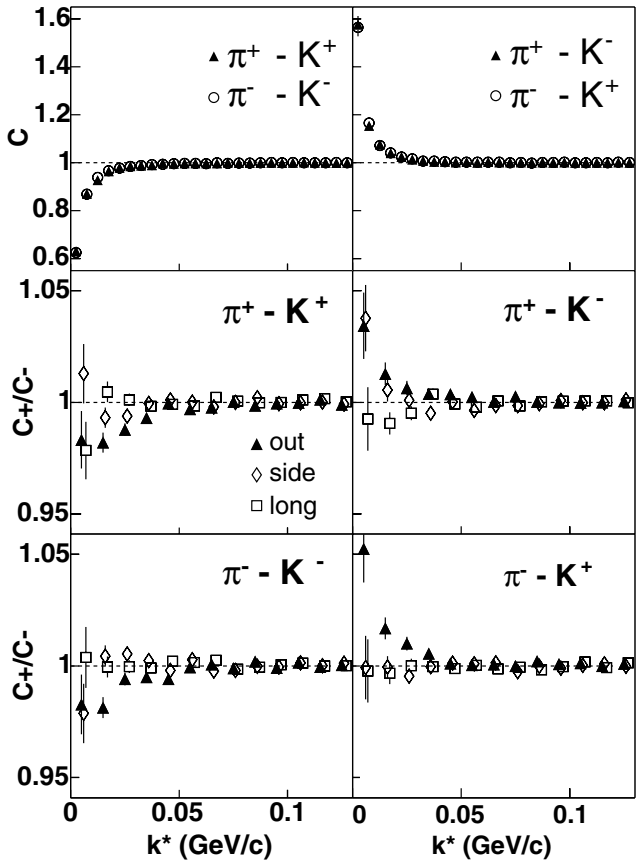

Figure 3.4: Pion-kaon correlation functions measured by STAR in Au+Au collisions at $\sqrt{s_{NN}} = 130GeV$. Top panels: the average of the $C_+(k^*)$ and $C_-(k^*)$. Middle and bottom panels: ratio of the $C_+(k^*)$ and $C_-(k^*)$ defined with the sign of the projections, k^*_{out}, k^*_{side}, k^*_{long} [39].

3.2 STAR analyzes - baryon-baryon systems

Study of proton-lambda system is presented on figure 3.6 which shows measured correlation functions corrected on purity and momentum resolution. Data shows unexpected difference in radii between $p-\Lambda(\bar{p}-\bar{\Lambda})$ and $p-\bar{\Lambda}(\bar{p}-\Lambda)$. This may imply that baryon-antibaryon pairs are created close in space what is not in baryon-baryon pairs. Authors of this analysis also suggests that measured difference in system size between radii extracted from $p-\Lambda(\bar{p}-\bar{\Lambda})$ and $p-\bar{\Lambda}(\bar{p}-\Lambda)$ may arise from the improper treatment of the purity correction. Non-primary particles may carry residual correlations from their parents. This effect may be relatively strong in case of protons. Massive particles have smaller curvature thus significant number of protons which come from weak decays points to primary vertex what makes them impossible to remove them using *DCA* cuts.

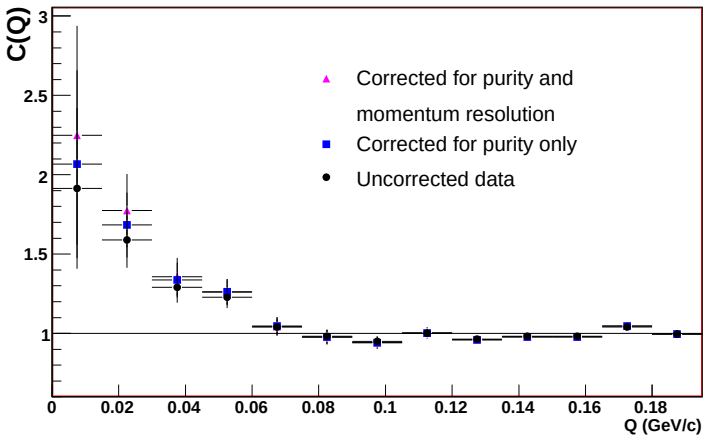

Figure 3.5: The $K^0 - K^0$ correlation functions. Solid black circles show raw uncorrected experimental data, blue squares show purity corrected data and pink triangles represent purity corrected and momentum resolution corrected data [40].

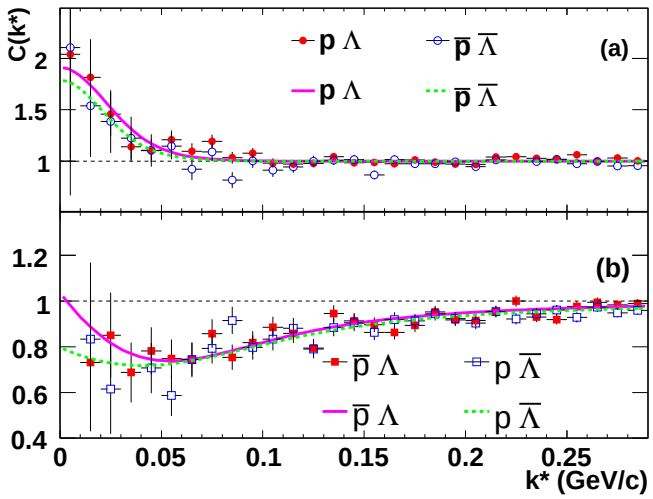

Figure 3.6: Correlation functions (points) corrected on purity and momentum resolution for $p-\Lambda$, $p-\bar{\Lambda}$, $\bar{p}-\Lambda$ and $\bar{p}-\bar{\Lambda}$ and corresponding fits (lines) for Au+Au collisions at $\sqrt{s_{NN}} = 200GeV$ [41].

	p-p [fm]	$\bar{p}-\bar{p}$ [fm]	$p-\bar{p}$ [fm]
central 0-10%	$4.51^{+0.07+0.15}_{-0.07-0.19}$	$5.05^{+0.08+0.22}_{-0.08-0.21}$	$4.08^{+0.09+0.12}_{-0.09-0.13}$
mid-central 10-30%	$3.82^{+0.09+0.11}_{-0.09-0.10}$	$4.02^{+0.09+0.24}_{-0.09-0.23}$	$3.27^{+0.10+0.13}_{-0.10-0.11}$
peripheral 30-80%	$2.71^{+0.11+0.13}_{-0.11-0.12}$	$2.59^{+0.13+0.26}_{-0.13-0.25}$	$2.22^{+0.12+0.12}_{-0.12-0.13}$

Table 3.2: Extracted source size of proton-proton, antiproton-antiproton, and proton-antiproton systems in Au+Au collisions at top RHIC energy in STAR for central, mid-central and peripheral data sets. Reported errors are statistical (first) and systematic (second)[43].

Extensive study of the effect of residual correlations in baryon-baryon system has been recently done in case of (anti)proton-(anti)proton correlation functions measured in Au+Au collisions at $\sqrt{s_{NN}} = 200GeV$ (see figure 3.7). Plots show functions calculated for central events 0-10% (red) as well as for mid-central 10-30% (green) and peripheral 30-80% (blue). Top panel represents proton-proton functions, middle panel shows anti-proton-anti-proton functions and bottom panel shows proton-anti-proton data. Presented functions are corrected on purity, momentum resolution and residual correlations. In residual correlations correction influence of proton-lambda was taken into account. It was found that residual correlations do not have significant influence on proton-proton function but in case of unlike sign system of proton-anti-proton residual correlations play dominant role. Table 3.2 show source sizes for different proton combinations and various centrality bins for Au+Au collisions at $\sqrt{s_{NN}} = 200GeV$. Calculated values of source sizes show clear centrality dependence and consistency between various proton-(anti)proton combinations what was achieved thanks to applied corrections: purity correction, momentum resolution correction and residual correlations correction.

3.3 Overview of previous attempts to analysis of pion-proton femtoscopy

Probably the first attempt to analyze pion-proton correlations was done in the A877 experiment at the AGS facility. Measurement was done for central (4% of the geometrical cross section) collisions of Au+Au collisions. Figure 3.8 presents results of this analysis. Upper panel show $\pi^- - p$ correlation functions, lower panels show $\pi^+ - p$ correlation functions. Experimental functions are plotted with black points. Solid, dashed and dotted lines show theoretical calcu-

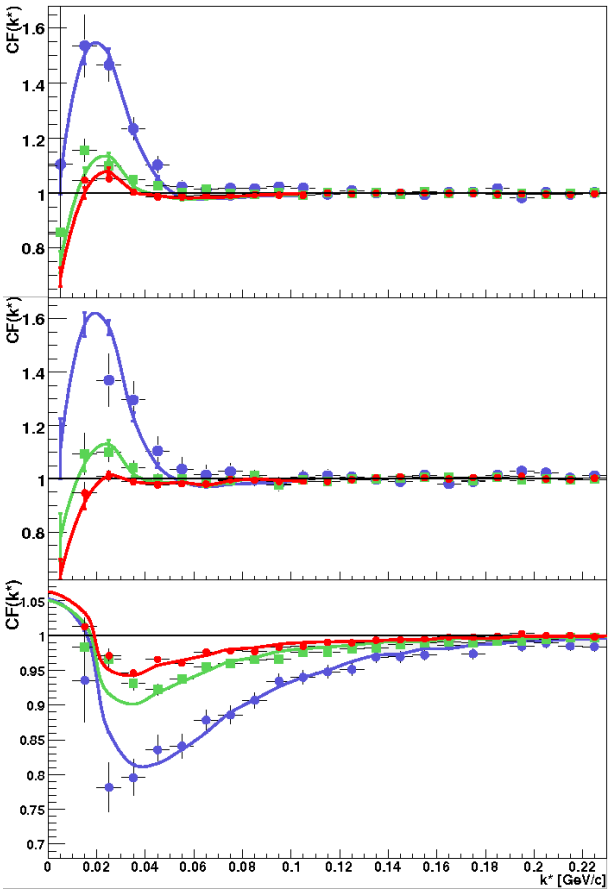

Figure 3.7: Results of proton femtoscopy corrected on momentum resolution, purity and residual correlations. Top panel proton-proton functions, middle panel anti-proton-anti-proton and bottom panel proton-anti-proton functions. Red points (lines) are for central data 0-10%, green for mid-central 10-30% and blue for peripheral 30-80% [43].

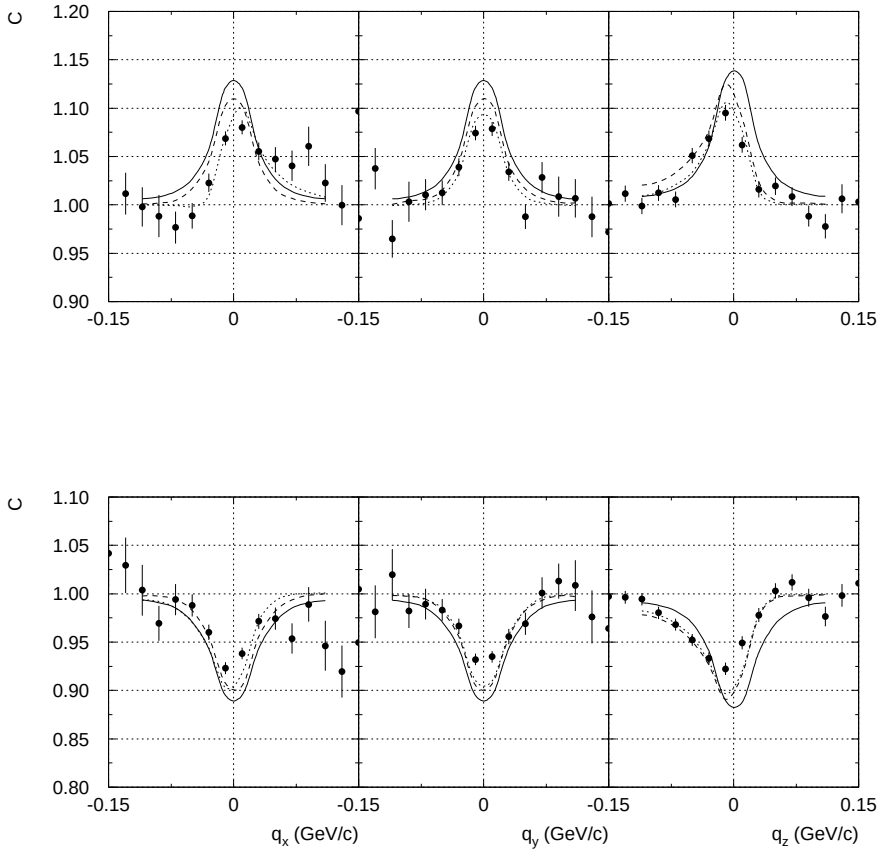

Figure 3.8: $\pi^- - p$ correlation functions (upper plots) and $\pi^+ - p$ (lower plots) measured in the E877 experiment in Au+Au collisions at $\sqrt{s_{NN}}$ =11GeV [44]. Points - experimental functions, solid, dashed and dotted lines - theoretical calculations.

lations for system with no asymmetry, system with asymmetry in z direction $\Delta z = 10$[fm] and for system with asymmetry in x and z directions $\Delta x = 5$[fm] and $\Delta z = 10$[fm]. Δx or Δz is a distance between average emission points of poins and average emission points of protons in *x* and *z* axis respectively. According to the author the best agreement with the data is for system with asymmetry 10[fm] in *z* and 5[fm] in *x*.

An attempt to study pion-proton femtoscopy was also done in the fixed target experiment by the NA49 collaboration. Left panel of figure 3.9 shows $\pi^+ - p$ experimental correlation function (pink points) compared to RQMD study (blue lines) and right panel of this figure presents preliminary results of double ratios of *out* pion-proton correlation functions calculated for $\pi^+ - p$ (red points) and $\pi^- - p$ (blue points) systems in central Pb+Pb collisions at $\sqrt{s_{NN}} =$

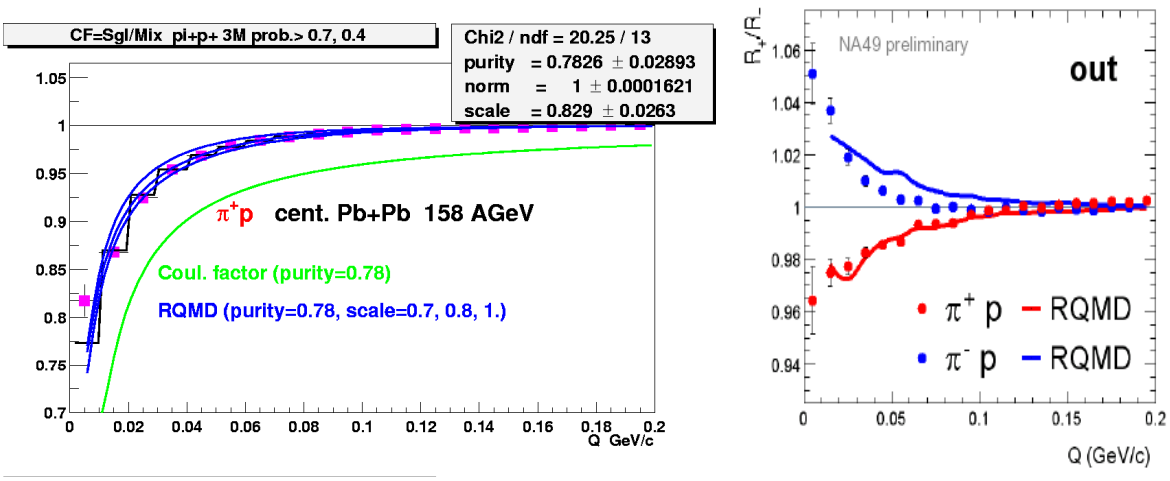

Figure 3.9: $\pi^+ p$ correlation function (left panel) and double ratios of $\pi^+ - p$ (red) and $\pi^- - p$ (blue) experimental correlation functions (right panel). Calculation done for central Pb+Pb collisions at $\sqrt{s_{NN}}$ =158GeV from NA49 experiment (points) compared to RQMD calculations (lines) [45][46].

158[GeV]. Experimental results are compared to RQMD studies (red line for $\pi^+ - p$ and blue line for $\pi^- - p$). Deflection from zero at small values of vector Q suggest that that pions and protons are not emitted from the same regions of the source created in nuclear collision. Fit indicate that RQMD overestimates the r^*-separations by 10-20%. According to the authors overestimation of the observed asymmetry is the result of underestimation of the collective flow in the model.

3.4 Summary

Femtoscopic measurements of various systems done at RHIC by STAR and Phenix experiments in Au+Au collisions at $\sqrt{s_{NN}} = 200GeV$ are summarized at figure 3.10 which presents source size R_{inv} versus transverse mass m_T. Data show negative correlation between calculated source size and transverse mass which is universal for all particle species. Observed decrease of the size with increasing m_T is connected with the collective behavior of the created system. Measured sizes varies from about $R_{int} = 7\,fm$ for pion-pion source at $m_T = 0.2GeV/c^2$ up to about $R_{int} = 1.5\,fm$ for proton-lambda.

A few attempts to study pion-proton correlations in heavy ion collisions was done in the past. Their results suggest space-time asymmetry of the pion-proton source. However they were only

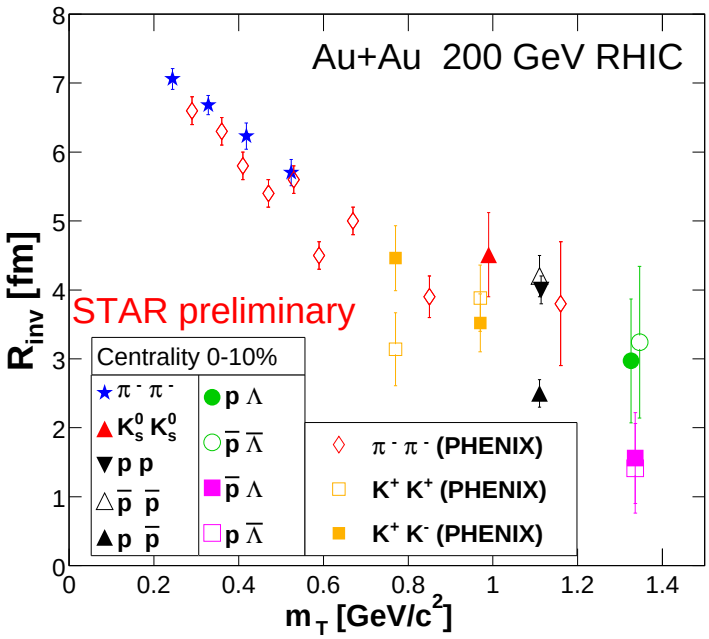

Figure 3.10: Source size R_{inv} versus transverse mass m_T for various systems in Au+Au collisions at $\sqrt{s_{NN}} = 200GeV$ measured by STAR and Phenix experiments [42].

presented in preliminary versions. This thesis is intended to provide the most extensive and the most advanced study of pion-proton correlations.

Chapter 4

Experimental Setup

4.1 RHIC - Relativistic Heavy Ion Collider

Relativistic Heavy Ion Collider RHIC [47][48] situated in Brookhaven National Laboratory in USA began its operation in the summer 2000. RHIC is the first heavy ion collider. It is constructed in 3.834 km long ring tunnel. The collider consists of two accelerator rings with six intersection points. Heavy ion (up to Au) beams can be accelerated up to 100 GeV/nucleon. Proton beams can be accelerated up to 250 GeV.

Heavy ion beams are generated in pulsed sputter ion source at the Tandem Van de Graaff and accelerated up to 1MeV/nucleon. At the exit they are partially stripped of their electrons (up to charge +32 for Au). Positively charged ions are delivered to Booster Synchrotron where are accelerated up to 95MeV/nucleon. Before injection to AGS Alternating Gradient Synchrotron ions are stripped again (up to charge +77 for Au). AGS accelerates ions up to RHIC injection energy which is 10.8GeV/nucleon. Before final injection to RHIC ions are finally stripped of all electrons. RHIC complex overview as well as acceleration scenario is depicted on figure 4.1.

RHIC began its operation with four experiments STAR, PHENIX, PHOBOS and BRAHMS which are briefly described below [49].

PHENIX The Pioneering High Energy Nuclear Interaction eXperiment [50][51] is designed to measure direct probes of the collisions such as electrons, muons, and photons. This detector consists of four instrumented spectrometers or arms and three global detectors. Electrons, photons and charged hadrons are detected by east and west central arms centered at zero rapidity region. East and west central arms cover $2 \times 90^\circ$ of azimuthal angle. North and south forward

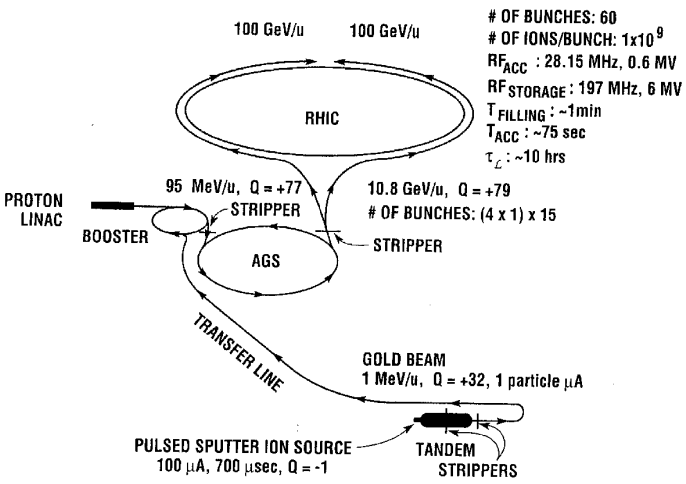

Figure 4.1: RHIC complex overview and acceleration scenario [47]

arms have full azimuthal coverage and are dedicated for detecting muons. The global detectors are to measure vertex position, multiplicity or start time of the interaction.

PHOBOS The PHOBOS experiment [52][53] was designed to measure multiplicities of charged particles and collective flow characteristics within wide pseudo-rapidity region $-5.4 < \eta < 5.4$. It consists of four subsystems: two arm magnetic spectrometer with time-of-flight wall as its central detector, multiplicity array, vertex detector and set of triggers. The layout of the PHOBOS detector is presented at figure 4.3.

BRAHMS Broad RAnge Hadron Magnetic Spectrometers Experiment at RHIC [54][55] is designed to do hadron spectroscopy in wide polar angle relative to beam direction with precise particle identification and momentum determination. Due to wide range of momentum of reconstructed particles Brahms consists of two spectrometers. One for low from a few hundred MeV/c and medium momenta, second for high momenta up to 25-30 GeV/c. Rapidity coverage of this detector is from 0 up to 4. The schematic experimental setup is presented at figure 4.4.

pp2pp In fall 2001 the fifth experiment known as a pp2pp [56] began its operation. Its purpose was to study long range nuclear interactions in collisions of polarize and unpolarized protons of interest to nuclear and particle physicists, and to provide a precise measurement necessary for the analysis of the four other experiment's heavy ion data. Pp2pp by measuring elastic scattering of polarized protons in nonperturbative has a unique opportunity to probe the spin

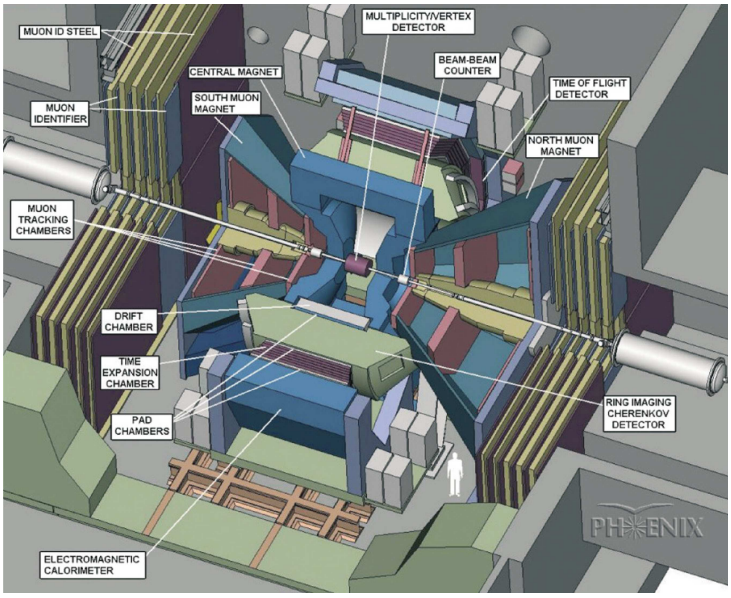

Figure 4.2: Phenix experiment [53]

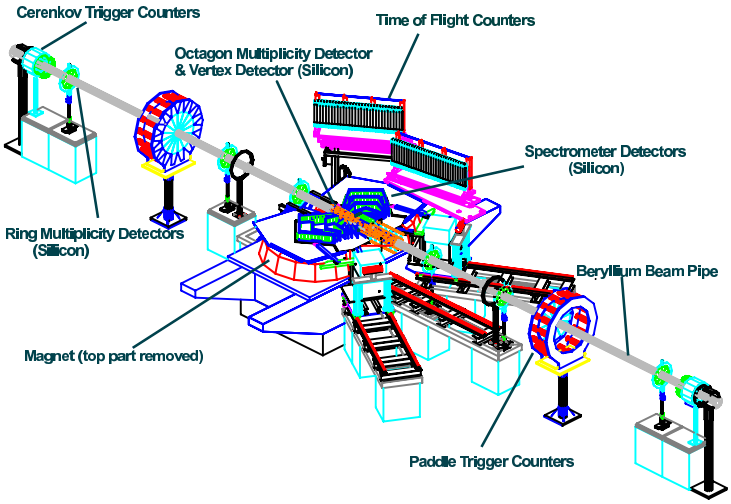

Figure 4.3: Phobos experiment [53]

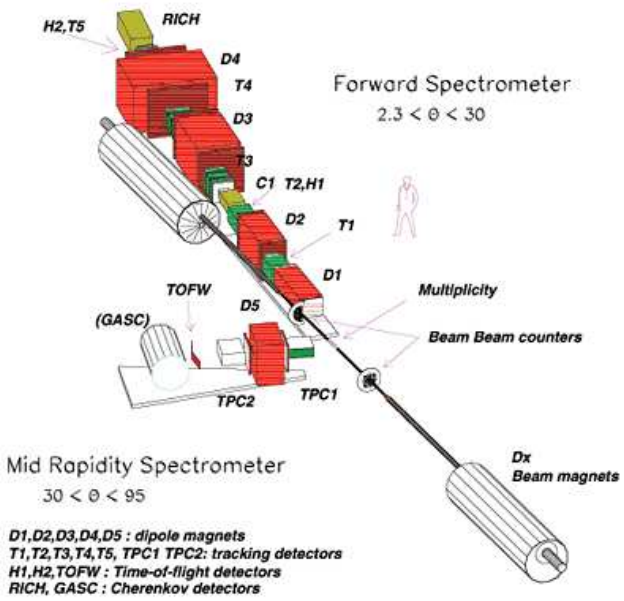

Figure 4.4: Brahms experiment [55]

structure of the proton and a pomerons - the proposed carriers of the strong force. The layout of this experiment is presented at figure 4.5.

Since run 9 the pp2pp detectors are installed in the STAR experiment. The idea is to investigate, using pp2pp Roman Pots detectors together with STAR TPC and ToF, elastic scattering and its spin dependence, the structure of color singlet exchange in the non-perturbative regime of QCD, search for diffractive production of light and massive systems in double Pomeron exchange process and search for new physics, including glueballs and Odderon [58].

4.2 STAR experiment

STAR - Solenoidal Tracker At RHIC is the largest experiment at RHIC [59][60]. STAR has been dedicated to investigate the behavior and properties of strongly interacting matter at high energy density and its primary goal is to search for signatures of quark gluon plasma formation. Its design is based on time projection chamber placed together with other sub-detectors inside a solenoidal magnet [61] which produces a uniform magnetic field in a range $0.25 < |B_z| = 0.5T$. Such design allows simultaneous measurement of various observables.

STAR Time Projection Chamber is the main tracking device of the STAR detector [62]. TPC identifies particles based on ionization energy loss (dE/dx). It is capable to record the

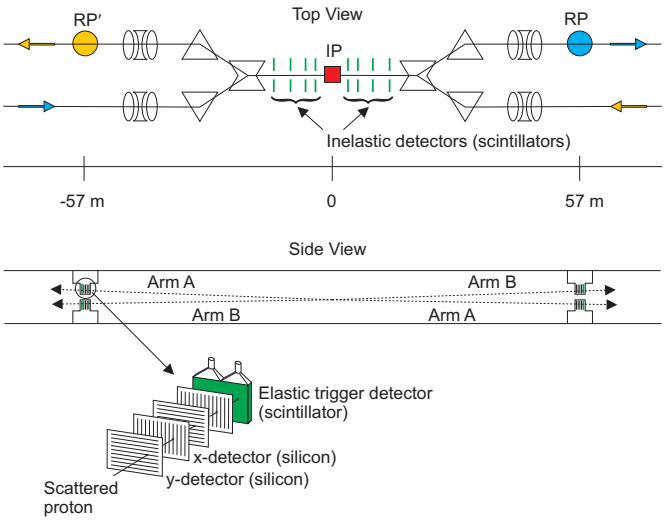

Figure 4.5: pp2pp experiment [57]

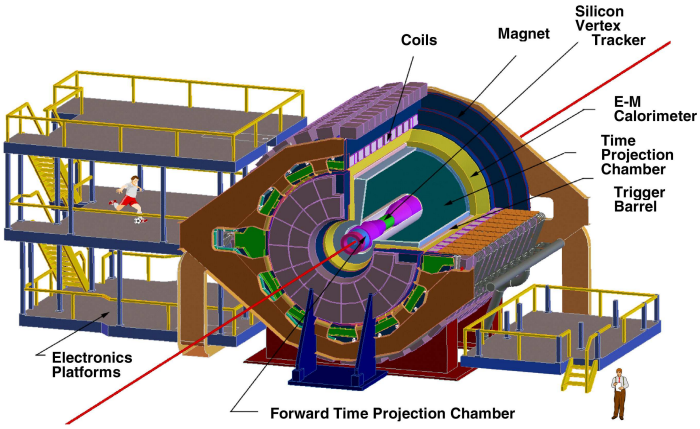

Figure 4.6: STAR experiment [60]

tracks of the particles and measure their momenta. It surrounds the vertex of the collision in full azimuthal angle and pseudo-rapidity region from -1.8 up to 1.8.

The schematic layout of the TPC is shown at figure 4.7. It is situated $\pm 2.1m$ from the vertex along the beam line. The inner diameter is $1m$ and the outer is $4m$. The cathode situated at $z = 0$ operates at $28kV$ and with two anodes placed at $\pm 2.1m$ gives electric field equal $135V/cm$. Each anode has 12 sectors (readout modules). On the outer radius subsectors the pads are $20mm$ long. On the inner radius subsectors single pad length is $12mm$ which improves two track resolution especially for low-pt tracks which cross the TPC pads at angles far from perpendicular.

Charged particle ionizes TPC gas while it passes through the TPC. Energy lost on ionization is transfered to liberated electrons which are registered in the readout modules. The dE/dx is measured in up to 45 padrows. The length of the single padrow is too short to accurately measure average dE/dx thus the most probable energy loss is measured. The mean value of dE/dx is determined from the 70% truncated mean (30% of the clusters having the largest signal are removed). Ionization spectra from the STAR TPC detector are parametrized by "Bichsel functions" [62][63][64][65][66] which in case of thin layers gives much better approximation of energy loss than Bethe-Bloch parametrization.

In TPC momenta of the particles can be determined from $0.1GeV$ up to about $30GeV$ but particles can be correctly identified from $0.1GeV$ up to above $1GeV$. This makes analysis presented in this thesis difficult as the requirements for proton selection exceeds the upper limit for momenta of the particles.

The position resolution along the *z*-axis is the best for short drift distances and small deep angles and varies from $0.5mm$ up to $3.5mm$. Resolution in transverse plane (along the pad rows) varies from $0.5mm$ (for small crossing angle) up to $2mm$ for Full Field ($0.5T$) or from $0.5mm$ up to $3mm$ for Half Field ($0.25T$).

TPC is filled with the P10 gas which contains 90% of argon and 10% of methane. P10 gas has a fast drift velocity (about $5.45cm/\mu s$) which peaks at relatively small electric field. The drift velocity is known with a precision of 0.1%. Oxygen and water absorbs drifting electrons. To assure high purity of TPC gas, necessary for good quality of particle reconstruction, gas is circulating over the system where oxygen and water contamination is eliminated.

STAR Silicon Vertex Tracker SVT[67] was designed mainly to improve vertex position reconstruction, two track separation resolution and the energy loss measurement. Construction of

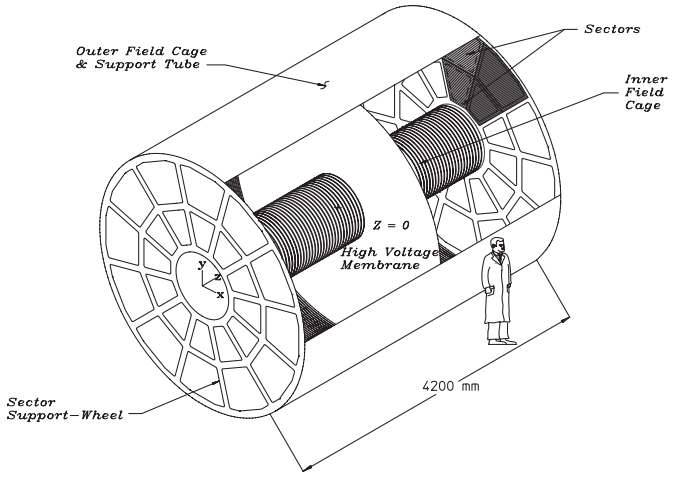

Figure 4.7: STAR Time Projection Chamber [62].

SVT is based on silicon drift detector SDD technology which gives two-dimensional position measurement with resolution of $20\mu m$. 216 SSDs are arranged in three barrels around the beam pipe. Inner 6.9cm in radius and 25.2cm length, middle 10.8cm radius and 37.8cm length and outer 14.5 radius and 44.4cm length.

Very big disadvantage of SVT is the number of gamma conversions into electron-positron pairs which take place in the material of this detector. Such pairs are correlated what in case of misidentification may have significant impact on analysis of non-identical correlation functions.

STAR Triggers The STAR trigger system operates at RHIC crossing rate about 10MHz [68]. For Au+Au collisions in run4 it was based on fast detectors CTB - Central Trigger Barrel, two west and east ZDCs - Zero Degree Calorimeters, BBC - Beam-Beam Counter. Information from the fast detectors is used to trigger slow detectors like TPC or SVT which can operate at about 100Hz. CTB measured charged particles multiplicity in pseudo-rapidity range $-1 < \eta < 1$. ZDC verified centrality of the AuAu collision and z-vertex position in minimum-bias collisions, BBC was for z-vertex determination in AuAu central collisions.

Chapter 5

Experimental analysis technique and results

5.1 Events selection

In the experiment the impact parameter of two colliding nuclei cannot be measured directly thus centrality of the collision is estimated from the multiplicity of the charged hadrons in the event. In this work collisions of gold-gold nuclei at the energy in central mass system of 200GeV/nucleon are analyzed. Analysis is done in three different centrality bins: 0-10%, 10-30% and 30-50% of the total hadronic cross section. Such defined centrality bins for analyzed dataset are described by reference multiplicity in the STAR detector. Values of reference multiplicity for selected centrality bins for Au+Au collisions at $\sqrt{s_{NN}} = 200GeV$ taken by STAR in 2004 are presented in table 5.1.

Distribution of reference multiplicity of selected events is presented on figure 5.1. Left panel

Centrality	Reference multiplicity
0-10%	$>= 440$
10-30%	222 - 439
30-50%	96 - 221

Table 5.1: Reference multiplicity for centrality bins used in this work for STAR 2004 data, Au+Au collisions at $\sqrt{s_{NN}} = 200GeV$.

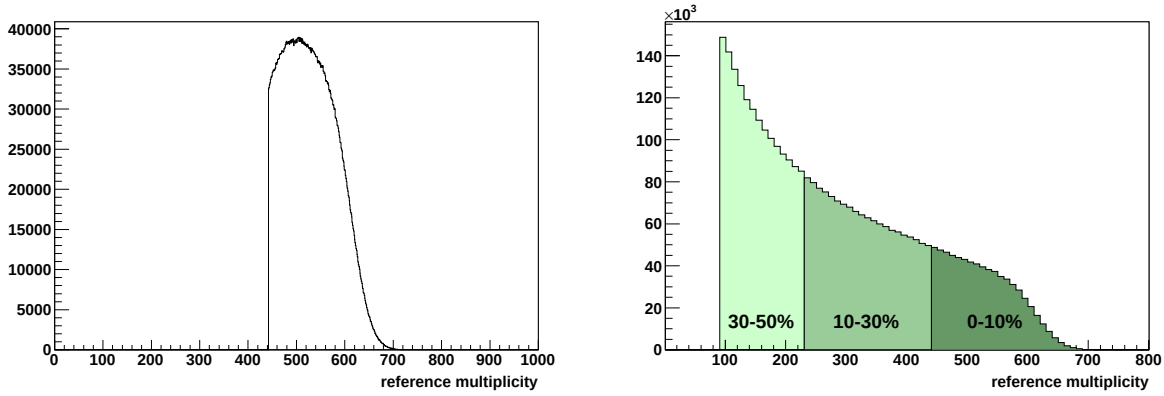

Figure 5.1: Reference multiplicity distributions for STAR 2004 data, Au+Au collisions at $\sqrt{s_{NN}} = 200GeV$ used in this work. Left panel: events from central trigger. Right panel: events from minimum bias trigger.

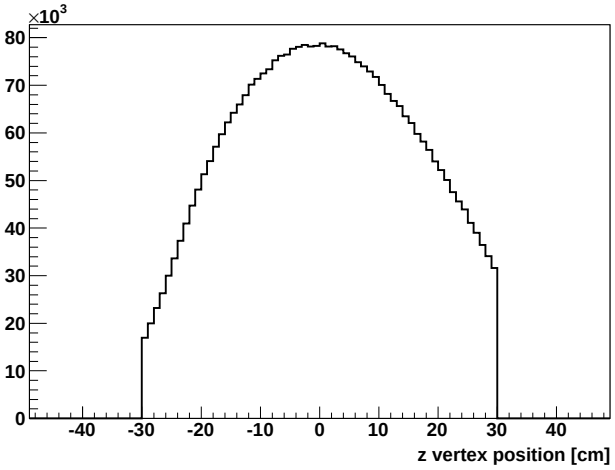

Figure 5.2: Z-vertex position distribution for STAR 2004 data, Au+Au collisions at $\sqrt{s_{NN}} = 200GeV$.

shows distribution of the events taken with the central trigger. Right panel shows distribution of the events recorded with the minimum-bias trigger setup.

Precision of the reconstructed tracks is very significant so only events that took place in the center of the detector (with z-vertex position $-30cm < z < 30cm$) are analyzed. Figure 5.2 presents distribution of z-vertex position of selected events.

5.2 Particle selection

Particle identification is based on ionization energy loss (dE/dx) in TPC. Pions and protons are selected based on N_σ value which describes distance (in standard deviation units) from the mean of the Gaussian parametrization of the dE/dx curve. For pions and protons N_σ has been set to 3 which corresponds to 99.7% of the total integral.

Measuring correlations of non-identical particles with different masses requires wide acceptance on particle identification. In case of pion-proton analysis which have significantly different masses particles identification faces problems not known in other analyses. To construct pair with small relative velocity of the particles pion with momentum $p = 0.1 GeV/c$ needs proton with $p = 0.67 GeV/c$, proton with momentum $p = 1.2 GeV/c$ has a close velocity pion with $p = 0.18 GeV/c$. This shows that analysis presented in this work reaches the limits of particle identification in TPC. The second significant problem with particle identification that cannot be avoided in this analysis is that pions and protons which creates close velocity pairs are selected from the regions of dE/dx plot where lines of pions and protons intersect the line of electrons. This problem significantly increases danger of electron contamination. Figure 5.3 shows dE/dx measurement versus magnetic rigidity. Solid lines are $I70$ means Bichsel's [62] prediction for 30% truncated dE/dx mean in STAR TPC.

Summary of the particle track cuts is presented in table 5.2. Presented single track cut values are valid for all investigated centrality bins. Only particles with number of hits equal or grater than 15 are taken into account. The distance of closest approach *DCA* to the primary vertex should be smaller than $3cm$.

Histograms presented on figure 5.4 show transverse momentum distributions versus rapidity of pions and protons for separate k^* bins of measured correlation function. Presented first 6 bins cover region of the measured correlation effect. These histograms show that most of the protons in the correlation effect have transverse momentum higher than 1[GeV/c] and most of the pions which contribute to measured correlation function have transverse momentum between 0.15 and 0.2[GeV/c]. It was mentioned in section 4.2 that STAR Time Projection Chamber - the main detector used in this analysis - can correctly identify particles with momentum up to $p \approx$ 1[GeV/c]. This is additional difficulty that makes analysis of pion-proton momentum correlation functions very complicated.

Significant improvement of particle identification and selection can be achieved with additional signal from Time-Of-Flight detector which has been recently installed in the STAR

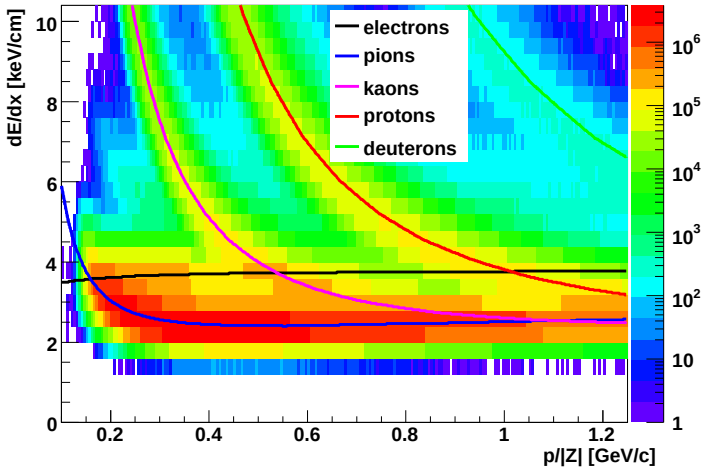

Figure 5.3: Rate of energy loss versus magnetic rigidity in STAR.

	pion	proton
$N_{\sigma\pi}$	-3.0 - 3.0	3.0 - 1000
$N_{\sigma K}$	-1000 - -3.0	3.0 - 1000
$N_{\sigma p}$	-1000 - -3.0	-3.0 - 3.0
y	-0.7 - 0.7	-0.7 - 0.7
p [GeV/c]	0.1 - 0.6	0.4 - 1.25
p_T [GeV/c]	0.1 - 0.6	0.4 - 1.25
N_{hits}	$>= 15$	$>= 15$
$DCA[cm]$	$<= 3$	$<= 3$

Table 5.2: Summary of single track cuts for pions and protons.

experiment. Data taken with TOF detector from Au+Au collisions at $\sqrt{s_{NN}} = 200$[GeV] from Run 2010 will be available in the near future.

5.3 Pair selection

Track splitting takes place when one track is reconstructed as two separate trucks. This effect causes false enhancement of number of pairs in the lowest k^* bins. In order to remove pairs constructed of split tracks, a pair level cut was developed in STAR [69]. The idea is based on hits location of each truck. Figure 5.5 shows four scenarios. The first one where tracks are clearly two tracks, second scenario where the splitting is the most probable, and cases (b) and (c) where there is some chance that splitting took place.

This effect plays significant role in case of particles with similar masses. In case of this analysis such scenario is very rare.

Track merging takes place when two particles travel through the detector so close that their hits are reconstructed as a one track what results in reduced number of pairs in low k^* bins.

Two tracks are considered as a merged if they share more than 10% of the hits. Minimum separation between two hits of different tracks should be 5mm. If separation between two hits of two different tracks is lower than 5mm such hits are considered as shared. Pair of tracks which shares more than 10% of the hits (1 to 5 hits) is removed from the analysis. Influence of merged hits of tracks of pair pion-proton pairs on correlation function is presented on figure 5.6.

Electron-positron contamination Gamma quants which comes from electromagnetic decays of resonances may convert into electron-positron pairs while traveling through the material of the detector. Such scenario was very often in the silicone barrels of SVT detector. Momenta of electron-positron pairs which comes from gamma quant conversion are correlated hence if misidentified as pion-proton pair introduce a fake correlation effect.

To eliminate such pairs a topological cut was developed in STAR. The idea of $e^+ - e^-$ pairs finding is shown on figure 5.7. Parameters that are taken into account in this cut are as follows. Delta deep angle $\Delta\theta$ which for gamma conversion into $e^+ - e^-$ pair has relatively small value. Invariant mass m_{inv} which for γ decay products should be close to zero. Distance between two helices in longitudinal direction ΔZ and in transverse plain ΔXY as well as decay length ΔL and

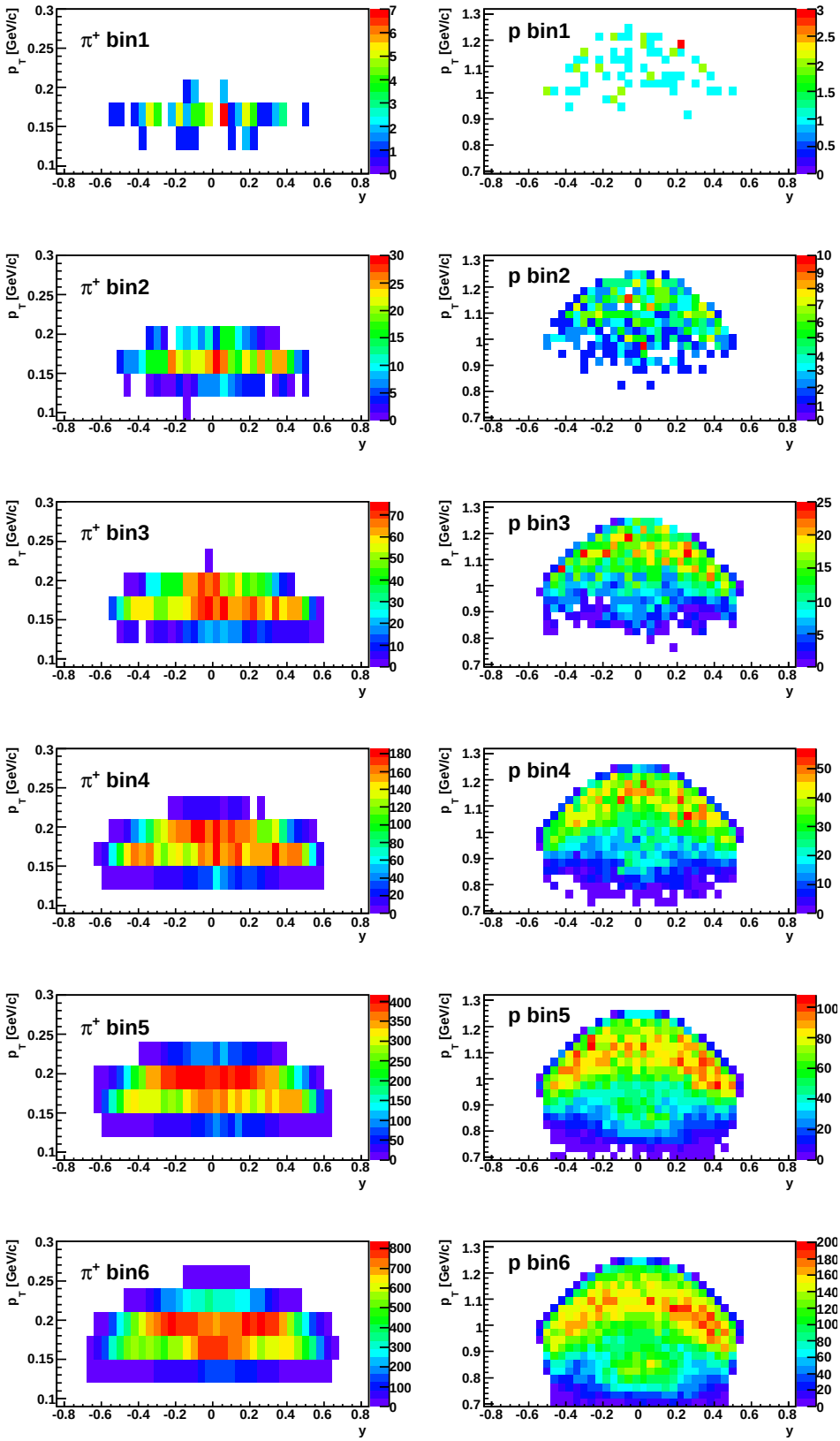

Figure 5.4: Example of distribution of p_T vs. y for pions and protons in separate first six k^* bins of the $\pi^+ - p$ correlation function - STAR data, Au+Au central collisions at $\sqrt{s_{NN}} = 200$[GeV].

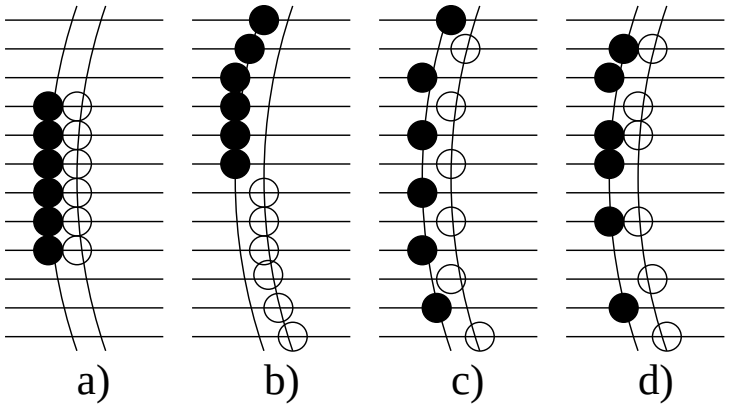

Figure 5.5: Various scenarios of distribution of hits of tracks [69].

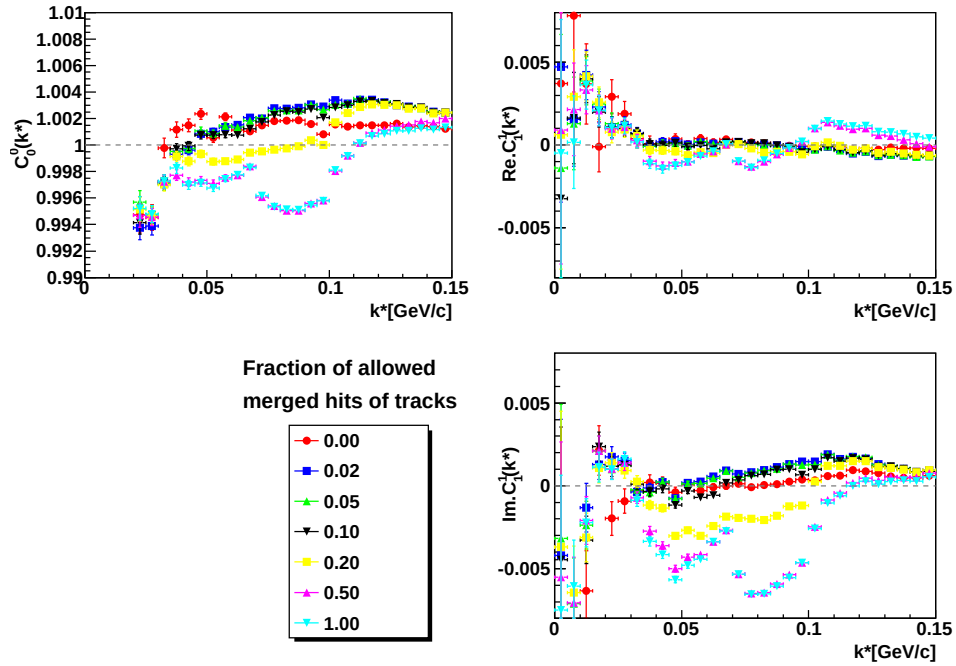

Figure 5.6: Influence of merged hits of tracks of pion-proton pairs on correlation function.

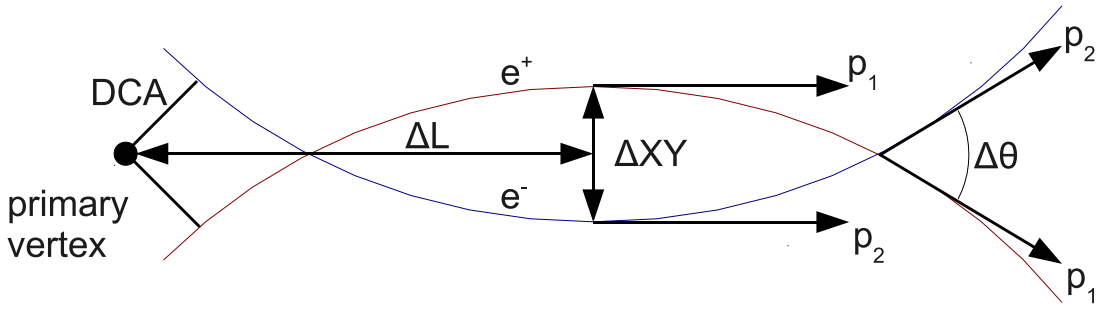

Figure 5.7: Topological method of electron-positron pairs removal (transverse plain view).

Parameter	Value
$\Delta\theta$	<0.07
m_{inv}	< 0.07 GeV/c
ΔZ	< 2 cm
ΔXY	< 3 cm
ΔL	> 3 cm
PID_{ee}	0.01

Table 5.3: Values for the electron-positron pairs removal.

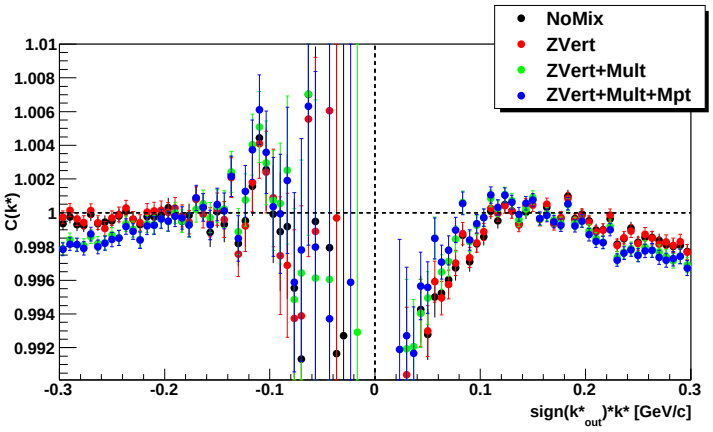

Figure 5.8: Comparison of different mixing methods in constructing $\pi^+ - p$ correlation function.

PID probability of being electron-positron pair. Values of the parameters used in the analysis can be found in the table 5.3.

5.3.1 Events mixing

Background should be constructed only from the events with similar characteristics thus events are divided into bins with respect to the z-vertex position, event multiplicity and mean transverse momentum of all the particles in the event. Z-vertex position is divided into 15 bins which gives 4cm width of a single bin. Multiplicity of every centrality bin is divided into 6 bins and mean p_T into 3 bins. Such definition gives 270 total mixing bins.

It is very important in constructing correlation function to correctly add functions constructed in different mixing bins. Thus method of rescaling denominator (equation 5.1) should

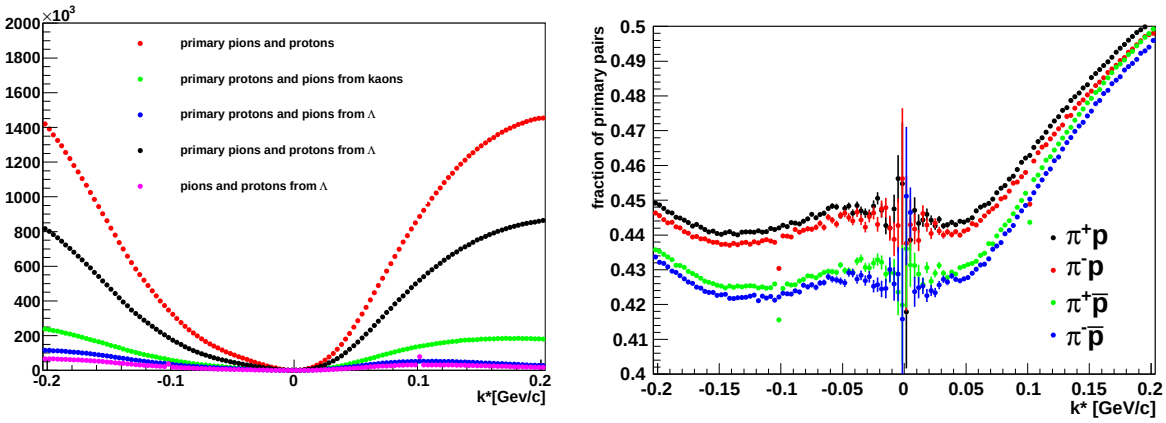

Figure 5.9: Contribution of different particles to $\pi^+ p$ pair (left) and fraction of primary pion-proton pairs for all charge combinations (right) - Therminator results.

be used rather than scaling correlation function (equation 5.2).

$$C(k^*) = \frac{\sum_i N_i(k^*)}{\sum_i c_i D_i(k^*)} \tag{5.1}$$

$$C(k^*) = c\frac{\sum_i N_i(k^*)}{\sum_i D_i(k^*)} \tag{5.2}$$

Figure 5.8 shows comparison of different mixing methods in constructing correlation function. In every case function was normalized by rescaling denominator. The best results are achieved for mixing in 3 variables: vertex position, multiplicity of the event and mean p_T of the particles in the event.

5.4 Purity correction

Particle identification in the STAR experiment is based on probability. Additionally although we do our best to construct correlation function only from primary particles which contribute to the correlation effect due to experimental limitations some particles coming from weak decays are also taken to the analysis (as primary particles we also consider particles coming from short lived strong decaying resonances). These two effects are taken into account in the purity correction.

Probability of correct particle identification P_{PID} was estimated in the experiment based on `HIJING` simulations. Probability of being primary particle has been estimated in simulations with `THERMINATOR`.

Contribution from different particles is presented on figure 5.9 (left panel). Right panel of this figure shows calculated fraction of primary pion-(anti)proton pairs. Pion-proton correla-

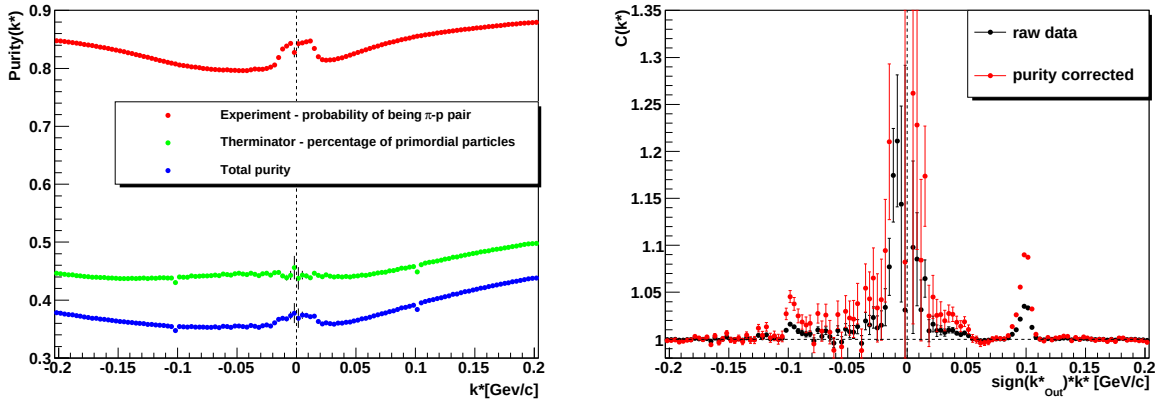

Figure 5.10: Left panel: example of experimental probability of being pion-antiproton pair (red), theoretical percentage of primary pairs (green) and total purity correlation function (blue). Right panel: example of impact of purity correction on experimental correlation function. Raw data $\pi^+ - \bar{p}$ correlation function (black) and purity corrected $\pi^+ - \bar{p}$ correlation function (red).

tion function is mainly affected by products of the decays of kaons and lambdas. The most significant is influence of protons coming from lambdas and pions coming from kaons decays. Decay products of sigma (Σ) and other particles that decay into pions or protons have negligible contribution into the purity function of pion-proton pair.

Right panel of figure 5.9 shows that percentage of primary pairs is higher for particles than for anti-particles.

Purity function is a product of PID probabilities and fraction of primary pairs F_{prim}.

$$C_{purity}(k^*) = P_{1PID}(p_{T1})P_{2PID}(p_{T2})F_{prim}(k^*) \tag{5.3}$$

Measured correlation function can be corrected according to the formula:

$$C(k^*) = \frac{C_{exp}(k^*) - 1}{C_{purity}(k^*)} + 1 \tag{5.4}$$

Figure 5.10 shows purity function $C_{purity}(k^*)$ (left panel) and impact of purity correction on measured correlation function (right panel). Purity increases strength of correlation effect but do not changes its k^* range or direction. Flat tails (large k^* above 0.1GeV) of the correlation function are not affected by purity correction.

If the correlation function is expressed in spherical harmonics then purity function C_{purity} also should be expressed in spherical harmonics. Corrected function is calculated in the same way as the experimental one (see section 2.4). In such case function which is intended to be corrected is treated as numerator and purity function is treated as denominator.

5.5 Momentum resolution correction

Reconstructed momentum of the particle differs from the real momentum due to the effect of the momentum resolution. This effect affects correlation function what is calculated with respect to the relative momentum of two particles. This leads to underestimation of the extracted source size due to lower number of pairs at small k^*.

Momentum resolution correction can be applied either to the calculated correlation function or to the fit procedure. In this work momentum resolution at the level of fit procedure is used.

Three components of reconstructed momentum p are:

$$p_x = p\sin(\theta)\cos(\phi) \tag{5.5}$$

$$p_y = p\sin(\theta)\sin(\phi) \tag{5.6}$$

$$p_z = p\cos(\theta) \tag{5.7}$$

systematic momentum shift due to energy loss:

$$\langle p_{true} - p \rangle = a + bp^{\alpha} \tag{5.8}$$

momentum resolution (Gaussian smearing)

$$\frac{\Delta p}{p} = a_p + b_p p^{\alpha} + c_p p \tag{5.9}$$

$$\Delta\phi = a_\phi + b_\phi \phi^{\alpha} \tag{5.10}$$

$$\Delta\theta = a_\theta + b_\theta \theta^{\alpha} \tag{5.11}$$

parameters a, b, c are particle type dependent. For each p, ϕ and θ corresponding corrections ∂p, $\partial\phi$ and $\partial\theta$ are generated from Gaussian distribution. Then three components of the reconstructed momentum can be corrected.

$$p_x^{smeared} = p_x^{real} + \partial p_x \tag{5.12}$$

$$p_y^{smeared} = p_y^{real} + \partial p_y \tag{5.13}$$

$$p_z^{smeared} = p_z^{real} + \partial p_z \tag{5.14}$$

In the fit procedure when momentum resolution is enabled two particle relative momentum k^* is calculated from smeared momenta.

	quark content	decay products	Breit-Wigner mass	Breit-Wigner full width
Δ^{++}	uuu	$\pi^+ + p$	1232 MeV	118 MeV
$\bar{\Delta}^{++}$	$\bar{u}\bar{u}\bar{d}$	$\pi^- + \bar{p}$	1232 MeV	118 MeV
$\bar{\Delta}^{0}$	$\bar{u}\bar{d}\bar{d}$	$\pi^+ + \bar{p}$	1232 MeV	118 MeV
Δ^{0}	udd	$\pi^- + p$	1232 MeV	118 MeV

Table 5.4: Δ baryon summary.

5.6 Fit procedure

Correlation functions of non-identical particles do not have an analytical form. To extract quantitative information from measured functions one has to arbitrarily assume a form of the emission source function and generate a set of correlation functions with different parameters of the emission source function and find which one suites the best the experimental result.
In the fit procedure momenta of the pairs used for construction of the experimental correlation functions are used. For each pair the freeze-out coordinates are generated from the emission source function. Based on freeze-out coordinates, momenta of the pair and types of the particles a squared wave-function, called weight, is calculated. Weight describes Coulomb and strong interaction between particles in the pair. Emission source for which the χ^2 value between generated function and experimental one is the smallest describes the best the experimental source. This procedure is implemented in the CorrFit [70] program which was used for fitting of experimental and theoretical correlation functions in this work.

5.7 Influence of Δ resonance on $\pi - p$ correlation function

Δ resonance is short lived strong decaying resonance thus products of its decay are treated as primary particles but it decays into pion and (anti)proton pair which may significantly impact measured pion-proton correlation function. Δ resonances exist in four various charge combinations which may decay into $\pi^+ - p$, $\pi^+ - \bar{p}$, $\pi^- - p$ or $\pi^- - \bar{p}$ thus Δ may influence all four investigated combinations of pion-proton functions. Table 5.4 summarizes all interesting for this analysis Δ species. To estimate potential impact of Δ on pion-proton correlation function an extensive study using `Therminator` [14] has been performed.

5.7.1 Mass dependent particle decay widths with Breit-Wigner distribution in `Therminator`

`Therminator` is a very powerful tool for studying resonances. In version 1.0 its module `ParticleDecayer` uses fixed mass (mean of the Breit-Wigner) of the resonance in the process of determining decay conditions. To achieve more realistic effect in studying influence of delta resonance on pion-proton function randomizing mass of the resonance according to Breit-Wigner (eq. 5.15) distribution has been implemented into `Therminator v1.0`.

$$F(m) = \frac{\Gamma^2/4}{(m-M_0)^2+\Gamma^2/4} \tag{5.15}$$

M_0 is mean of the distribution and Γ is the full width of the distribution. Inverse transformation method has been used in process of resonance mass generating. Inverse cumulative distribution function for Breit-Wigner distribution is defined by equation 5.16.

$$G(y) = M_0 + \frac{\Gamma}{2}\,\mathrm{tg}\,(\pi(y-0.5)) \tag{5.16}$$

5.7.2 Δ in correlation functions

Figure 5.11 shows $\pi^+ - p$, $\pi^- - \bar{p}$, $\pi^- - p$ and $\pi^+ - \bar{p}$ correlation functions calculated from Therminator data which show Δ^{++}, $\bar{\Delta}^{++}$, Δ^0 and $\bar{\Delta}^0$ resonance at 0.23[GeV/c] respectively. Position of delta resonance is relatively far from the correlation effect which for all combinations of pion-proton functions is up to about 0.1[GeV/c]. Observed peak of the delta resonance is lower for negative values of vector k^* than for positive values of k^*. This is due to difference in number of pairs in combinatoric background.

Figure 5.12 shows centrality dependence of delta resonance in pion-proton correlation functions. Width of the observed delta is constant over all investigated centrality bins. Height of the delta is higher for $30-50\%$ (blue points) and is getting lower for more central events 10-30% (red points) and 0-10% (black points). This effect is also related to difference in number of pairs in combinatoric background.

Two particle distributions of pion-proton pairs plotted on figure 5.13 show no significant impact of products of delta decay on space-time source characteristics. Black points on this figure show results for primary particles, blue points show distributions plotted for primary particles and particles coming from resonances but not from delta resonance and red points show two particle distributions of all particles including delta decay products.

Delta is not observed in correlation functions calculated from experimental STAR data. This can be explained by statistics and momentum resolution issues.

5.8 Influence of Λ baryon on $\pi - p$ correlation function

Baryon Λ decays in weak process into $\pi^- - p$ pair, anti-baryon $\bar{\Lambda}$ decays into $\pi^+ - \bar{p}$ pair. As lambda is long lived particle (mean life time $\tau = (2.631 \pm 0.02) \cdot 10^{-10}$[s][1]) it decays far from primary vertex so a *DCA*-distance of closest approach cuts on single tracks can be applied to remove the products of its decay from the data sample. *DCA* cuts are not sufficient to remove all particles coming from lambda decays though lambda peaks are visible at $k^* \approx 0.1 GeV/c$ in unlike sign functions.

Position of lambda peak in unlike sign functions do not overlap with range of correlation effect so there is no need for special treatment of correlated lambda decay products. However pions and protons coming from lambda which cannot be removed using *DCA* cut decrease purity of the correlation function what results in decreased correlation effect. Especially protons, which extrapolated curvatures point to primary vertex, are very difficult to be removed using *DCA* cuts. This can be taken into account in the purity correction (section 5.4). Contribution of lambda into purity of pion-proton pair is presented on figure 5.9.

Correction on purity have to be applied to all functions not only unlike-sign pairs as proton coming from lambda decay may influence $\pi^- - p$ and $\pi^+ - p$ functions.

5.9 Experimental pion-proton correlation functions - $out - side - long$ decomposition

Application of sophisticated methods described above lead to construction of experimental pion-proton correlation functions which will be presented in this section.

Figures 5.14, 5.15 and 5.16 show correlation functions calculated in *Out*, *Side* and *Long* decomposition as well as corresponding $double - ratios$[2]. All plots show functions for raw data before applying any corrections.

[1] Particle Physics Booklet, July 2008

[2] Functions presented at the 20th International Conference on Ultra-Relativistic Nucleus Nucleus Collisions - Quark Matter 2008 in Jaipur, India.

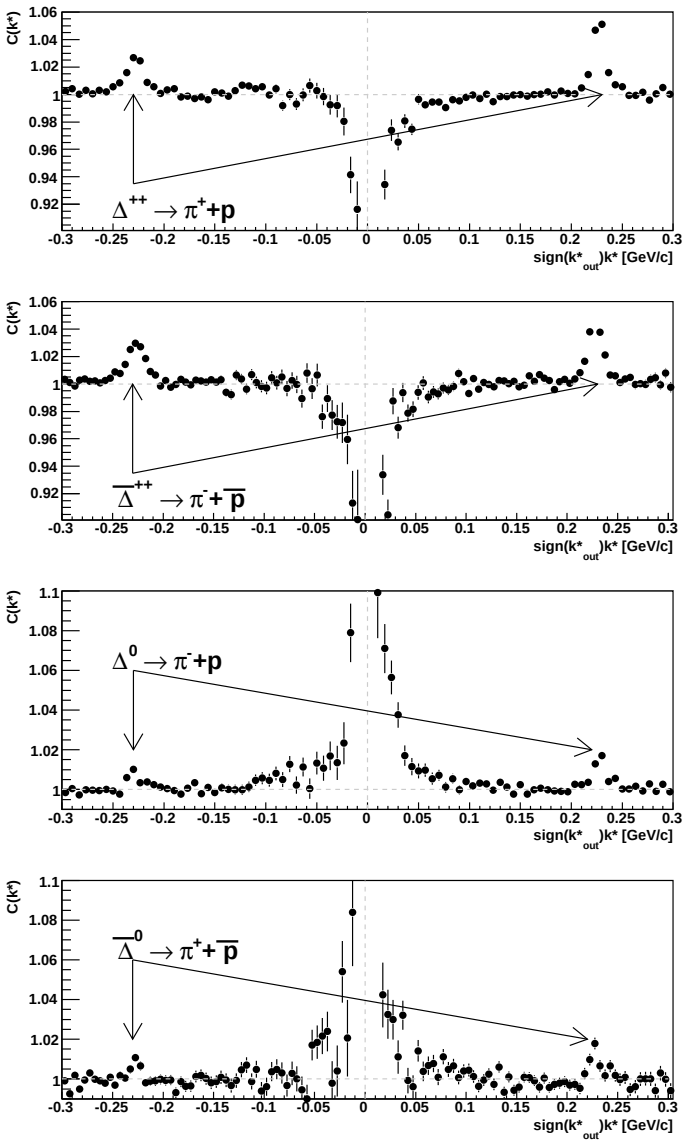

Figure 5.11: Delta resonance in pion-proton correlation function (Therminator results). Functions from top to bottom $\pi^+ - p$, $\pi^- - \bar{p}$, $\pi^- - p$, $\pi^+ - \bar{p}$.

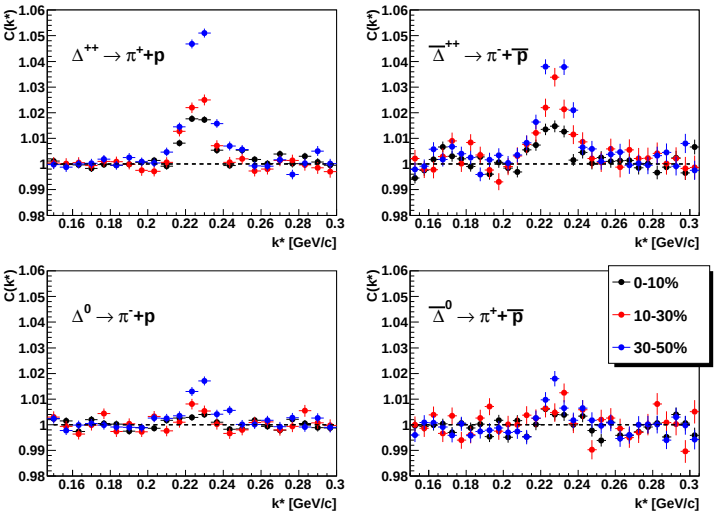

Figure 5.12: Centrality dependence of delta in pion-proton correlation functions (Therminator results). Central data 0-10% - black points, intermediate data 10-30% - red points, mid-central data 30-50% - blue points.

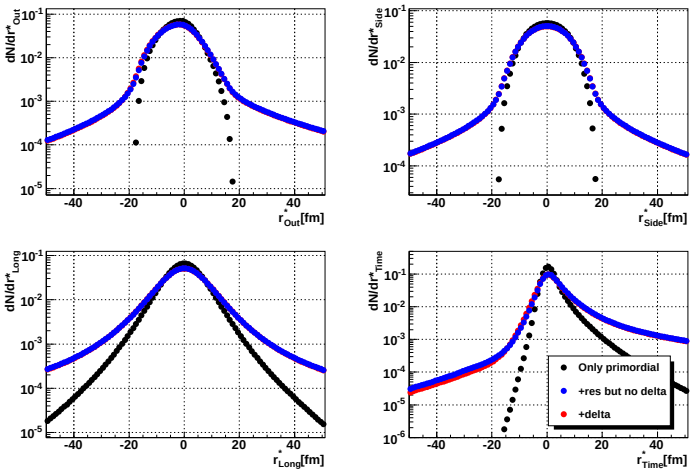

Figure 5.13: Influence of products of Δ^{++} resonance decay into $\pi^{+} - p$ pair on two particle space and time source distributions (Therminator results). Black points - only primary particles, blue points - primary particles and particles from resonances but not from delta resonance, red points - all particles including particles coming from delta resonance.

Physical interpretation of *Out*, *Side* and *Long* components of correlation functions of non-identical particles is described in section 2.2. Functions for $\pi^+ - p$, $\pi^- - \bar{p}$, $\pi^+ - \bar{p}$ and $\pi^- - p$ calculated with respect to the sign of vector k^*_{Out} are presented on left column of figure 5.14. Functions plotted with red dots are for central events (0-10% of total hadronic cross section), green squares are for intermediate events (10-30%) and blue triangles are for mid-central events (30-50%). First two functions reveals attractive Coulomb interaction of like-sign pairs thus observed correlation effect is negative. Expected source size for central collisions is bigger than for intermediate or mid-central collisions what is reflected in strength of the correlation effect - correlation is higher for smaller source size. Next two functions calculated for $\pi^+ - \bar{p}$ and $\pi^- - p$ show positive correlation effect what is in agreement with repulsive coulomb interaction of the unlike-sign pairs. Additional artifact that can be observed on these plots are lambda peaks at $k^* \sim 0.1$[GeV/c]. Lambda peaks do not overlap with observed correlation effect thus they do not need to be taken into account during fit procedure (more detailed explanation of impact of lambda on pion-proton correlation function can be found in section 5.8).

Right column of figure 5.14 present $double-ratios\, C^+/C^-(k^*)$ of corresponding correlation functions. Presented $double-ratios$ reveals differences at low values of k^* between correlation functions calculated for positive or negative sign of the k^*_{Out} vector. Observed deviation from unity for like-sign pairs is negative and deviation for unlike-sign pairs is positive. Such deviation from unity for low values of k^* as explained in section 2.2 is an evidence that average emission points and average emission time of pions and (anti)protons are not the same.

Correlation functions calculated for *side* and *long* components plotted on figures 5.15 and 5.16 can be used as a cross check. As mentioned in section 2.2 due to symmetry in rapidity region *long* components of the correlation functions should be the same thus corresponding $double-ratio$ should be flat over the full range of vector k^*. Definition of the *side* direction and symmetry with respect to the azimuthal angle cause that corresponding *side* $double-ratio$ also should be flat.

Double ratio functions are very sensitive to fluctuations of the correlation functions. Presented $double-ratios$ for all *out*, *side* and *long* components have large error bars. No qualitative information can be extracted due to strong fluctuations of the points at low values of k^*.

One of the reasons why *out, side, long* representation of the pion-proton correlation function is not sufficient for measuring difference between mean space-time emission points is the

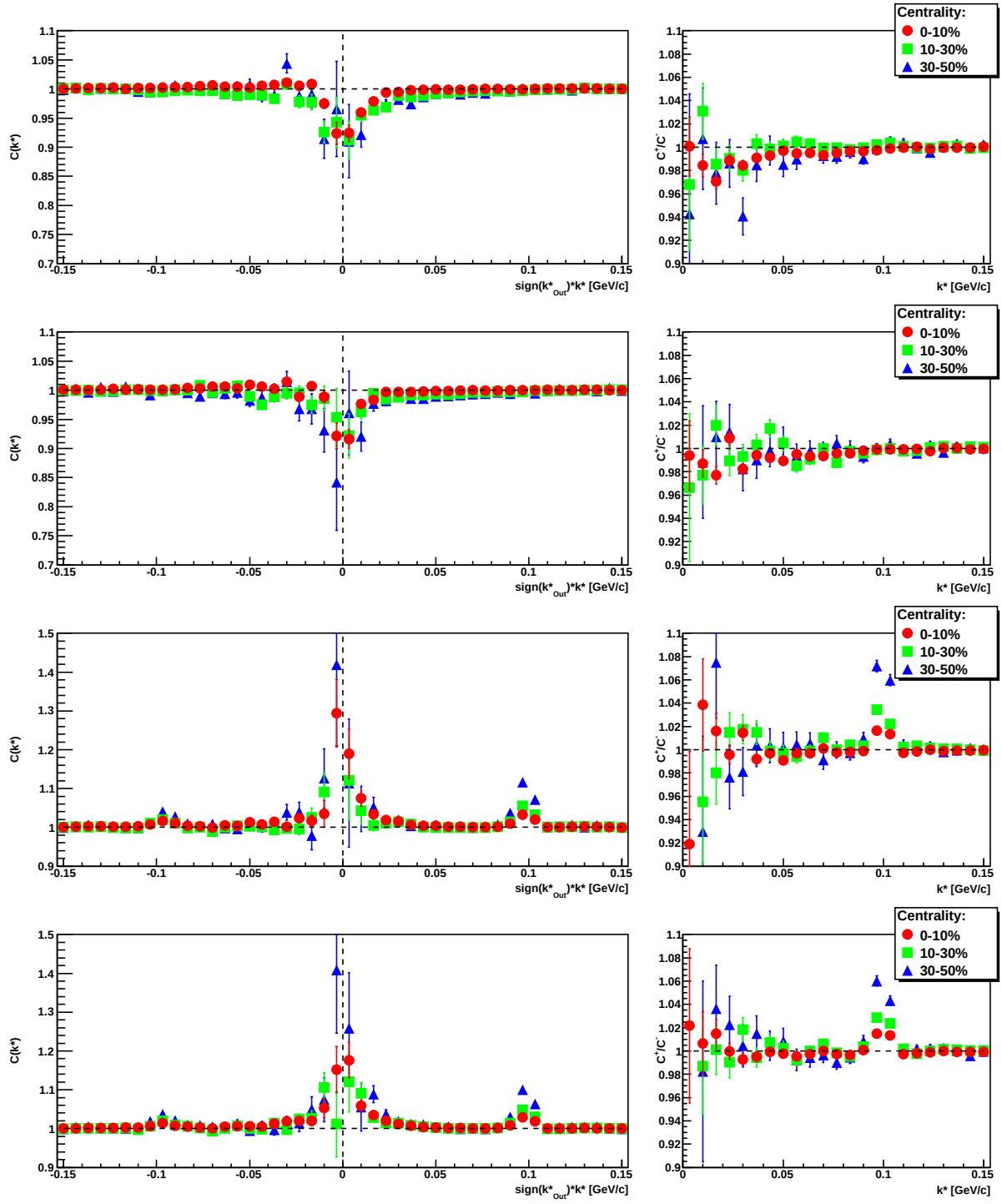

Figure 5.14: Left column: *Out* component of pion-proton correlation functions. Right column: *Out double − ratio* C^+/C^- of pion-proton correlation functions. From top to bottom $\pi^+ - p$, $\pi^- - \bar{p}$, $\pi^- - p$, $\pi^+ - \bar{p}$. Data are for Au+Au collisions at $\sqrt{s_{NN}} = 200GeV$. Red dots - central events (0-10%), green squares - intermediate events (10-30%), blue triangles - mid-central events (30-50%).

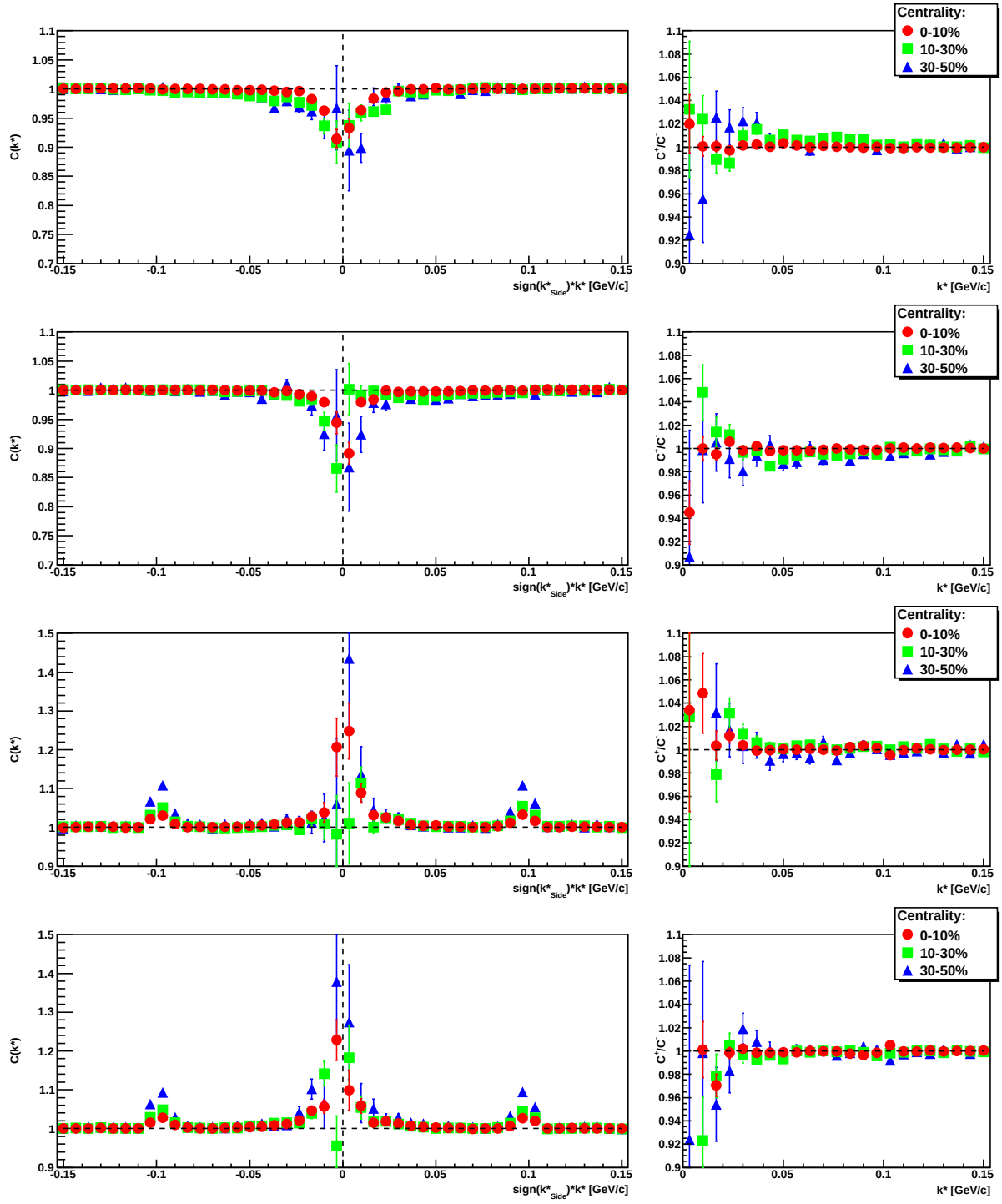

Figure 5.15: Left column: *Side* component of pion-proton correlation functions. Right column: *Side double − ratio* C^+/C^- of pion-proton correlation functions. From top to bottom $\pi^+ - p$, $\pi^- - \bar{p}$, $\pi^- - p$, $\pi^+ - \bar{p}$. Data are for Au+Au collisions at $\sqrt{s_{NN}} = 200GeV$. Red dots - central events (0-10%), green squares - intermediate events (10-30%), blue triangles - mid-central events (30-50%).

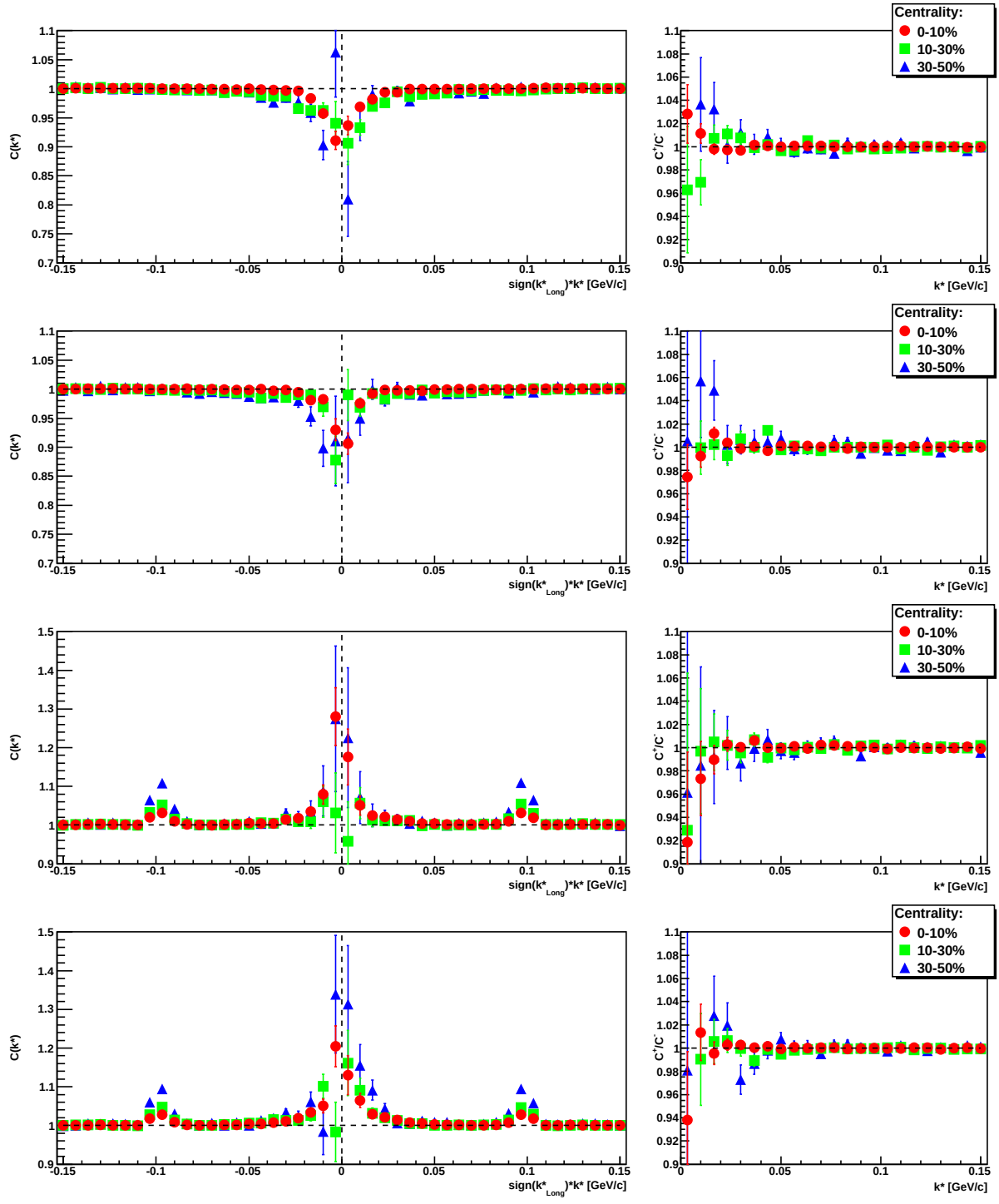

Figure 5.16: Left column: *Long* component of pion-proton correlation functions. Right column: *Long double − ratio* C^+/C^- of pion-proton correlation functions. From top to bottom $\pi^+ - p$, $\pi^- - \bar{p}$, $\pi^- - p$, $\pi^+ - \bar{p}$. Data are for Au+Au collisions at $\sqrt{s_{NN}} = 200GeV$. Red dots - central events (0-10%), green squares - intermediate events (10-30%), blue triangles - mid-central events (30-50%).

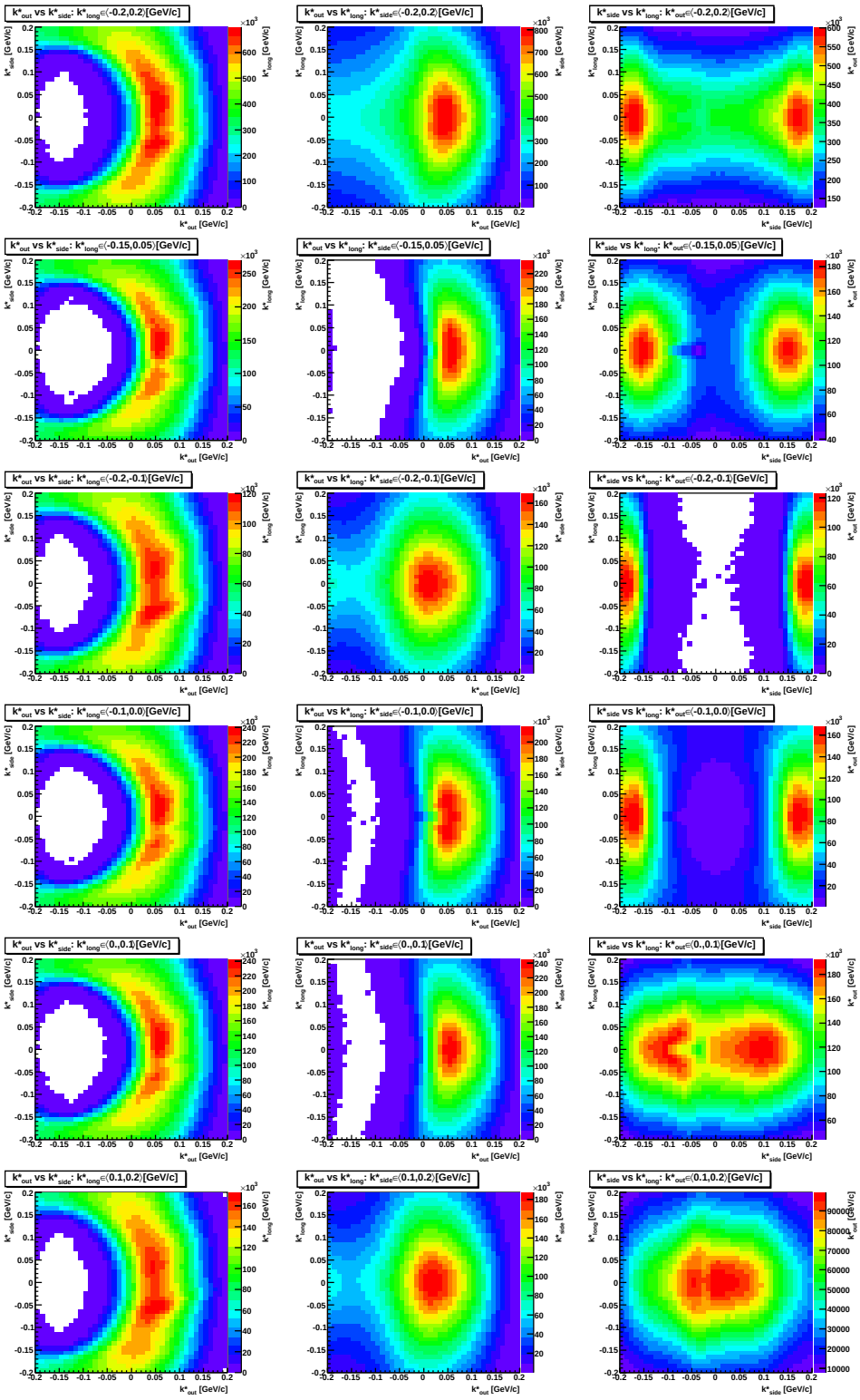

Figure 5.17: Acceptance limitations - 2-dimensional pion-proton pair distributions for various ranges of vector k^* show that STAR do not cover full phase-space of the k^*.

acceptance limitation of the STAR experiment which do not cover full phase-space of the k^* vector. Histograms presented on figure 5.17 show two-dimensional pion-proton pair distributions plotted for various ranges of vector k^*. Problems with acceptance are especially significant for negative orientation of vector k^*.

Due to difficulties with obtaining quantitative results from constructed pion-proton correlation functions in $out-side-long$ decomposition, a new technique of constructing correlation functions directly in spherical harmonics decomposition has been used for further analysis in this work [37].

5.10 Experimental pion-proton correlation functions - spherical harmonics decomposition

Experimental pion-(anti)proton correlation functions calculated directly in spherical harmonics for Au+Au collisions at $\sqrt{s_{NN}} = 200$[GeV/c] are plotted on figures 5.18 (central collisions 0-10%), 5.19 (intermediate collisions 10-30%) and 5.20 (mid-central collisions 30-50%). Presented functions are calculated for raw data and are not corrected on purity or momentum resolution.

The formalism and interpretation of particular components of correlation function calculated in spherical harmonics was introduced in section 2.4. Every figure consists of five components. The first one is real $C_0^0(k^*)$ component which carries information about the size of the source. As in $out-side-long$ representation C_0^0 shows negative correlation for like-sign pairs and positive correlation effect for unlike-sign pairs. C_0^0 functions show that for all centrality bins unlike-sign pairs show stronger correlation effect than like-sign pairs. This could suggest that size of the $\pi^+ - \bar{p}$ and $\pi^- - p$ source is smaller than size of the $\pi^+ - p$ and $\pi^- - \bar{p}$ sources. There is no physical reason for such difference. Simulations also do not show any differences in size between like-sign pairs and unlike-sign pairs. Real part of $C_1^1(k^*)$ probes space-time asymmetry in the outward direction between average emission points of pions and protons. Deviation from zero for low k^* values suggest that pions and protons are not emitted from the same regions of the source. Imaginary part of $C_1^1(k^*)$ should be flat over the full range of k^* due to symmetry in azimuthal angle. Some fluctuations can be observed for $k^* < 0.03$ one of the reasons for such fluctuations is limited statistics at this region of k^* and the second one is detector issues related to momentum reconstruction and particle identification which cannot not be eliminated during

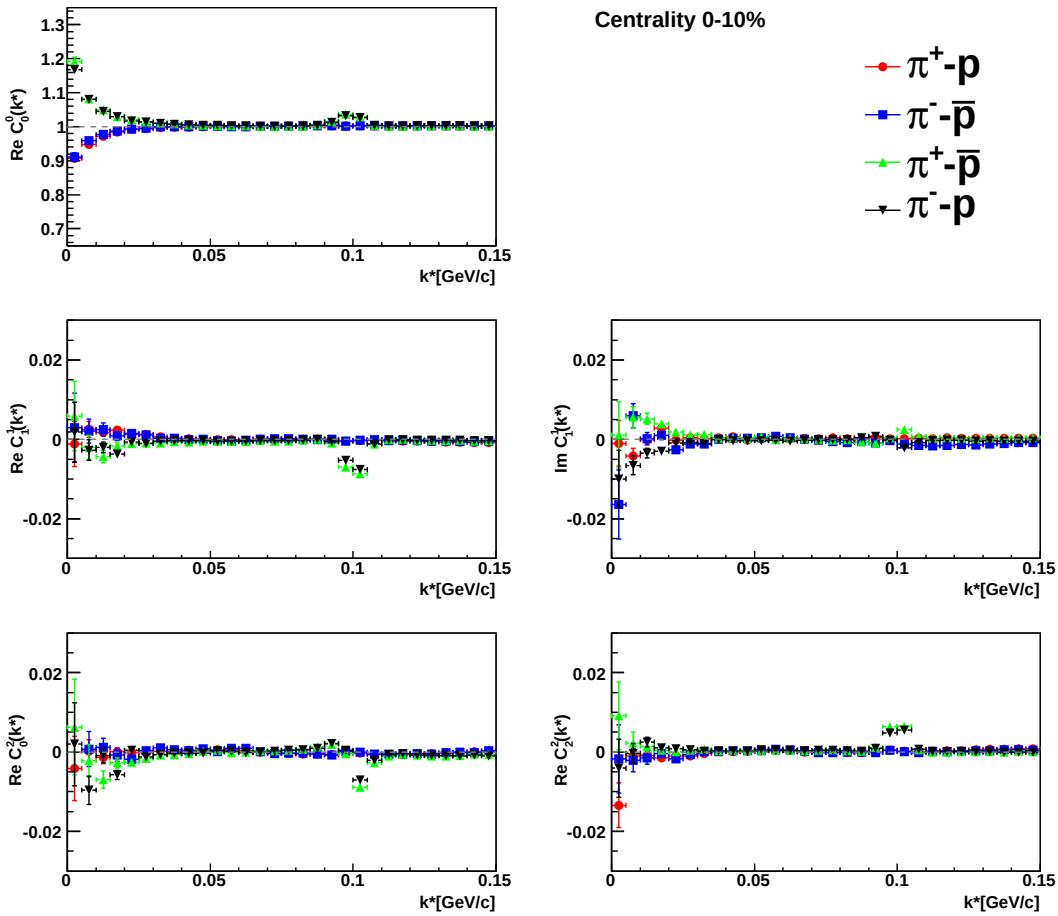

Figure 5.18: Pion-(anti)proton correlation functions in spherical harmonics. Central (0-10%) Au+Au collisions at $\sqrt{s_{NN}} = 200$[GeV/c].

data analysis process. Real parts of $C_0^2(k^*)$ and $C_2^2(k^*)$ components of the correlation function may indicate difference in size between *out*, *side*, and *long* directions but observed effect is smaller than statistical errors.

All components of correlation functions for $\pi^+ - \bar{p}$ and $\pi^- - p$ show lambda peaks around $k^* = 0.1$[GeV/c], but as in $out - side - long$ representation these peaks are located above femtoscopic effect.

Before extracting quantitative information from the fit procedure presented functions must be corrected on purity (sec. 5.4) and on momentum resolution (sec. 5.5). In further discussion only real parts of $C_0^0(k^*)$ and $C_1^1(k^*)$ components which are the most important for this thesis will be discussed.

Functions corrected on purity are presented on figure 5.21. Every figure shows comparison of different centrality bins for $\pi^+ - p$, $\pi^- - \bar{p}$, $\pi^+ - \bar{p}$ and $\pi^- - p$ correspondingly. Observed

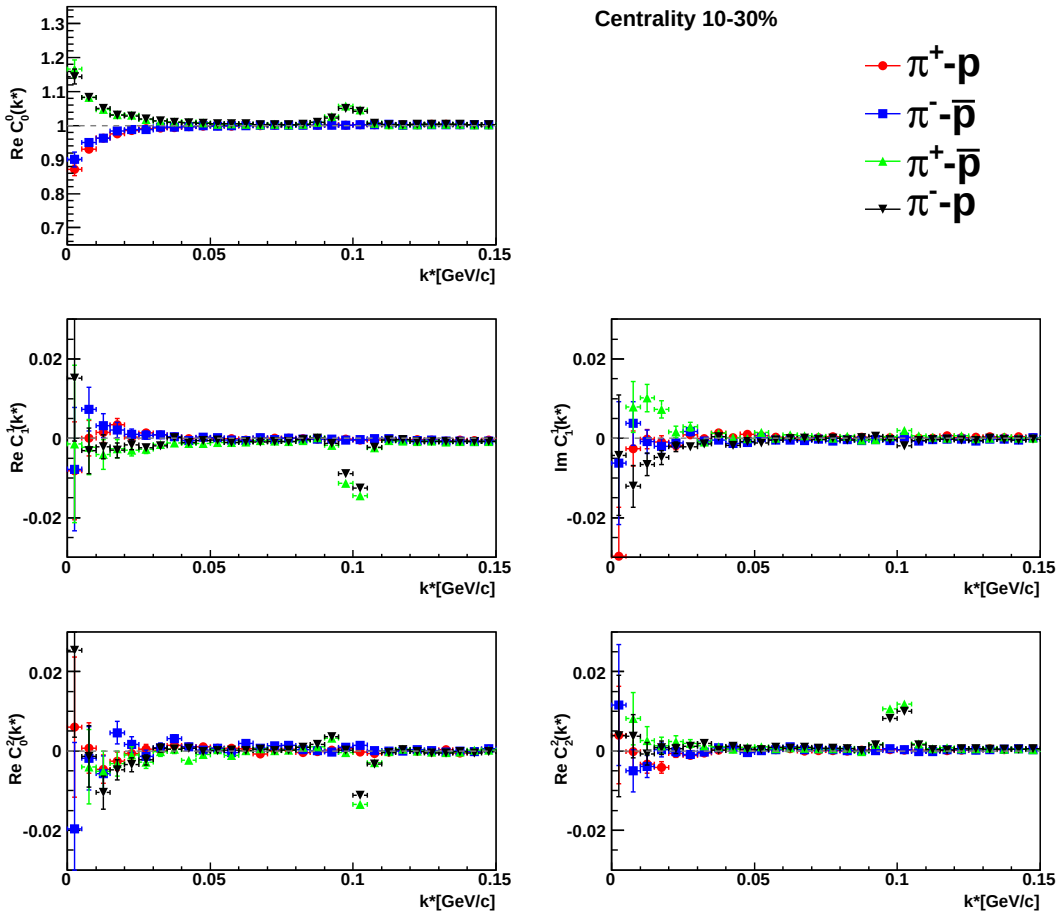

Figure 5.19: Pion-(anti)proton correlation functions in spherical harmonics. Intermediate (10-30%) Au+Au collisions at $\sqrt{s_{NN}} = 200$[GeV/c].

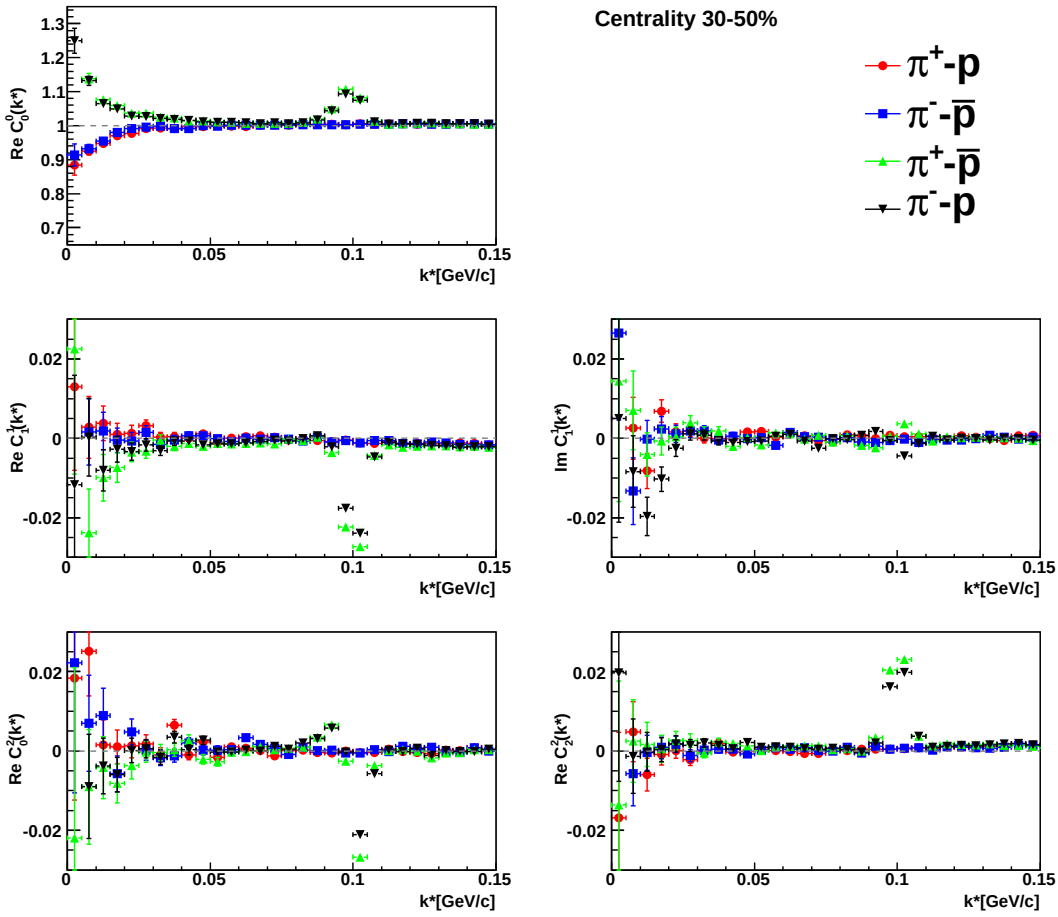

Figure 5.20: Pion-(anti)proton correlation functions in spherical harmonics. Mid-central (30-50%) Au+Au collisions at $\sqrt{s_{NN}} = 200$[GeV/c].

correlation effect is weaker for central collisions (red dots) than for intermediate (blue squares) and mid-central events (green triangles). Centrality dependence seems to be very small. Points of the correlation functions calculated for different centralities partially overlap. This is due to sensitivity of the correlation function to source size and its asymmetry. Very small changes in pion-proton correlation function gives relatively bigger changes in observed source size. This feature causes lots of problems with stability of the fit.

A fit procedure (sec. 5.6) can be applied to the corrected functions. The most appropriate is to fit functions calculated for full-field data and reversed-full-field data separately and then to average obtained fit results. Figures 5.22 and 5.23 show $\pi^+ - \bar{p}$ and $\pi^- p$ correlation functions calculated for full field and reversed full field datasets. Fitted functions are purity corrected. Correction on momentum resolution is applied during the fit procedure to the momenta of the experimental pairs used for constructing theoretical correlation function. Figures present real $C_0^0(k^*)$ and $C_1^1(k^*)$ components of the experimental correlation functions (black points) and two dimensional χ^2-maps from the fit procedure. χ^2-maps show found minimum (best source parameters) in $\sigma_{out} - \mu_{out}$ coordinates. The best fit for every function is plotted with red, green or blue points. Fit results show clear centrality dependence of the size and space-time asymmetry of the pion-proton source. χ^2-maps show relatively high value of χ^2 for the best fit. This may be related to Gaussian source parametrization which do not necessarily correspond to physical source, also very essential contribution is from fluctuations of the correlation functions for large value of k^*. Although these fluctuations around unity for C_0^0 component or around zero for C_1^1 component are very small a contribution to χ^2 is significant due to very high statistics in this region of k^* what gives small statistical error bars. The best $chi^2/ndf \approx 6$ is for mid-central collisions mainly due to lower statistics.Due to high values of χ^2/ndf in the obtained fit results extracted statistical errors are multiplied by $\sqrt{\chi^2/ndf}$. For central and intermediate events statistical errors dominates over systematic errors. In case of mid-central events statistical and systematic errors are comparable.

Fitted values of source parameters are presented in table 5.5 for separate full field and reversed full field datasets and in table 5.6 for averaged full field and reversed full field datasets. Statistical errors come from the fit procedure. Systematic errors are due to applied corrections on purity and momentum resolution. In case of averaged full field and reversed full field data additionally from discrepancy between them. Source size of $\pi^+ - \bar{p}$ system for central collisions is around 10.8[fm] and for $\pi^- - p$ system around 12[fm]. Shift between average emission

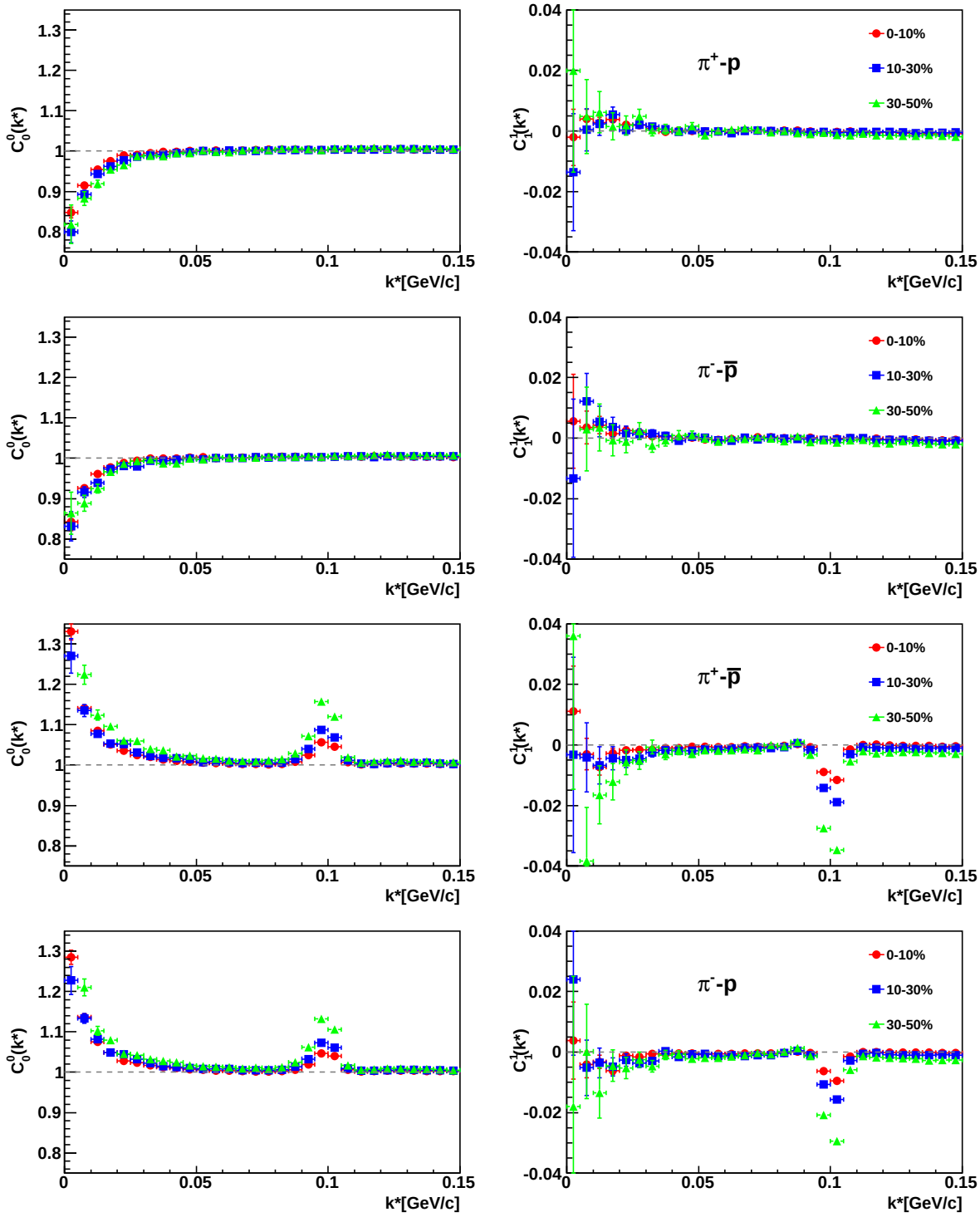

Figure 5.21: Pion-(anti)proton correlation functions corrected on purity. From top to bottom: $\pi^+ - p$, $\pi^- - \bar{p}$, $\pi^+ - \bar{p}$ and $\pi^- - p$.

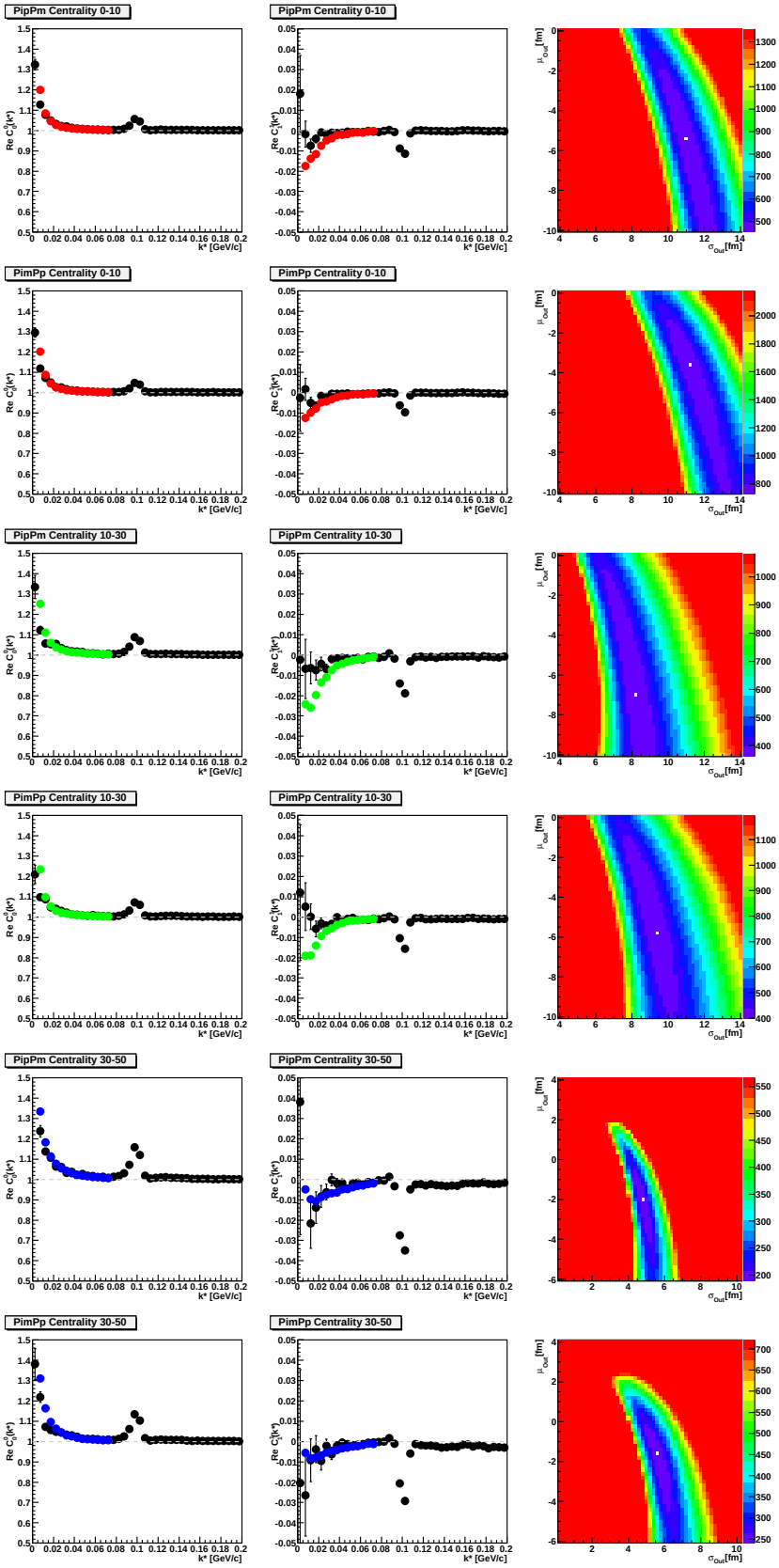

Figure 5.22: Fit results for unlike-sign pion-proton pairs. Black points - corrected experimental function, red,green,blue - points best fit function. Full-Field data of Au+Au collisions at $\sqrt{s_{NN}} = 200$[GeV/c]. Left column $ReC_0^0(k^*)$, middle column $ReC_1^1(k^*)$, right column χ^2-map.

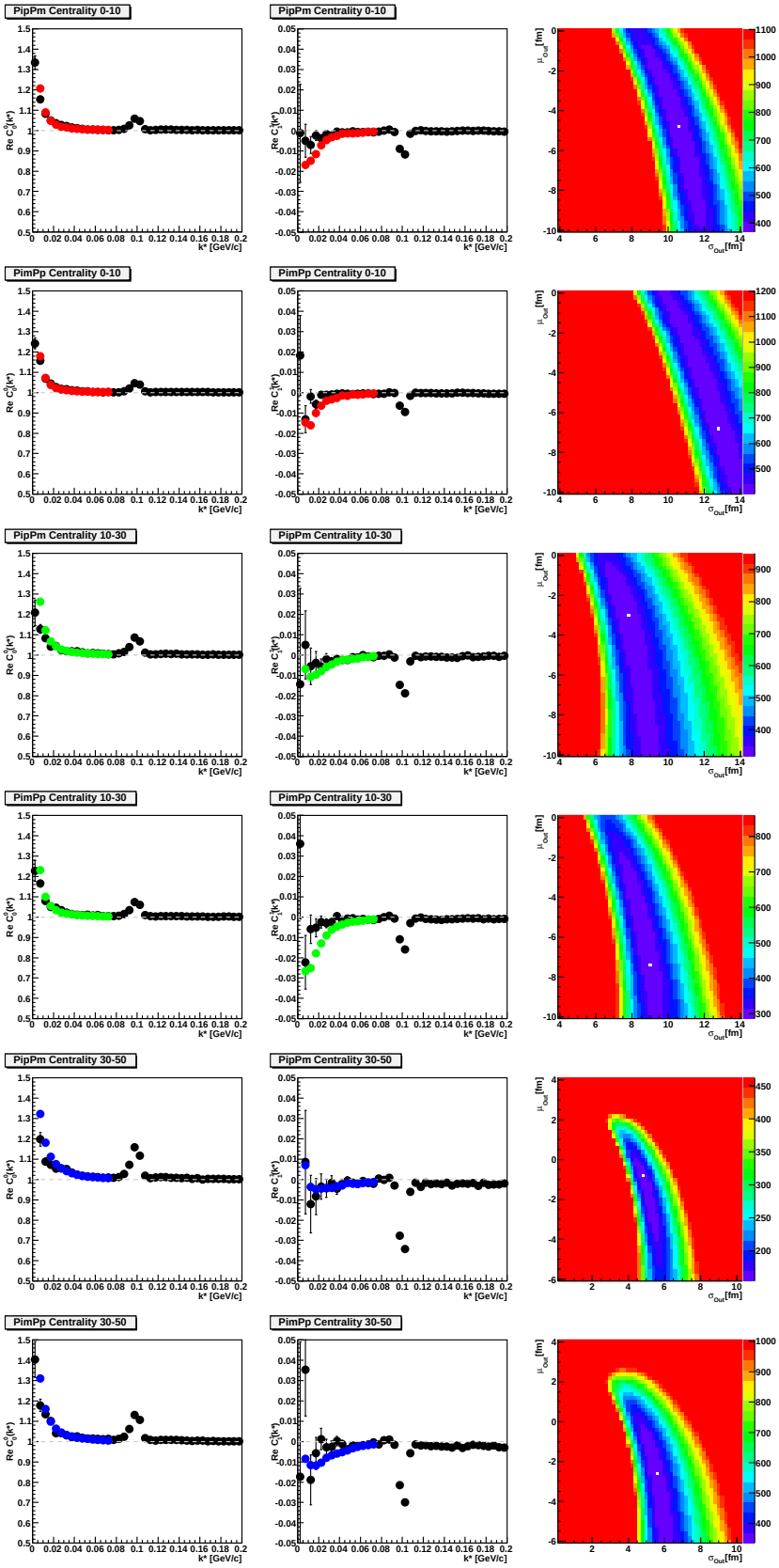

Figure 5.23: Fit results for unlike-sign pion-proton pairs. Black points - corrected experimental function, red,green,blue - points best fit function. Reversed-Full-Field data of Au+Au collisions at $\sqrt{s_{NN}} = 200$[GeV/c]. Left column $ReC_0^0(k^*)$, middle column $ReC_1^1(k^*)$, right column χ^2-map.

Centrality	Pair	FF		RFF	
		σ_{out}[fm]	μ_{out}[fm]	σ_{out}[fm]	μ_{out}[fm]
0-10%	$\pi^+ - \bar{p}$	$11.0^{+1.6+0.2}_{-1.6-0.6}$	$-5.4^{+3.2+0.2}_{-3.2-2.0}$	$10.6^{+1.4+0.2}_{-1.4-1.0}$	$-5.0^{+3.6+0.2}_{-2.2-2.8}$
	$\pi^- - p$	$11.2^{+2+0.2}_{-2-0.2}$	$-3.6^{+3+0.2}_{-3-0.4}$	$12.8^{+2.3+0.2}_{-1.5-2.0}$	$-6.8^{+3.8+0.2}_{-2.7-5.0}$
10-30%	$\pi^+ - \bar{p}$	$8.2^{+2.2+0.2}_{-1.4-1.0}$	$-7.0^{+6.5+0.2}_{-5.7-4.4}$	$7.8^{+1.3+0.2}_{-2.0-0.4}$	$-3.0^{+2.7+0.2}_{-4.0-1.0}$
	$\pi^- - p$	$9.4^{+1.5+0.2}_{-2.3-0.8}$	$-5.8^{+3.8+0.2}_{-3.8-2.8}$	$9.0^{+1.3+0.2}_{-1.3-0.4}$	$-7.4^{+3.2+0.2}_{-3.2-1.8}$
30-50%	$\pi^+ - \bar{p}$	$5.6^{+0.6+0.2}_{-1.2-0.2}$	$-1.6^{+1.2+0.2}_{-1.2-0.2}$	$5.6^{+1.4+0.2}_{-1.4-0.2}$	$-2.6^{+2.1+0.2}_{-2.8-0.2}$
	$\pi^- - p$	$4.8^{+0.5+0.2}_{-0.5-0.2}$	$-2.0^{+0.2+0.2}_{-0.2-0.2}$	$4.8^{+0.5+0.2}_{-0.5-0.2}$	$-0.8^{+0.2+0.2}_{-0.2-0.2}$

Table 5.5: Fit results for unlike-sign pairs: size and space-time asymmetry of pion-(anti)proton source in Au+Au collisions at $\sqrt{s_{NN}} = 200$[GeV/c]. First error is statistical error from fit procedure, second error is systematic from applied corrections.

Centrality	Pair	$\langle FF + RFF \rangle$	
		σ_{out}[fm]	μ_{out}[fm]
0-10%	$\pi^+ - \bar{p}$	$10.8^{+2.1+0.3}_{-2.1-1.2}$	$-5.2^{+5+0.3}_{-4-3}$
	$\pi^- - p$	$12^{+3+0.3}_{-2.5-0.3}$	$-5.2^{+5+0.3}_{-4-5}$
10-30%	$\pi^+ - \bar{p}$	$8^{+2.6+0.3}_{-2.4-1.1}$	$-5^{+7+0.3}_{-7-4}$
	$\pi^- - p$	$9.2^{2.0+0.3}_{-2.6-0.9}$	$-6.6^{+5+0.3}_{-5-3}$
30-50%	$\pi^+ - \bar{p}$	$5.6^{+0.3+0.3}_{-0.3-0.3}$	$-2.1^{+0.3+0.3}_{-0.3-0.3}$
	$\pi^- - p$	$4.8^{+0.3+0.3}_{-0.3-0.3}$	$-1.4^{+0.3+0.3}_{-0.3-0.3}$

Table 5.6: Averaged (full field and reversed full field data sets) fit results for unlike-sign pairs: size and space-time asymmetry of pion-(anti)proton source in Au+Au collisions at $\sqrt{s_{NN}} = 200$[GeV/c]. First error is statistical error from fit procedure, second error is systematic from applied corrections and from discrepancy between full field and reversed full field results.

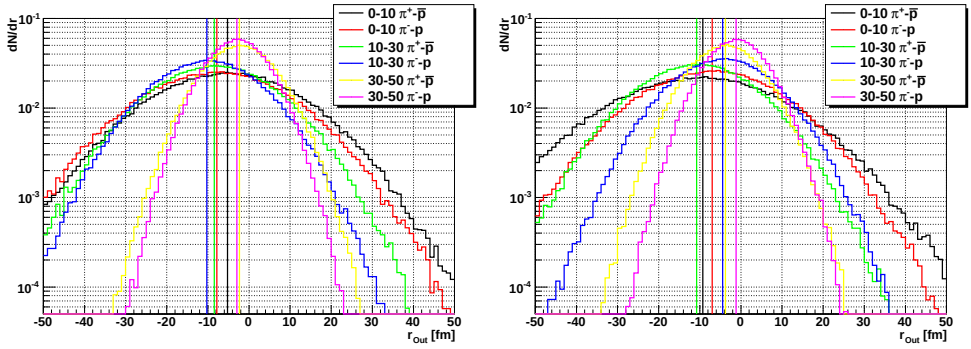

Figure 5.24: Two particle pion-proton source distributions obtained from a fit to experimental data procedure. Left panel is for full field dataset, right panel is for reversed full field dataset.

points in both cases is around -5.2[fm]. Intermediate events gives source size 8[fm] for $\pi^+ - \bar{p}$ and 9.2[fm] for $\pi - -p$ and asymmetry -5[fm] and -6.6[fm] correspondingly. For mid-central events source size σ_{out} is around 5.6[fm] for $\pi^+ - \bar{p}$ and 4.8[fm] for $\pi^- - p$ pairs and asymmetry μ_{out} is around -2.1[fm] and -1.4[fm] correspondingly. All obtained quantitative results are consistent with each other within estimated error bars and show centrality dependence. *Out* components of the two particle distributions of the fitted Gaussian sources in LCMS are plotted on figure 5.24. Fit procedure assumes symmetric Gaussian distribution in *side*, *long* and *time* components with the width equal to the width of the *out* component.

Summary of the fit results is presented on figure 5.25[3] which shows space-time asymmetry of the source as a function of a source size. Plotted contours are the ellipses of covariances fitted to χ^2-maps. Values of μ_{out} and σ_{out} are correlated and for approximation to zero size system asymmetry between average space-time emission points of pions and protons also goes to zero.

[3]Results presented on V Workshop on Particle Correlations and Femtoscopy, CERN 2009

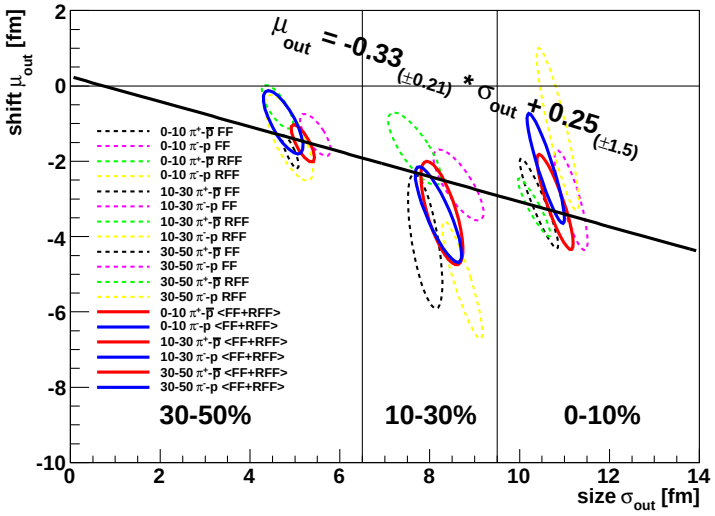

Figure 5.25: Ellipses of covariances fitted to the χ^2-maps.

Chapter 6

Discussion and interpretation

Discussion and interpretation of achieved experimental results can be done by comparison to model predictions. For this purpose two models are used in this thesis `Therminator 2.0 beta` and `UrQMD` version 3.3. Correlation functions calculated from simulated data are constructed in the same way as the experimental functions. Also method of extracting parameters of the source is the same. In addition to correlation functions that can be calculated from simulated or experimental data, distributions of space-time freeze-out coordinates can be obtained from simulations. This gives important feedback on possible source structure and sequence of emission of different particle species.

6.1 Dependence of the $\pi - p$ correlation function on FSI and space-time structure of the source

Numerical calculations provide important information about interactions between particles. Momenta of the particles generated in Therminator are used for calculation of the correlation functions in three different cases, when Coulomb and strong interactions are enabled, when only Coulomb interaction is enabled and when only strong interaction is enabled. Figure 6.1 depicts all three cases for like-sign pairs and unlike-sign pairs. Calculated functions show that strong interaction is negligible for pion-proton pairs. As the Coulomb interactions is symmetric with respect to the charge of the particles, in discussion of simulated data only like-sign pairs and unlike-sign pairs are discussed.

The same data is used to study the influence of the source size and its asymmetry on correlation functions. Figure 6.2 shows $ReC_0^0(k^*)$ and $ReC_1^1(k^*)$ components of the pion-proton

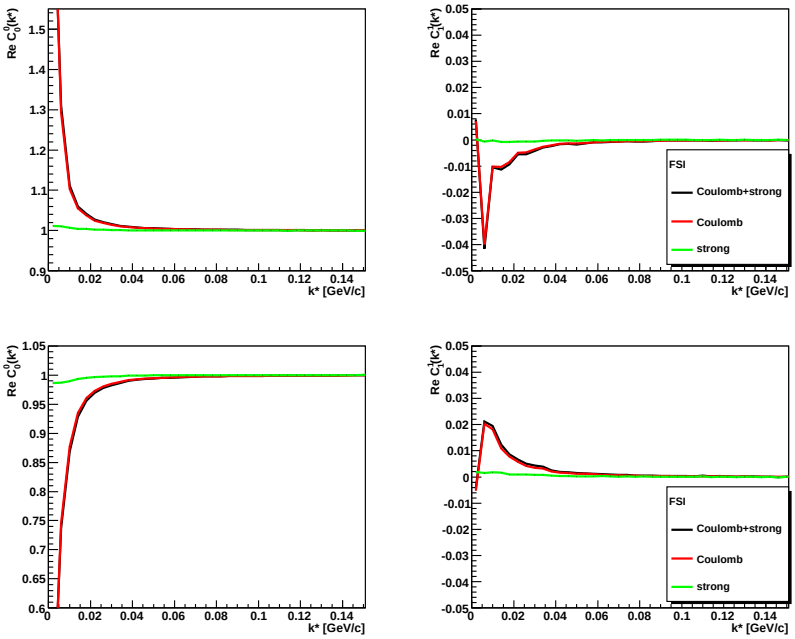

Figure 6.1: Pion-proton correlation functions - Coulomb and strong interactions. Upper panels - unlike-sign pairs. Lower panels like-sign pairs.

correlation functions in spherical harmonics for various size of the system and various values of the distance between average emission points. $ReC_0^0(k^*)$ components show stronger correlation for smaller source sizes. $ReC_1^1(k^*)$ components show stronger effect for higher values of asymmetry.

6.2 Simulations with Therminator

Therminator has been already briefly discussed in section 1.4.2. Parameters of the freeze-out are set to the values that reproduce central (0-10%), intermediate (10-30%) and mid-central (30-50%) Au+Au collisions at $\sqrt{s_{NN}} = 200GeV$.

Based on the simulated data, pion-proton correlation functions are constructed. Figure 6.3 shows *out* component of the pion-proton correlation function. Upper plot is for the unlike-sign pairs and lower plot is for like-sign pairs. Figure 6.4 shows two real components $C_0^0(k^*)$ and $C_1^1(k^*)$ of the correlation functions calculated in spherical harmonics. As in experimental data functions show centrality dependence of the observed size of the system and its asymmetry. Values of the size and asymmetry of the system obtained from the fit procedure are presented in table 6.1. Size of the pion-proton source varies from 9.9fm for like-sign pairs in central

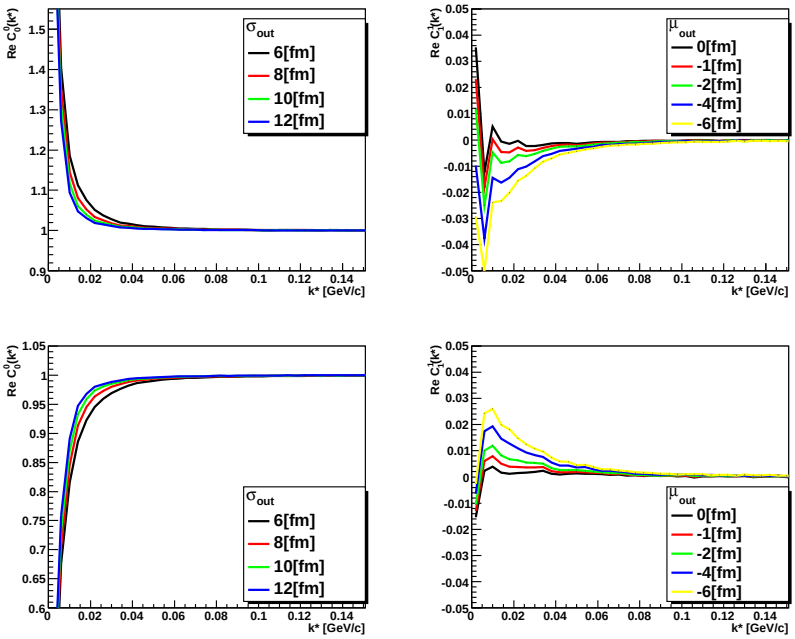

Figure 6.2: Pion-proton correlation functions - size and shift dependence. Upper panels are for unlike-sign pairs. Lower panels are for like-sign pairs.

collisions to 7fm for mid-central collisions. Centrality dependence of the size of the system is weaker than in experiment. Source size for central events in Therminator is about 10% smaller than source size observed in the STAR experiment. Reversed situation is for mid-central data where simulated data gives bigger size than experiment. Magnitude of asymmetry varies from -7.8fm for central collisions to -5fm for mid-central collisions and exceeds asymmetry measured from experimental data.

Simulated data gives opportunity to calculate characteristics of the quantities that are not available in experimental data. Images of the pion and proton sources are plotted on figure 6.5. Two dimensional histograms show distributions in transverse plain of freeze-out spacial coordinates of pions and protons that contribute to the correlation function. This figure tells us that emission points of protons are more concentrated at the edge of the source than emission points of pions and that pion source is bigger than proton source.

Two particle pion-proton pair separation distributions for investigated centrality bins are plotted on figure 6.6. Distributions are plotted for like-sign pairs as well as unlike-sign pairs. It is clearly seen that there is no difference in source distribution between like-sign pairs and unlike-sign pairs. dN/dr_{out} shows spacial asymmetry of the source. Also distribution of the emission time difference shows that emission process of pions and protons differs. No asymmetry is

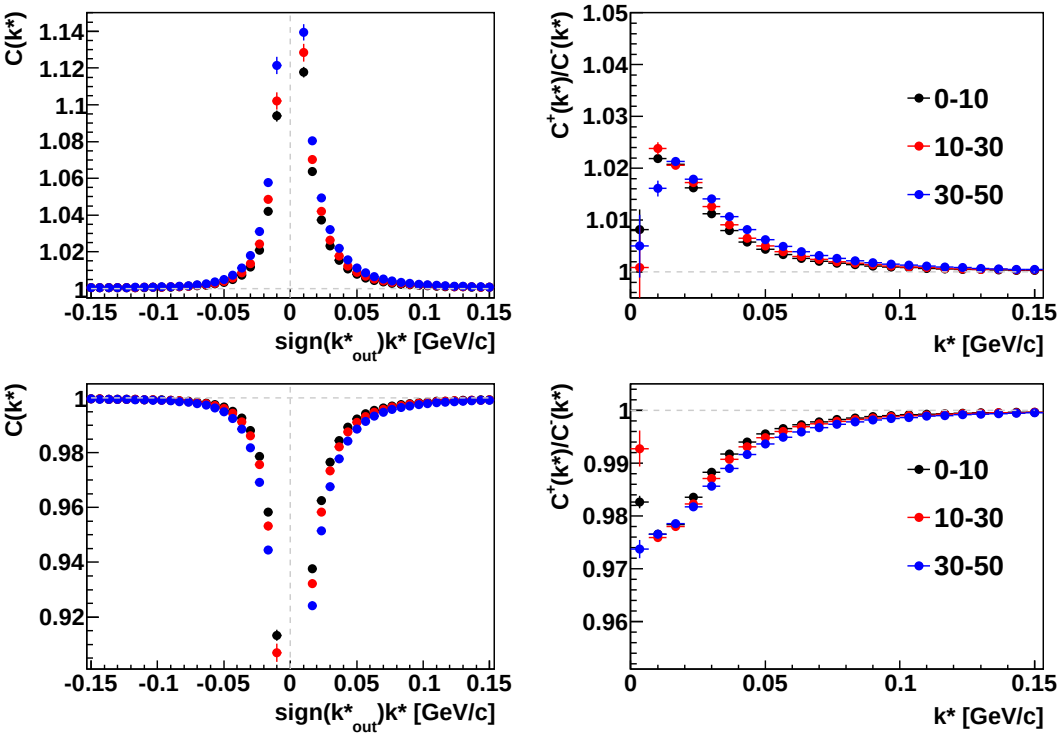

Figure 6.3: Pion-proton correlation functions - therminator.

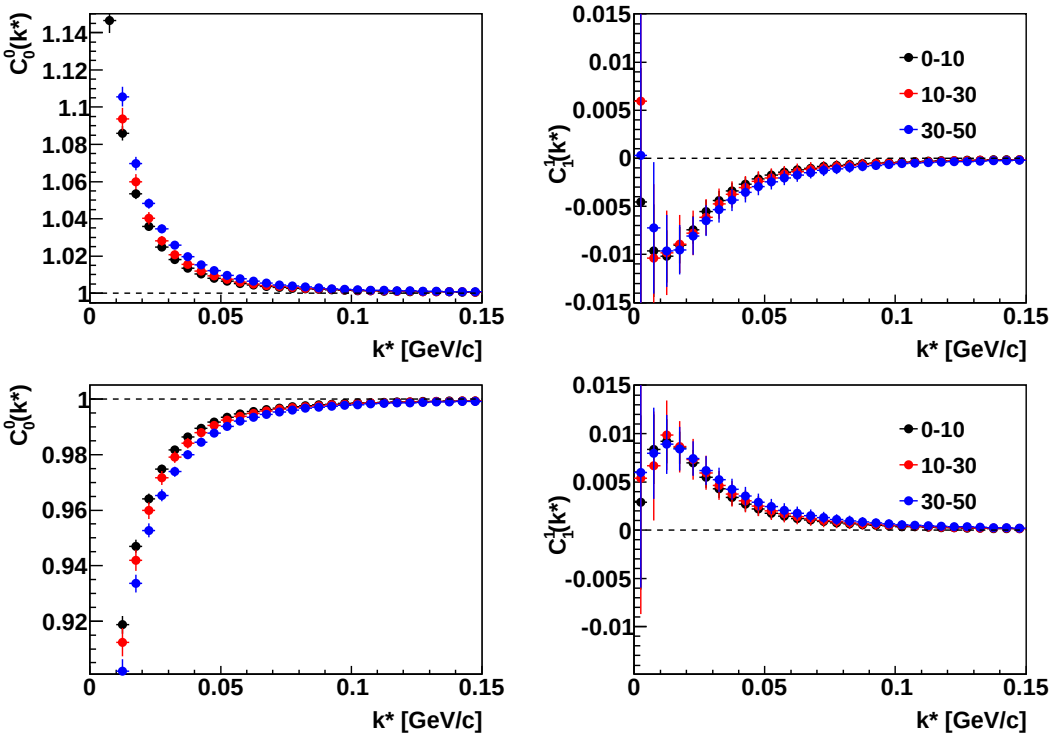

Figure 6.4: Pion-proton correlation functions in spherical harmonics - therminator.

Centrality	Pair	σ_{out}[fm]	μ_{out}[fm]
0-10%	like-sign	$9.9^{+1.0}_{-1.0}$	-7.8^{+3}_{-3}
	unlike-sign	$9.5^{+0.6}_{-0.6}$	$-6.9^{+1.2}_{-1.6}$
10-30%	like-sign	$9^{+0.5}_{-0.5}$	$-7.1^{+0.6}_{-0.8}$
	unlike-sign	$8.3^{+0.5}_{-0.5}$	$-6.1^{+0.6}_{-0.8}$
30-50%	like-sign	$7.3^{+0.4}_{-0.4}$	$-5.4^{+0.7}_{-1.1}$
	unlike-sign	$7^{+0.4}_{-0.4}$	$-5^{+0.9}_{-0.5}$

Table 6.1: Fit results - therminator. 3D Gaussian profile in LCMS.

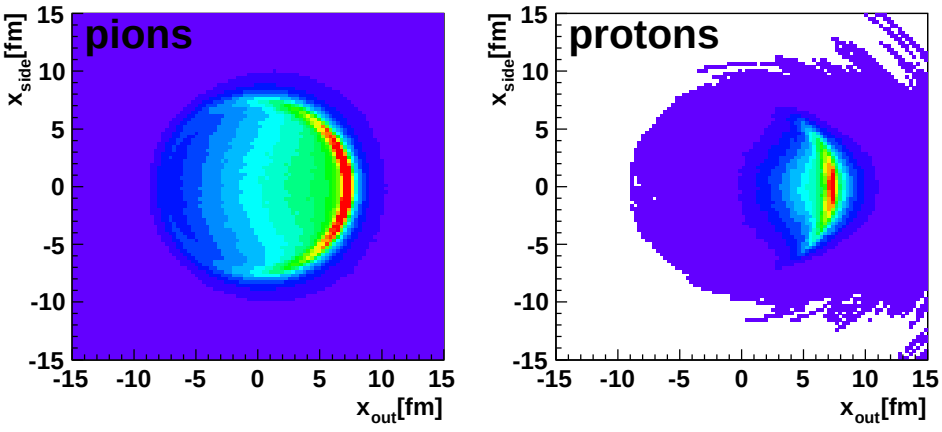

Figure 6.5: Image of pion source - left and proton source - right. Therminator results.

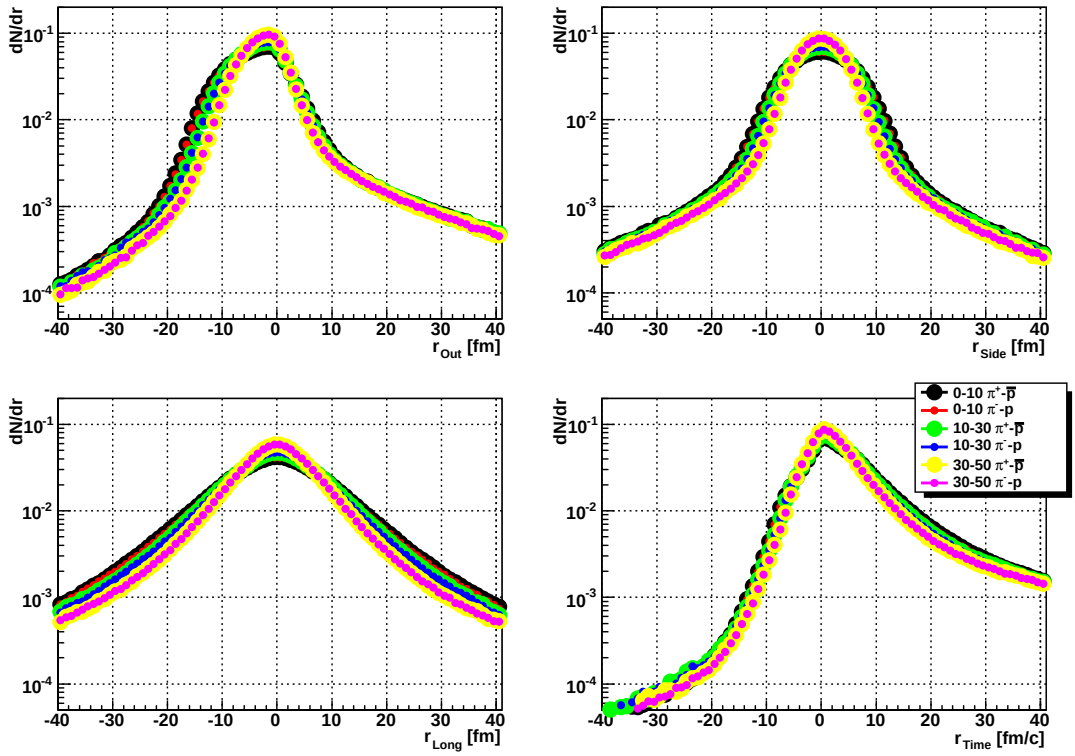

Figure 6.6: Two particle pion-proton pair separation distribution from Therminator. Upper left panel shows distribution in *out* direction, upper right panel shows *side* direction, lower left panel shows *long* direction and lower right panel shows two particle emission time difference distribution. Distributions constructed for pairs that contribute to the correlation effect ($k^* <$ 0.07GeV/c)

observed in *side* and *long* directions. Centrality dependence of the size and asymmetry of pion-proton source can be also observed.

Observed asymmetry contains two components, one related to the spacial shift between emission points and another related to the emission time difference. Figure 6.7 shows emission time difference versus separation of the emission points for pairs that contribute to the correlation effect. Six histograms present data for like-sign pairs (left column) and unlike-sign pairs (right column), central (top), intermediate (middle) and mid-central (bottom) Au+Au collisions. We can observe that both space and time components are correlated. Bigger spacial shift corresponds to bigger emission time difference.

Positive value of r_{Time} corresponds to the scenario when proton is emitter earlier than pions. Histograms show that most of the pions that contribute to the correlation effect are emitted later than protons. Opposite scenario when pion is emitter earlier than proton is very rare. For central

collisions emission time difference reaches higher values than for intermediate and mid-central collisions what is in agreement with the statement that bigger sources lives longer.

Results of simulations with `Thermiantor` with implemented hydrodynamics of Au+Au collisions at $\sqrt{s_{NN}} = 200$GeV are qualitatively in agreement with experimental measurements. Mechanisms implemented in the model suggest that observed asymmetry in pion-proton system may arise from collective behavior of the created system.

6.3 Simulations with UrQMD

UrQMD model was briefly discussed in section 1.4.1. About 3 million minimum bias events of Au+Au collisions at $\sqrt{s_{NN}} = 200$GeV was generated. Based on impact parameter events from central (0-10%), intermediate (10-30%) and mid-central (30-50%) collisions were selected for the analysis. Figure 6.8 presents distribution of the impact parameter *b* and selected centrality bins of the generated events.

Out component of the pion-proton correlation functions and corresponding $double-ratios$ calculated from simulated UrQMD data are presented on figure 6.9. Functions calculated in spherical harmonics are presented on figure 6.10. In both cases functions are calculated for like-sign pairs (lower panels) and unlike-sign pairs (upper panels). Black points show functions for central events, red points are for intermediate events and mid-central events are marked with blue points. *Out* $double-ratios$ and real $C_1^1(k^*)$ component of the correlation functions show space-time asymmetry of the created source.

Quantitative results obtained from the fit procedure are presented in table 6.2. In the fit procedure like in experimental fit a 3D Gaussian profile of the source in the longitudinal co-moving system LCMS was assumed. Extracted sizes of the pion-proton system for investigated centralities show centrality dependane, but exceed values obtained from the experimental functions in every centrality bin, from about 25% for central events to about 50% for mid-central events. Values of space-time asymmetry do not show clear centrality dependence. For central events and intermediate events they are close to the experimental values but for the mid-central events asymmetry of the system in UrQMD data two times exceeds the experimental value.

Generated freeze-out coordinates allow for construction of two dimensional distributions of emission points of pions and protons. Figure 6.11 shows two-dimensional distributions of pions and protons emission points. Distributions are calculated in transverse plain. Emission points of

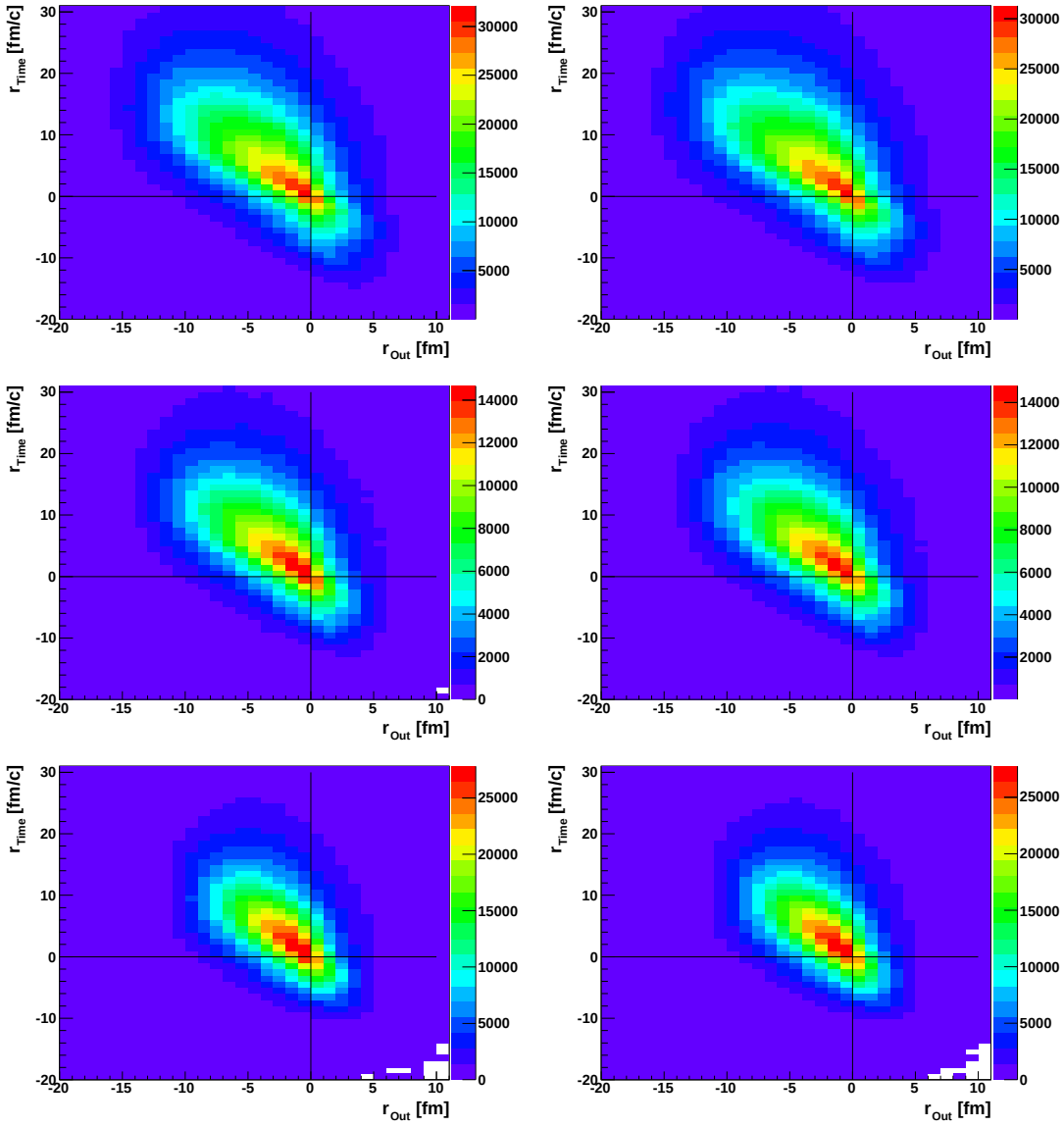

Figure 6.7: Distribution of the emission time difference versus separation of the emission points - Therminator. Left panels show data for like-sign pion-proton pairs. Right panels show data for unlike-sign pion-proton pairs. Upper plots are for central (0-10%) Au+Au collisions, middle plots are for intermediate (10-30%) collisions and lower plots are for mid-central (30-50%) collisions.

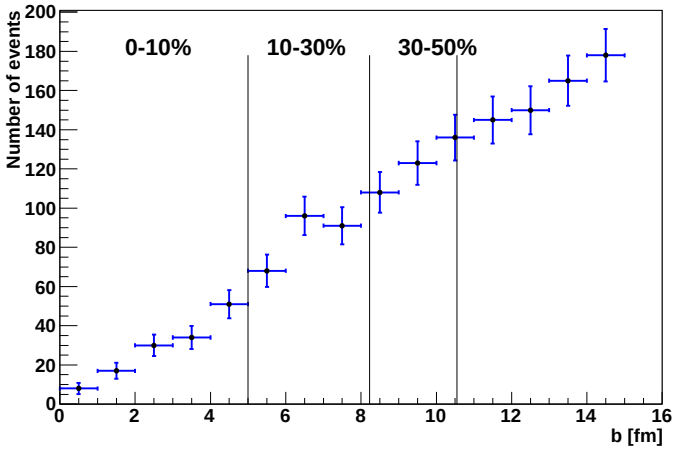

Figure 6.8: Distribution of the impact parameter in Au+Au collisions at $\sqrt{s_{NN}} = 200$GeV - UrQMD.

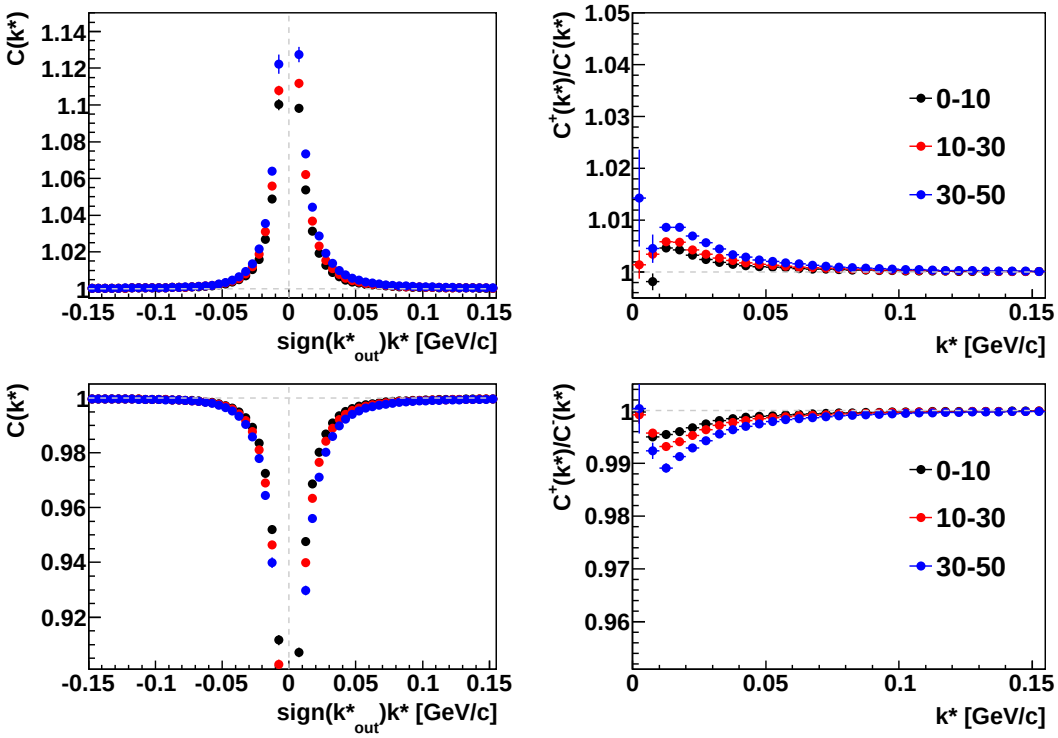

Figure 6.9: Pion-proton correlation functions - UrQMD.

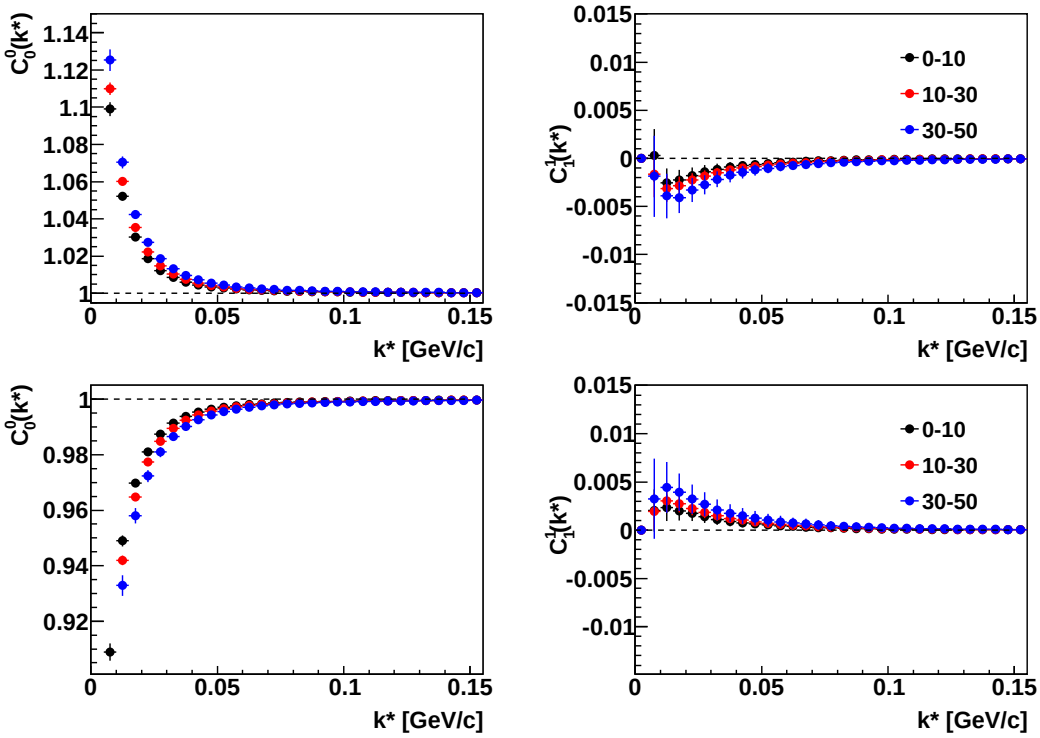

Figure 6.10: Pion-proton correlation functions in spherical harmonics - UrQMD.

Centrality	Pair	σ_{out}[fm]	μ_{out}[fm]
0-10%	like-sign	$15.8^{+0.2}_{-0.2}$	$-5.2^{+0.2}_{-0.2}$
	unlike-sign	$15^{+0.3}_{-0.3}$	$-4.4^{+0.2}_{-0.2}$
10-30%	like-sign	$12.8^{+0.2}_{-0.2}$	$-4.8^{+0.2}_{-0.2}$
	unlike-sign	$12.8^{+0.2}_{-0.2}$	$-4.8^{+0.2}_{-0.2}$
30-50%	like-sign	$10.8^{+0.2}_{-0.2}$	$-5.2^{+0.2}_{-0.2}$
	unlike-sign	$10.4^{+0.2}_{-0.2}$	$-5.6^{+0.2}_{-0.2}$

Table 6.2: Fit results - UrQMDv3.3. 3D Gaussian profile of the source in LCMS.

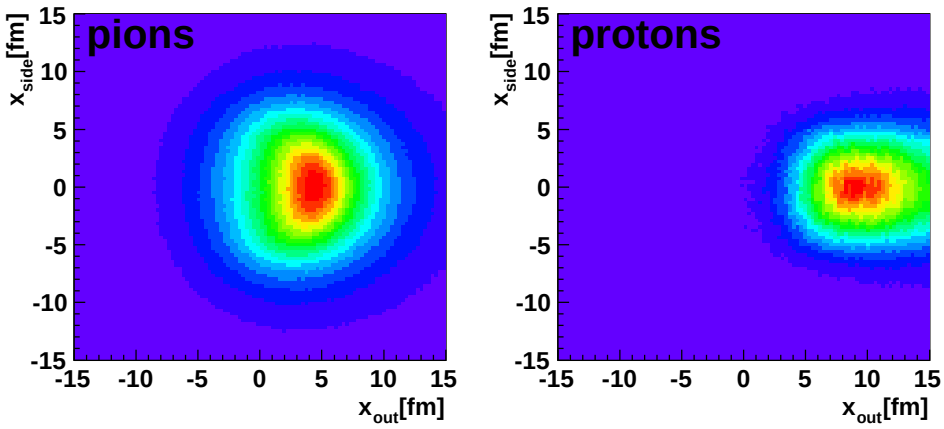

Figure 6.11: Image of pion source - left and proton source - right. UrQMDv3.3 results.

pions are distributed almost over the whole source, while emission points of protons are shifted towards the edge of the source. Shift for the protons is stronger than shift for the pions also proton source is smaller than the source of pions. No asymmetry is observed in *side* direction.

Pion-proton pairs that contributed to correlation functions were used to construct two-particle separation distributions - figure 6.12. Like in case of Therminator data there is no difference in presented histograms between like-sign pairs and unlike-sign pairs. Distributions in *side* and *long* directions are symmetric. *Out* component plotted on upper left panel shows asymmetry of the source also emission time difference distribution plotted on lower right panel shows difference in emission scenario between pions and protons. Observed asymmetry in $time$ is not so strong as in case of Therminator. Source size of the system created in UrQMD simulations is bigger than size of the system in Therminator mainly due to the long tail on the negative side of the dN/dr_{out} distribution.

Emission time difference versus separation of the emission points for pairs that contribute to the correlation effect is plotted on figure 6.13. Histograms show data for like-sign pairs (left column) and unlike-sign pairs (right column), central (top), intermediate (middle) and mid-central (bottom) Au+Au collisions. We can observe shift between emission points of pions and protons. Emission time difference is almost symmetric with respect to the $r_{Time} = 0$ axis. It means that probability of the scenario when pion is emitted earlier than proton is likely the same as the scenario when pion is emitted later than proton. No correlation between space and time components of asymmetry for pion-proton system is observed in UrQMD data.

Bigger emission time differences observed in central Au+Au collisions suggest that evolution of source created in central heavy ion collision lasts longer than evolution of smaller source

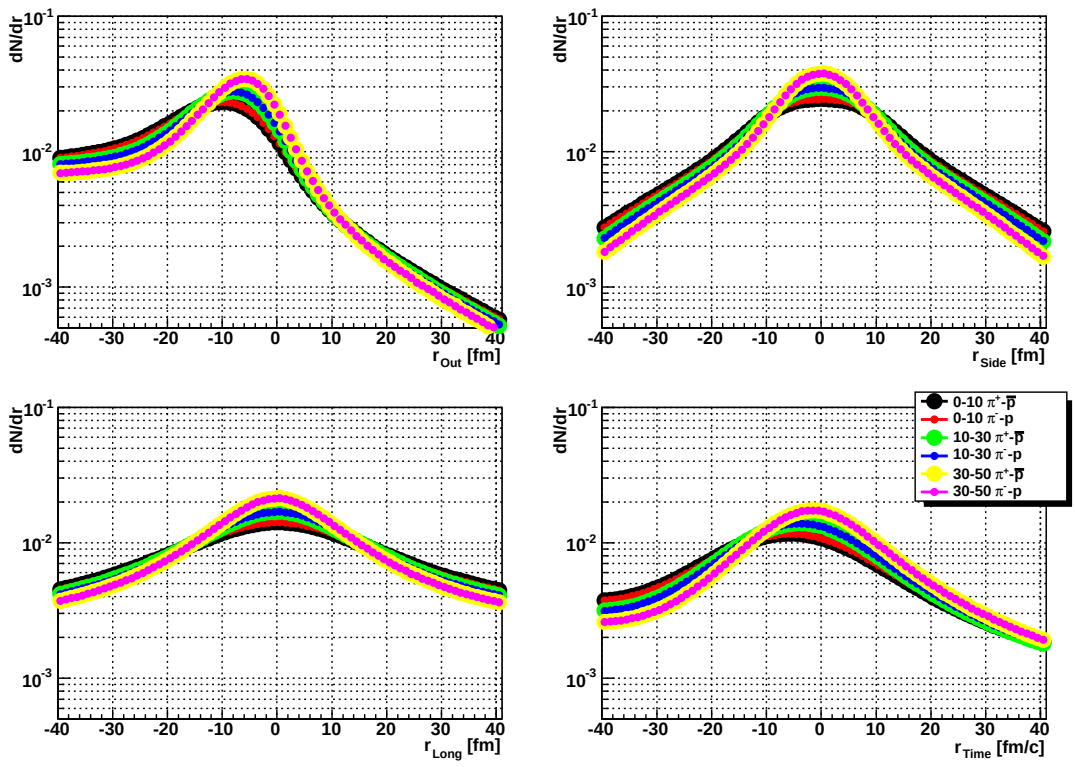

Figure 6.12: Two particle pion-proton pair separation distribution from UrQMDv3.3. Upper left panel shows distribution in *out* direction, upper right panel shows *side* direction, lower left panel shows *long* direction and lower right panel shows two particle emission time difference distribution.

created non-central collision.

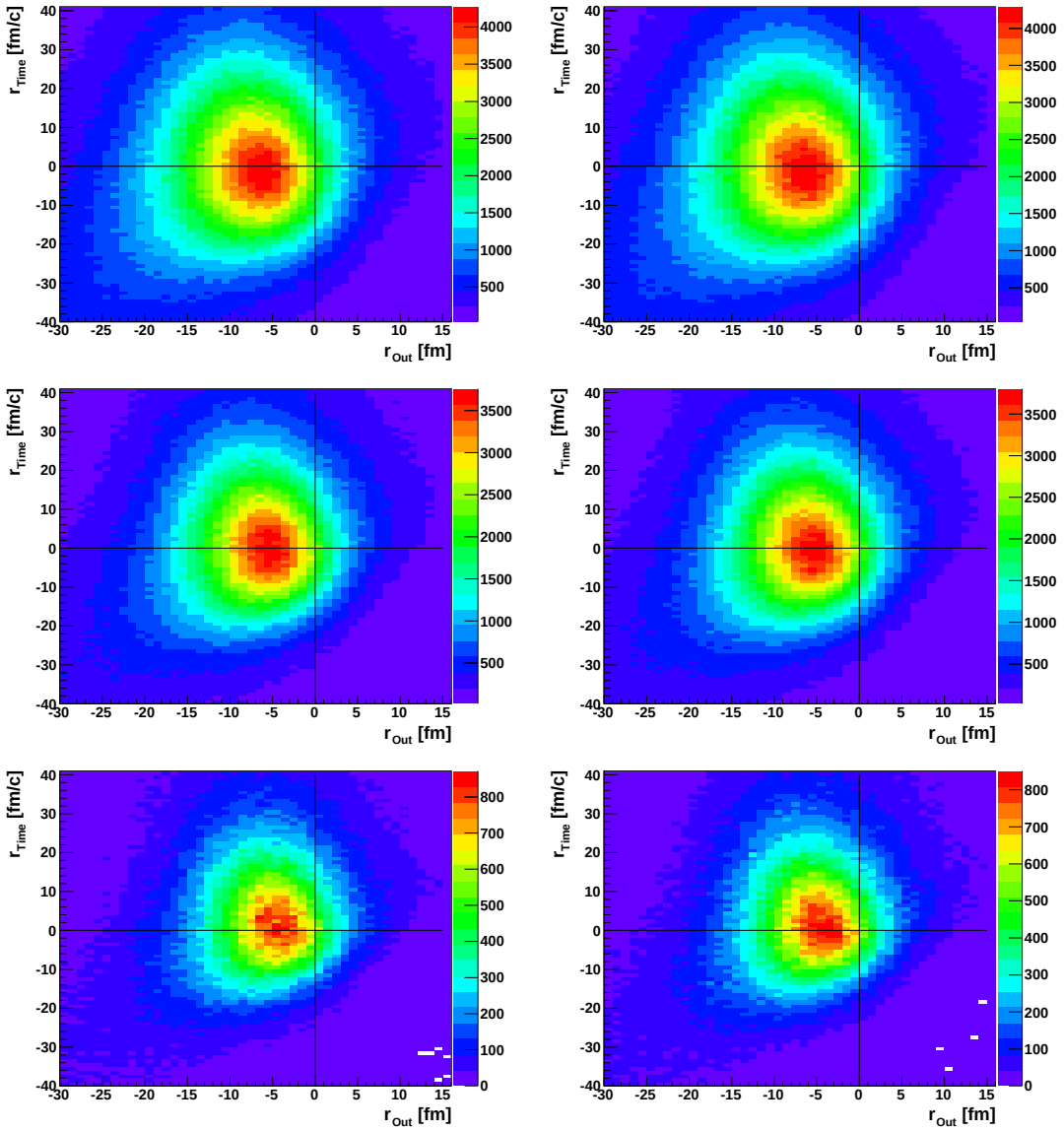

Figure 6.13: Distribution of the emission time difference versus separation of the emission points - UrQMD. Left panels show data for like-sign pion-proton pairs. Right panels show data for unlike-sign pion-proton pairs. Upper plots are for central (0-10%) Au+Au collisions, middle plots are for intermediate (10-30%) collisions and lower plots are for mid-central (30-50%) collisions.

Chapter 7

Conclusions

Femtoscopy of non-identical particles is a very exciting field of the heavy ion collision physics. This thesis presents the most advanced and the most successful so far study of correlations of pion-proton system. It supplements analyzes of identical and non-identical mezons or baryons done in the past by various world wide collaborations.

Analysis done in this thesis was performed at the highest available so far energy $\sqrt{s_{NN}} =$ 200GeV in the Au+Au head on collisions. Three centrality bins were selected from the recorded dataset: central events - 0-10% of the total hadronic cross section, intermediate events - 10-30% and mid-central events - 30-50%.

Pion-proton pairs may come from strong decays of Δ resonances or weak decays of Λ baryons thus extensive study was performed to estimate possible contribution to the correlation function from the products of such decays. It was found that both Δ and Λ lay in the correlation function above the region of the correlation effect. Pions and protons coming from Λ decays are one of the products that contribute to the fraction of primary pairs thus calculated experimental functions were corrected on purity. It was found that purity is slightly higher for particles than for anti-particles.

Significant difference in mass between pions and protons makes it very difficult to study correlations of the particles at close velocity in such an experiment like STAR where the time projection chamber has lower limit of transverse momentum acceptance is at the level of 0.1GeV/c and the upper limit of momentum acceptance, where particle identification is possible is around 1GeV/c. Due to these limitations requirements of this analysis exceeds the capabilities of the particle identification offered by the STAR TPC.

Traditional representation of the correlation function in $out - side - long$ was not suffi-

cient for study of pion-proton correlations. Also standard methods of decomposition of three-dimensional correlation function in spherical harmonics failed due to holes in the angular distribution of the k^* vector. Application of the recently developed method of calculating correlation function directly in spherical harmonics was a milestone in this analysis. This method allowed for calculation of reliable experimental pion-proton correlation function and extracting quantitative information from the fit procedure.

Data analysis required also applying of extended methods for background mixing which was necessary to get flat functions for large values of k^*. To obtain a high quality data sample a set of track selection methods have been used to remove split or merged pairs and electron-positron pairs coming from conversion (mainly in the material of the SVT detector) of gamma quants.

Pion-proton correlation functions were calculated for all four charge combinations $\pi^+ - p$, $\pi^- - \bar{p}$, $\pi^+ - \bar{p}$ and $\pi^- - p$ and constructed functions in spherical harmonics as well as in $out - side - long$. $Out - side - long$ parametrization due to already discussed problems provides only qualitative information about the size and space-time asymmetry. Reliable fit results were obtained for the $ReC_0^0(k^*)$ and $ReC_1^1(k^*)$ components for unlike sign pairs. Qualitative and quantitative results extracted from the constructed correlation functions show that:

- average emission points of pions and protons are not the same,
- proton source is shifted *outward* the created system,
- observed size of the pion-proton source and asymmetry between average emission points are correlated and decrease with impact parameter,
- measured asymmetry suggest collective behavior of the source created in Au+Au collisions
- delta resonances and lambda baryons do not affect observed asymmetry,
- evolution of the source created in central heavy ion collision lasts longer than evolution of the source created in non-central collision.
- size of the pion source is bigger than size of the proton source,
- if we assume `Therminator` with hydro as a representative tool for simulating heavy ion collisions we can claim that protons are in the average emitted earlier than pions.

Obtained in this thesis values of the system size and shift between average emission points of pions and protons are also in agreement with the results of the previous pion-kaon analysis.

Obtained quantitative results was compared to similar studies done with `Therminator` and `UrQMD` data. Calculated parameters of the Gaussian source are found to be between values provided by these two models. Fit results show correlation in centrality dependence of the system size and its asymmetry.

Analysis of pion-proton (meson-baryon) femtoscopy at RHIC done in this thesis is a step forward in the process of studying interactions in meson-meson, meson-baryon and baryon-baryon systems. Knowledge obtained during this study and methods developed during analysis will be very helpful in the femtoscopic analyzes planned for the already started at RHIC bream-energy-scan program dedicated to the critical point search.

Recently a TOF - time of flight detector covered full azimuthal angle of the STAR experiment also SVT - silicon vertex tracker which caused lots of problems with electron-positron contamination in the analyzed data was removed from the experiment. With this new setup of the experiment acquired in 2009/2010 run data of Au+Au collisions at $\sqrt{s_{NN}} = 200$GeV STAR will provide much higher quality of the reconstructed tracks. Tools and methods of data analysis prepared during work on this thesis will allow for quick repeat of analysis of pion-proton femtoscopy as well as computation of correlation functions for pion-kaon and not yet investigated kaon-proton system. Full analysis of these tree systems is very interesting and desired from the scientific point of view as the observed asymmetries in these systems should be complementary.

Bibliography

[1] F. Karsch; Lattice Results on QCD Thermodynamics; Nucl.Phys. A698 (2002) 199-208 [arxiv:0103314v1 [hep-ph]]

[2] Z. Fodor, S.D. Katz; Critical point of QCD at finite T and μ, lattice results for physical quark masses; JHEP 0404 (2004) 050 [arxiv:0402006v1 [hep-lat]]

[3] A. Bazavov et. al.; Equation of state and QCD transition at finite temperature; Phys.Rev.D80:014504 (2009) [arxiv:0903.4379v1 [hep-lat]]

[4] A. Adare et. al (Phenix Collaboration); Scaling properties of azimuthal anisotropy in Au+Au and Cu+Cu collisions at $\sqrt{s_{NN}} = 200$ GeV; Phys.Rev.Lett. 98 (2007) 162301 [arxiv:0608033v1 [nucl-ex]]

[5] B. Alessandro et. al (NA50 Collaboration); A new measurement of J/psi suppression in Pb-Pb collisions at 158 GeV per nucleon; Eur.Phys.J. C39 (2005) 335-345 [arxiv:0412036 [hep-ex]]

[6] T. Matsui, H. Satz, J/ψ suppression by quark-qluon plasma formation; Phys. Lett. B178 (1986) 416

[7] J. Adams et. al (STAR Collaboration); Evidence from d+Au measurements for final-state suppression of high pT hadrons in Au+Au collisions at RHIC; Phys. Rev. Lett. 91 (2003) 072304 [arxiv:0306024 [nucl-ex]]

[8] B.I. Abelev et. al (STAR Collaboration); Enhanced strange baryon production in Au+Au collisions compared to p+p at $\sqrt{s_{NN}}$ = 200 GeV; Phys. Rev. C 77 (2008) 44908 [arxiv:07052511 [nucl-ex]]

[9] M. Gazdzicki, M.I. Gorenstein; On the Early Stage of Nucleus-Nucleus Collisions; APOBB B30 (1999) 2705

[10] M. I. Gorenstein, M. Gazdzicki and K. A. Bugaev; Transverse Activity of Kaons and the Deconfinement Phase Transition in Nucleus–Nucleus Collisions; Phys. Lett. B 567 (2003) 175 [arxiv:0303041 [hep-ph]]

[11] C. Alt et. al (NA49 Collaboration); Pion and kaon production in central Pb+Pb collisions at 20A and 30A GeV: Evidence for the onset of deconfinement; Phys.Rev.C77 (2008) 024903 [arxiv:0710:0118 [nucl-ex]]

[12] S.A. Bass et. al; "Microscopic Models for Ultrarelativistic Heavy Ion Collisions"; Prog.Part.Nucl.Phys.41:255-370,1998 [arxiv:9803035v2 [nucl-th]]

[13] M. Bleicher et. al; "Relativistic Hadron-Hadron Collisions in the Ultra-Relativistic Quantum Molecular Dynamics Model"; J.Phys.G25:1859-1896,1999 [arXiv:9909407v1 [hep-ph]]

[14] A. Kisiel, T. Taluc, W. Broniowski, W. Florkowski; "THERMINATOR: THERMal heavy-IoN generATOR; Comput.Phys.Commun. 174 (2006) 669-687 [arxiv:0504047v2 [nucl-ex]]

[15] A. Kisiel; "Non-identical particle femtoscopy in models with single freezout"; Braz.J.Phys.37 (2007) 917-924 [arxiv:0612052 [nucl-th]]

[16] W. Broniowski, W. Florkowski, M. Chojnacki, A. Kisiel; Free-streaming approximation in early dynamics of relativistic heavy-ion collisions; Phys.Rev.C80:034902,2009 [arxiv:0812.3393v1 [nucl-th]]

[17] W. Broniowski, M. Chojnacki, W. Florkowski, A. Kisiel; Initial condition for hydrodynamics, partonic free streaming, and the uniform description of soft observables at RHIC; Phys.Rev.Lett.101:022301,2008 [arxiv:0801.4361v1 [nucl-th]]

[18] A. Kisiel, W. Broniowski, M. Chojnacki, W. Florkowski; Azimuthally-sensitive femtoscopy from RHIC to LHC in hydrodynamics with statistical hadronization; Phys.Rev.C79:014902,2009 [arxiv:0808.3363v2 [nucl-th]]

[19] A. Kisiel; Non-identical particle femtoscopy at $sqrts_{NN}$=200 AGeV in hydrodynamics with statistical hadronization; [arXiv:0909.5349v3 [nucl-th]]

[20] R. Lednicky; Correlation Femtoscopy of Multiparticle Processes; Phys. Atom. Nucl. 67 (2004) 73-83

[21] W. Broniowski, M. Rybczynski, P. Bozek; GLISSANDO: GLauber Initial-State Simulation AND mOre; Comput.Phys.Commun.180:69-83,2009 [arXiv:0710.5731v3 [nucl-th]]

[22] F. Cooper, G. Frye; Single-particle distribution in the hydrodynamic and statistical thermodynamic models of multiparticle production; Phys. Rev. D 10, (1974) 186-189

[23] R. Hanbury Brown, R.Q. Twiss; Correlation between Photons in two Coherent Beams of Light; Nature, 177, (1956) 27-29

[24] R. Hanbury Brown, R.Q. Twiss; A Test of a new type of stellar interferometer on Sirius; Nature 178 (1956) 1046-1048

[25] G. Goldhaber, S. Goldhaber, W. Lee, and A. Pais; Influence of Bose-Einstein Statistics on the Antiproton-Proton Annihilation Process; Phys. Rev. 120 (1960) 300-312

[26] G.I. Kopylov, M.I. Podgoretski; Sov. J. Nucl. Phys. 15, 219 (1972).

[27] U.A. Wiedemann, U. Heinz; Particle Interferometry for Relativistic Heavy-Ion Collisions; Phys. Rept. 319 (1999) 145-230 [arXiv:9901094v1 [nucl-th]]

[28] S. Pratt; Pion interferometry of quark-gluon plasma; Phys. Rev. D33, (1986) 1314

[29] G. Bertsch, M. Gong, M. Tohyama; Pion interferometry in ultrarelativistic heavy-ion collisions; Phys. Rev. C37, (1988) 1896

[30] Y.M. Sinyukov, R. Lednicky, S.V. Akkelin, J. Pluta, B. Erazmus; Coulomb corrections for interferometry analysis of expanding hadron systems; Phys. Lett. B432 (1998) 248-257

[31] R. Lednicky; Finite-size effect on two-particle production in continuous and discrete spectrum; [arXiv:0501065v3 [nucl-th]]

[32] R. Lednicky; Correlation femtoscopy of multiparticle processes; Phys.Atom.Nucl. 67 (2004) 72-82; Yad.Fiz. 67 (2004) 73-83 [arxiv:0305027 [nucl-th]]

[33] R. Lednicky, S. Panitkin, N. Xu; Search for delays between unlike particle emissions in relativistic heavy-ion collisions; [arXiv:0304062v1 [nucl-th]]

[34] R. Lednicky, V.L. Lyuboshitz, B. Erazmus, D. Nouais; How to measure which sort of particles was emitter earlier and which later. Phys. Lett. B373 (1996) 30-34

[35] S. Voloshin, R. Lednicky, S. Panitkin, N. Xu; Relative space time asymmetries in pion and nucleon production in noncentral nucleus-nucleus collisions high energies; Phys. Rev. Lett. 79 (1997) 4766-4769

[36] Z. Chajecki, M. Lisa; Global Conservation Laws and Femtoscopy of Small Systems; Phys. Rev. C 78 (2008) 064903

[37] A. Kisiel, D.A. Brown; Efficient and robust calculation of femtoscopic correlation functions in spherical harmonics directly from the raw pairs measured in heavy-ion collisions; [arXiv:09013527v2 [nucl-th]]

[38] B.I. Abelev (STAR Collaboration); Pion interferometry in Au+Au and Cu+Cu collisions at $\sqrt{s_{NN}} = 62.4 and 200 GeV$; Phys. Rev. C 80 (2009) 24905 [arxiv:09031296v2 [nuxl-ex]]

[39] J. Adams (STAR Collaboration); Pion-Kaon Correlations in Central Au+Au Collisions at $\sqrt{s_{NN}}$= 130 GeV; Phys. Rev. Lett. 91 (2003) 262302 [arxiv:0307025 [nucl-ex]]

[40] B.I. Abelev (STAR Collaboration); Neutral Kaon Interferometry in Au+Au collisions at $\sqrt{s_{NN}} = 200 GeV$; Phys. Rev. C 74 (2006) 54902 [arxiv:0608012 [nucl-ex]]

[41] J. Adams (STAR Collaboration); Proton Λ correlations in central Au+Au collisions at $\sqrt{s_{NN}} = 200 GeV$; Phys. Rev. C 74 (2006) 64906 [arxiv:0511003 [nucl-ex]]

[42] Z. Chajecki; Femtoscopy in hadron and lepton collisions: world systematics; APPB 40 (2009) 1119-1136 [arXiv:0901.4078v1 [nucl-ex]]

[43] H. Zbroszczyk; Studies of baryon-baryon correlations in relativistic nuclear collisions registered at the STAR experiment (PhD Thesis)

[44] D. Miskowiec; Separation between sources of pions and protons in central Au+Au collisions at the AGS (E877); [arXiv:9808003v2 [nucl-ex]]

[45] R. Lednicky; Proceedings of Int. Conf. on Contemporary Physics - IV, Ulaanbaatar, Mongolia, 13-20 August 2007

[46] Ch.Blume et al.; Results on correlations and fluctuations from NA49; (NA49), Nucl. Phys. A 715 (2003) 55c

[47] M. Harrison et al.; RHIC project overview; Nucl. Inst. Meth. A 499 (2003) 235

[48] RHIC web page [www.bnl.gov/RHIC]

[49] T. Ludlam; Overview of experiments and detectors at RHIC; Nucl. Inst. Meth. A 499 (2003) 428-432

[50] K. Adcox et al. (Phenix Collaboration),; PHENIX detector overview; Nucl. Iinstr Meth. A499 (2003) 469-479

[51] Phenix Collaboration web page [www.phenix.bnl.gov]

[52] B.B. Back et al. (Phobos Collaboration); The Phobos detector at RHIC; Nucl. Inst. Meth. A499 (2003), 603

[53] Phenix Collaboration web page [www.phobos.bnl.gov]

[54] (BRAHMS Collaboration); The BRAHMS Experiment at RHIC; Nucl. Instr. Meth. A499, (2003) 437

[55] Brahms Collaboration web page [www.brahms.bnl.gov]

[56] The Brookhaven National Laboratory Bulletin Vol. 56 - No. 14

[57] S. Bueltmann, et al. (pp2pp Collaboration); First Measurement of Proton-Proton Elastic Scattering at RHIC; Phys.Lett. B579 (2004) 245-250 [arxiv:0305012v5 [nucl-ex]]

[58] W. Guryn; Physics with tagged forward protons at RHIC; APOBB B40 (2009) 1897-1907

[59] K.H. Ackermann, et al. (Star Collaboration); Star detector overview; Nucl. Instrum. Meth. A 499 (2003) 624-632

[60] Star Collaboration web page [www.star.bnl.gov]

[61] F. Bergsma, et al.; The STAR detector magnet subsystem; Nucl. Instrum. Meth. A 499 (2003) 633-639

[62] M. Anderson, et al.; The STAR time projection chamber: a unique tool for studying high multiplicity events at RHIC; Nucl. Instrum. Meth. A 499 (2003) 659-678

[63] H. Bichsel; Energy loss in thin layers of argon; STAR Note 0418 (2000)

[64] H. Bichsel; Comparison of Bethe-Bloch and Bichsel functions; STAR Note 0439 (2002)

[65] H. Bichsel; Calculated and experimental Landau spectra in a TPC; STAR Note 0440 (2002)

[66] H. Bichsel; "Resolution" of particle identification with TPCs; STAR Note 0441 (2002)

[67] R. Bellwied, et al.; The STAR Silicon Vertex Tracker: A large area Silicon Drift Detector; Nucl. Instrum. Meth. A 499 (2003) 640-651

[68] F.S. Bieser, et al.; The STAR trigger; Nucl. Instrum. Meth. A 499 (2003) 766-777

[69] J. Adams (Star Collaboration); Pion interferometry in Au+Au collisions at $\sqrt{s_{NN}}$ = 200 GeV;Phys. Rev. C 71 (2005) 44906 [arxiv:0411036v2 [nucl-ex]]

[70] A. Kisiel; "CorrFit - a program to fit arbitrary two-particle correlation functions", NUKLEONIKA 2004, 49 (Suppl. 2), (2004) S81-S83.

[71] M. Zawisza; Femtoscopy of Pion-Proton System at 200 AGev; APOBB B40 1163-1170 (2009)